HAL
open science

Self-mixing interferometry for absolute distance measurement : modelling and experimental demonstration of intrinsic limitations

Mengkoung Veng

To cite this version:

Mengkoung Veng. Self-mixing interferometry for absolute distance measurement : modelling and experimental demonstration of intrinsic limitations. Optics / Photonic. Institut National Polytechnique de Toulouse - INPT, 2020. English. NNT : 2020INPT0077 . tel-04419504v2

HAL Id: tel-04419504

https://theses.hal.science/tel-04419504v2

Submitted on 26 Jan 2024

HAL is a multi-disciplinary open access archive for the deposit and dissemination of scientific research documents, whether they are published or not. The documents may come from teaching and research institutions in France or abroad, or from public or private research centers.

L'archive ouverte pluridisciplinaire **HAL**, est destinée au dépôt et à la diffusion de documents scientifiques de niveau recherche, publiés ou non, émanant des établissements d'enseignement et de recherche français ou étrangers, des laboratoires publics ou privés.

THÈSE

En vue de l'obtention du

DOCTORAT DE L'UNIVERSITÉ DE TOULOUSE

Délivré par :

Institut National Polytechnique de Toulouse (Toulouse INP)

Discipline ou spécialité :

Photonique et système optoélectronique

Présentée et soutenue par :

M. MENGKOUNG VENG

le vendredi 16 octobre 2020

Titre :

Self-mixing interferometry for absolute distance measurement: modelling and experimental demonstration of intrinsic limitations

---

Ecole doctorale :

Génie Electrique, Electronique, Télécommunications (GEET)

Unité de recherche :

Laboratoire d'Analyse et d'Architecture des Systèmes (LAAS)

Directeur(s) de Thèse :

M. JULIEN PERCHOUX

M. FRANCIS BONY

Rapporteurs :

M. ALEXANDRE LOCQUET, GEORGIATECH

M. SANTIAGO ROYO, CD6 Universitat Politecnica Catalunya

Membre(s) du jury :

Mme VERONIQUE BARDINAL, LAAS TOULOUSE, Président

M. DAVID CITRIN, GEORGIA INSTITUTE OF TECHNOLOGY, Membre

M. FRANCIS BONY, TOULOUSE INP, Membre

M. JULIEN PERCHOUX, TOULOUSE INP, Membre

To younger me...

You know, for doing this!

Acknowledgements

Many people inspired and encouraged me on the path that led to this thesis. I am grateful to these people, who have helped me to grow as a person, as well as an independent researcher.

I would like to express my sincere gratitude to my principal advisor, Dr Julien Perchoux, for his words of wisdom, his timely advice and for supporting my research endeavour. I would also like to thank my associate advisor, Dr Francis Bony, who helped me along the way during this research.

I am also indebted to the technical support and friendly encouragement provided by Clément Tronche and Francis Jayat during the experiments. I would like to equally thank Emmanuelle Tronche for her help and patience, allowing me to wade through the paperwork.

I would also like to thank my fellow research students, particularly Fernando Urgiles, Einar Knudsen, Bastien Grimaldi, Yu Zhao, Laura Le Barbier, Antonio Luna Arriaga, Jalal Al Roumy, Raül da Costa Moreira, Evelio R. Miquet, Lavinia Ciotirca and Harris Apriyanto. Cold beers on Friday nights - or any night for that matter, St. Patrick's days, lunches, dinners, parties, coffees and talks that we had shared together shaped my world and who I am today.

I am so thankful to my parents who supported me with love and understanding. Without you, I could never have written this thesis. I am also very grateful to my friends who have supported me during the long road to this thesis.

To my Cambodian PhD fellow in Dijon, Lorn Da, who always shared the difficulties, encouraging me to write this thesis and backpacking with me across Europe. There are many terror-turn-to-funny stories to tell people about these journeys. I won't forget that you are afraid of water.

Lastly, I want to thank the unknown man who hit me one night with his speeding car, while I walked along a street in Phnom Penh - for this accident was probably the reason I wrote this thesis.

Contents

Introduction **1**

1 Introduction to Distance Measurement **5**
1.1 Sonar and Radar 6
1.1.1 Sonar 6
1.1.2 Radar 7
1.2 Triangulation 8
1.2.1 Stereo vision 8
1.2.2 Active triangular 10
1.3 Time of flight 11
1.3.1 Pulsed based direct TOF distance measurement 12
1.3.2 Phase-shift based indirect TOF distance measurement 14
1.4 Interferometry 15
1.4.1 Michelson interferometry 15
1.4.2 Self-mixing interferometry 19

2 Modelling the Fringe Disappearance in a Self-Mixing Sensor **31**
2.1 Three-mirror model 32
2.2 Dynamic model of laser under feedback 40
2.3 Phase condition 47
2.3.1 When $C \leq 1$ 48
2.3.2 When $C > 1$ 49
2.3.3 Fringes disappearance mechanism 52
2.3.4 Feedback parameter C and fringe disappearance 52
2.4 Conclusion 56

3 Absolute Distance Measurement **59**
3.1 Modelling 59
3.2 Fringe disappearance in absolute distance 63
3.2.1 Laser behaviour under the excess phase equation 64
3.2.2 Laser behaviour under the rate equations 66
3.3 Experiments 68
3.3.1 Feedback power ratio profile 68
3.3.2 Frequency modulation coefficient 73
3.3.3 Laser injection current 75
3.3.4 Distant fringe frequency 77
3.3.5 Fringe disappearance experiment 79
3.3.6 Fringes disappearance behaviour 81
3.3.7 Measurement error 89
3.4 Conclusion 92

4 Combined Distance and Velocity Measurement **95**
4.1 Laser Doppler 96
4.1.1 Modelling 96
4.1.2 Experiment and validation 100
4.2 Measurement of the target distance and velocity 102
4.2.1 Modelling 103
4.2.2 Phase behaviour 110
4.2.3 Experimental validation 115
4.3 Profiling 120
4.3.1 Distance measurement 120
4.3.2 Velocity measurement 121
4.3.3 Distance and velocity measurement 123
4.4 conclusion 125

Conclusion **129**

Bibliography **133**

Abstract/Résumé **141**

List of Figures

1.1 Non-contact distance measurement techniques. 6
1.2 Principle of sonar distance measurement. 7
1.3 Principle of triangulation-based optical sensors: (a) Passive Triangulation (Stereo Vision); (b) Active Triangulation. 9
1.4 Essential optical components of a LiDAR system [1]. 12
1.5 Principle of direct TOF distance measurement method [2]. 13
1.6 Principle of phase-shift distance measurement method [2]. 15
1.7 Principle of Michelson interferometer. 16
1.8 Principle of Self-Mixing interferometry. 19
1.9 Frequency modulation coefficient of short-external-cavity Sharp LT080 laser [3]. 22
1.10 Laser optical power with hysteresis for an absolute distance measurement both theoretical and experimental result [4]. 23
1.11 (a) Front view of the screw reconstructed, (b) Another view of the target being obtained by image processing [4]. 24
1.12 Self-mixing interferometers with double external cavities [5]. 24
1.13 Experimental result by double external cavities [5]. 25
1.14 Block diagram of experimental result, signals from the photodetector and laser junction voltage are used to determine the distance between the laser and the target [6]. 25
1.15 Experimental time-domain signal (a) and its frequency spectrum (b) at the target distance of 30 cm method [6]. 26
1.16 Experimental setup with double modulation−wavelength and phase [7]. . . . 27
1.17 Derivative of the total output power waveform (light) and FFT (dark) with the single-mode VCSEL at (a) 36.5 cm and (b) 36.6 cm [8]. 28

1.18 Derivative of the total output power waveform (light) and FFT (dark) with the multi-mode VCSEL at (a) 36.5 cm and (b) 36.6 cm [8]. 28

1.19 The shape of laser current modulation [9]. 29

1.20 Experimental results of wavelength modulation coefficient in function of frequency modulation [9]. 29

1.21 Experimental setup with double modulation−wavelength and phase [10]. . . 30

1.22 (a) Power spectra of the beat signal with and without current reshaping.(b) Reshaped current versus original current [10]. 30

2.1 Schematic of two-mirror model of an optical cavity. 33

2.2 Schematic of the laser diode under optical feedback. Solid line with arrows indicates the beam light direction both in the internal and external cavity. . . 35

2.3 (a) Simulation of the three-mirror model versus change in emission frequency for different feedback levels. The dash line is the axis when the laser diode does not experience with the optical feedback. Unique solution can be found when the feedback parameter C is smaller than one while multiple solutions (both stable and unstable solution) can be found when the feedback parameter C is greater than one. (b) Operating regimes of LFI, after [11]. Region I, weak feedback; region II, moderate feedback; region III, strong feedback; region IV, chaos with islands of stability; region V, external cavity. 39

2.4 Plot of the excess phase equation for $C = 0.7$, and $\alpha = 5$. The red broken line is the axis where there is no optical feedback, and the black solid line indicates the solution path of φ_{FB}. 48

2.5 Plot the behaviour of $\cos\varphi_{\mathrm{FB}}$ under the feedback level $C = 0.7$. (a) In case of the phase stimulus decreases over time; (b) In case of the phase stimulus increases over time. 49

2.6 Plot of the excess phase equation for $C = 3$, and $\alpha = 5$. The red broken line is the axis where there is no optical feedback, and the black solid and broken lines indicate the region of stable and unstable solution of φ_{FB} respectively. . 50

2.7 Plot (a) show the phase stimulus φ_s is modulated in triangle waveform with a period T and plot (b) is the resulting of phase response φ_{FB} with the change of φ_{s} from 8π to 2π, the feedback parameter $C = 3$, and $\alpha = 5$. The thin dotted lines shows the unstable solutions to the excess phase equation, the thick solid and dotted lines trace the locus of solution in plot (b) to the phase stimulus in plot (a). 51

2.8 Numerical simulation with 6π phase stimulus's amplitude modulation. Plots (a), (c), (e), (g) are the phase behaviours under different feedback parameters C. Plots (b), (d), (f), and (h) are the results of derivative of output power under different feedback parameters C which correspond to (a), (c), (e), (g) respectively. (a) and (b) are plotted with C = 3; (c) and (d) are plotted with C = 4.6; (e) and (f) are plotted with C = 7.5; (g) and (h) are plotted with C = 10. 53

2.9 Numerical simulation with 12π phase stimulus's amplitude modulation. Plot (a) is the phase behaviour under different feedback parameters $C = 10$. Plot (b) is the result of derivative of output power which correspond to (a). 54

2.10 Evolution of the increment of C that results in the loss of two more fringes as a function of C and definition of the C ranges for which a pair of fringes have disappeared. 56

3.1 (a) Simulation of modulated injection current in triangle waveform varies from 60 mA to 60.5 mA at frequency modulation of 50 Hz−the increase and decrease ramp depicted in solid and broken line, respectively. (b) Simulation of laser emission frequency changes over time with the given FM coefficient $-3\,\mathrm{GHz/mA}$ and the amplitude of current modulation $0.5\,\mathrm{mA}$ peak-to-peak. (c) Simulation of optical output power of SMI signal with the small ripples in triangle waveform under the optical feedback $C = 0.7$ within the given parameter. (d) Simulation of the derivative of output optical power resulting from plot (c). 62

3.2 The behaviour of the laser diode phase under weak optical feedback $C = 0.7$. (a) Plot phase response in function of phase stimulus. (b) Plot the derivative of output power resulting from the dwelling stable solution from (a). 64

3.3 Simulation self-mixing absolute distance that the thick solid and broken lines indicate the direction of the phase stimulus during the decreasing and increasing respectively. (a) Plot of phase response φ_{FB} in function of phase stimulus φ_{s} under the optical feedback $C = 2.20$. (b) Plot of derivative of output power in the result from the dwelling phase in (a). (c) Plot of phase response φ_{FB} in function of phase stimulus φ_{s} under the optical feedback $C = 6.97$. (d) Plot of derivative of output power in the result of from the dwelling phase in (c). . 66

3.4 Simulation of output power from the rate equations under feedback parameter $C = 2.20$. (a) Plot of the phase response φ_{FB} in function of the phase stimulus φ_{s}; the thick solid and broken lines indicate the direction of the phase stimulus during decreasing and increasing respectively. (b) Plot of derivative of output power resulting from the evolution of the phase in (a). 68
3.5 Simulation of output power from the rate equations under feedback parameter $C = 6.97$. (a) Plot of the phase response φ_{FB} in function of the phase stimulus φ_{s}; the thick solid and broken lines indicate the direction of the phase stimulus during decreasing and increasing respectively. (b) Plot of derivative of output power resulting from the evolution of the phase in (a). 69
3.6 Simulation of output power from the rate equations under feedback parameter $C = 32.16$. (a) Plot of the phase response φ_{FB} in function of the phase stimulus φ_{s}; the thick solid and broken lines indicate the direction of the phase stimulus during decreasing and increasing respectively. (b) Plot of derivative of output power resulting from the evolution of the phase in (a). 70
3.7 Experimental setup for measuring the target surface's reflectivity. 71
3.8 Amplitude reflectivity coefficient for different surface−white paper, flat metal, microprismatic reflective tape, and microsphere reflective tape. 71
3.9 Variation of feedback parameter C as a function of the external cavity L_{ext} with different target's surfaces. (a) White paper. (b) Metal. (c) Microprismatic reflective tape. (d) Microsphere reflective tape. 72
3.10 Block Diagram of experimental setup: laser and photodetector are in the same package; the laser bias injection current is modulated in triangle waveform from the function generator, and the target is a white paper located at 1.2 m from the laser facet. 73
3.11 Experimental SMI signals resulting from modulating the laser with different modulation frequency when the target is fixed at 1.2 m from the target: (a) 100 mHz. (b) 1 kHz. 74
3.12 Experimental measurement of FM coefficient as a function of modulation frequency. 74
3.13 The results of experiment of SMI absolute distance with different injection currents under $10\,\mathrm{mA}$ peak-to-peak of current amplitude at $50\,\mathrm{Hz}$ frequency modulation with the target distance of 1.2 m. (a) $12.5\,\mathrm{mA}$. (b) $15\,\mathrm{mA}$. (c) $17.5\,\mathrm{mA}$. (d) $20\,\mathrm{mA}$. 76
3.14 The results of experiment of SMI absolute distance with different injection currents under $10\,\mathrm{mA}$ peak-to-peak of current amplitude at $50\,\mathrm{Hz}$ of the frequency modulation. (a) $12\,\mathrm{mA}$. (b) $20\,\mathrm{mA}$. 76

3.15 Experimental signal acquisition for the distance of $1.5\,\mathrm{m}$ with $20\,\mathrm{mA}$ injection current: (a) The input voltage to the driving circuit which then converted in to a current with corresponding current fluctuation of $5\,\mathrm{mA}$ peak-to-peak triangle modulation at $10\,\mathrm{Hz}$ of frequency; (b) the SMI distant signal resulting from a linear modulated current ramping. 77

3.16 An assuming plot: (a) A full cycle of linear triangle modulation of injection current in function of time. (b) The non-linearity of the laser frequency caused by linear modulation of triangle waveform. (c) The result of non-constant of fringe frequency in the optical output power. 78

3.17 (a) Plot the measurement result of fringe frequency indicated in black solid lines and the curve fitting from MATLAB Toolbox indicated in the red solid line. (b) Plot SMI absolute distance with the obtained parameters in (a) under the optical feedback level $C = 0.9$. 79

3.18 Block diagram of experimental setup. Laser and photodiode are in the same package. 80

3.19 Experimental SMI signal acquisition for the distance of 1.5 m with different target's amplitude reflectivities. (a) 1.77%. (b) 2.37%. (c) 2.97%. (d) 8.61%. (e) 13.06%. (f) 15.86%. (g) 21.08%. (h) 25.54%. 82

3.20 Simulation SMI output power in time for the distance of 1.5 m with different target's amplitude reflectivities. (a) 1.77%. (b) 2.37%. (c) 2.97%. (d) 8.61%. (e) 13.06%. (f) 15.86%. (g) 21.08%. (h) 25.54%. 83

3.21 The behaviour of the interferometric fringe disappearance and the feedback parameter C. The thin solid lines show the result of interferometric fringes disappearance in theory and the marker points shows the results of the experiment. 84

3.22 Experimental SMI signal acquisition for the target distance of 1.2 m with different amplitude reflection coefficients when the laser diode is operated with 20 mA of injection current and 5 mA of current's amplitude at 1 Hz of frequency modulation. 86

3.23 Simulation SMI output power in time for the distance of 1.2 m with different values feedback parameter C. (a) $C = 47$. (b) $C = 60$. (c) $C = 75$. 87

3.24 (a) Plot laser diode bias injection current in triangle waveform and constant. (b) Plot SMI absolute distance through the rate equation with the form of injection current in (a) under the feedback parameter $C = 47$. 88

3.25 Experimental SMI signal acquisition with the same target's amplitude reflectivities. (a) Without any perturbation during the propagation of light between the laser and the target. (b) With perturbation occurring during light propagation which then restarts the lasing mode from the previous solution path. . 89
3.26 The results of distant measurement of the microprismatic reflective tape with different methods of calculation. (a) The counting number of appeared interferometric fringes. (b) The average time spacing between the appeared interferometric fringes. 90
3.27 (a) Experimental result of fringe frequency at the distance of 1.2 m when the laser diode is modulated with amplitude 10 mA peak-to-peak at 100 Hz frequency modulation indicated in black solid lines, and MATLAB curve fitting is used to define the constant parameter A and τ indicated in red solid line. (b) Laser emission frequency in function of time resulting from curve fitting parameters in (a). 91
3.28 Determine FM coefficient value from the plot FM coefficient in function of time resulting from curve fitting of the laser emission frequency with the SMI signal demi-period of modulation when the target covered by the microprismatic reflective tape is fixed at a distance of 1 m. 92
3.29 Measurement error with time spacing method: the solid black line measured with Ω= -354 MHz/mA and the solid red line measured with the exponential of the FM coefficient resulting from the fringe frequency under the weak optical feedback regime. 93

4.1 The principle of self-mixing interferometer for velocimetry application with a translating target. Solid line with arrows indicates the beam light direction both in the internal and external cavity. 97
4.2 Simulation self-mixing velocimetry power under the optical feedback $C = 0.7$: (a) In the time domain. (b) In the frequency domain. 97
4.3 Simulation self-mixing velocimetry power under different optical feedback parameter C. 98
4.4 Simulation self-mixing power resulting from the Doppler shift distribution based on the rate equations. (a) In the time domain. (b) PSD of the self-mixing power variations in (a). 100
4.5 Experimental setup for self-mixing Doppler shift with the rotating target. . . . 101
4.6 Experimental results of Doppler shift with the white paper surface. (a) The self-mixing signal in the time domain. (b) PSD of of the self-mixing power variations obtained from (a). 102

4.7 Experimental results of Doppler shift with the microprism reflective tape surface. (a) The self-mixing signal in the time domain. (b) PSD of of the self-mixing power variations obtained from (a). 103
4.8 Simulation laser phase stimulus for the rotating target. (a) In the clockwise direction with the speed v = +0.35 mm/s. (b) In the anticlockwise direction with the speed v = -0.35 mm/s. 105
4.9 Simulation self-mixing power resulting from modulating the phase stimulus in the triangle waveform under the feedback parameter $C = 0.7$ in different velocity directions. (a) In the clockwise direction with the speed v = +0.35 mm/s. (b) In the anticlockwise direction with the speed v = -0.35 mm/s.106
4.10 FFT of the simulated self-mixing velocimetry output power resulting from the triangular frequency sweeping. 107
4.11 Simulation laser phase stimulus for the rotating target. (a) In the clockwise direction with the speed v = +2 mm/s. (b) In the anticlockwise direction with the speed v = -2 mm/s. 108
4.12 Simulation self-mixing power resulting from modulating the phase stimulus in the triangle waveform under the feedback parameter $C = 0.7$ in different velocity directions. (a) In the clockwise direction with the speed v = +2 mm/s. (b) In the anticlockwise direction with the speed v = -2 mm/s. 109
4.13 FFT of the simulated self-mixing velocimetry output power resulting from the triangular frequency sweeping. 109
4.14 (a) Plot the triangle laser phase stimulus sweeping in the function of time when the distance beat frequency is superior to the Doppler frequency. (b) The lasing mode in phase behaviour under the optical feedback parameter $C = 0.7$. 111
4.15 (a) Plot the lasing mode behaviour resulting from the triangular phase stimulus sweeping under the feedback parameter $C = 31.26$. (b) Simulation the self-mixing power resulting from dwelling of the lasing mode in (a). 113
4.16 (a) Plot the triangle laser phase stimulus sweeping in the function of time when the distance beat frequency is inferior to the Doppler frequency. (b) The lasing mode in phase behaviour under the optical feedback parameter $C = 0.7$. 114
4.17 (a) Plot the lasing mode behaviour resulting from the triangular phase stimulus sweeping under the feedback parameter $C = 26$. (b) Simulation the self-mixing power resulting from dwelling of the lasing mode in (a). 115
4.18 Plot the experimental results of FM coefficients in function of frequency modulations. 116

4.19 Block diagram of experimental setup. Laser and photodiode are in the same package, and the target is metal disc that can be rotated through the DC motor. 117
4.20 Experimental SMI signal acquisition when the distance beat frequency is superior to the Doppler frequency in different velocity directions and target surfaces. (a) and (b) The target as a white paper surface rotates in clockwise and anticlockwise, respectively. (c) and (d) The target as a microprism reflective tape surface rotates in clockwise and anticlockwise, respectively. 118
4.21 Experimental SMI signal acquisition when the distance beat frequency is inferior to the Doppler frequency in different velocity directions and target surfaces. (a) and (b) The target as a white paper surface rotates in clockwise and anticlockwise, respectively. (c) and (d) The target as a microprism reflective tape surface rotates in clockwise and anticlockwise, respectively. 119
4.22 Experimental results of SMI distance signal by triangular frequency sweeping. 120
4.23 (a) Experimental results of SMI distance signal for one cycle of the triangle waveform. (b) Peaks detection of half-period of the triangular SMI waveform. (c) Histogram of beat frequencies resulting peak detections in (b). 122
4.24 Distance measurements resulting from the SMI triangular frequency sweeping ranging from 128 cm to 133 cm. 123
4.25 Experimental results of Doppler shift with the reflective tape surface. (a) The self-mixing signal in the time domain. (b) PSD of of the self-mixing power variations obtained from (a). 124
4.26 Experimental results of SMI signal of distance and velocity by triangular frequency sweeping. 125
4.27 Experimental results of SMI signal of distance and velocity for one cycle of the triangle waveform. 125
4.28 (a) Peak detections of the first half self-mixing signal of the triangle waveform. (b) Histogram of the beat frequencies resulting from (a). (c) Peak detections of the other half self-mixing signal of the triangle waveform. (d) Histogram of the beat frequencies resulting from (d). 126
4.29 Distance measurements resulting from the SMI triangular frequency sweeping ranging from 128 cm to 133 cm when the target rotates. 126
4.30 Doppler frequency measurement resulting from the SMI triangular frequency sweeping when the target is fixed at the distances ranging from 128 cm to 133 cm. 127

List of Tables

3.1 In-Plane laser parameters [12]. 61

List of Symbols

α	Linewidth enhancement factor
α_{m}	Effective mirror loss
α_{s}	Loss coefficient mainly due to absorption by the free carrier
β	Phase constant
ε	Re-injection loss factor
η_{i}	Current injection efficiency
Γ	Confinement factor, $g = \Gamma g_{\mathrm{st}}$
$\hbar$	Plank's constant
κ_{ext}	Coupling strength between the target and the laser cavity
λ_{th}	Laser emission wavelength in vacuum
Ω	Frequency modulation coefficient
ω	Laser mode angular frequency
ω_{th}	Laser mode angular frequency in the absence of the optical feedback at threshold
τ_{ext}	External round-trip propagation time
τ_{in}	Internal round-trip propagation time of the laser cavity
τ_{n}	Carrier lifetime
τ_{ph}	Photon lifetime
τ_{TOF}	Time of flight

θ	Angle between the laser axis and the target velocity vector
ν	Velocity of the target
φ	Phase of E
φ_{FB}	Phase response
$\varphi_{\mathrm{FB,H}}$	Phase response at the high boundary
$\varphi_{\mathrm{FB,L}}$	Phase response at the low boundary
φ_{s}	Phase stimulus
$\varphi_{\mathrm{s,H}}$	Phase stimulus at the high boundary
$\varphi_{\mathrm{s,L}}$	Phase stimulus at the low boundary
a	Differential gain
C	Feedback parameter
c	Speed of light in Vacuum
E	Slowly varying (complex) envelop of the electric field
$f_{\mathrm{b,1}}$, $f_{\mathrm{b,2}}$	Beat frequencies in each half of the triangle waveform
f_{b}	Fringe frequency
f_{D}	Doppler frequency produced by velocity at the target
f_{d}	Beat frequency produced by distance of the target
f_{m}	Frequency modulation
G	Gain in the laser cavity—a function of N and S
g	Material gain in stimulated emission
g_{st}	Stimulated gain coefficient
g_{th}	Laser's gain at threshold
I	Laser operating current
k_{B}	Boltzmann's constant
L_{ext}	External distance from the source to the laser
L_{in}	Length of the laser cavity
m	Mode index (integer)

n_{ext}	Effective refractive index of the medium that the laser beam travels through
n_{g}	Effective group refractive index
n_{th}	Laser cavity effective refractive index at threshold
N	Carrier density in the laser cavity
N_{i}	Intrinsic carrier density in the laser cavity
N_{th}	Carrier density in the laser cavity at threshold
N_{tr}	Carrier density in the laser cavity at transparency
P	Optical power
P_0	Average output power of the laser n DC term
q	Charge of an electron
r_1, r_2	Amplitude reflection coefficient of the laser facet M_1 and M_2, respectively
r_{eq}	Amplitude reflection coefficient of equivalent mirror (laser's facet M_2 and the external target as the third mirror M_3)
r_{ext}	External amplitude reflection coefficient
R_{sp}	Spontaneous emission
S	Photon density in the laser cavity
t	Time
t_{avg}	Average time between fringes
V	Cavity volume
v_{g}	Laser cavity group velocity
V_{P}	Effective cavity volume occupied by photons, $V = V/\Gamma$
V_{T}	Laser terminal voltage

Introduction

Self-Mixing Interferometry (SMI) (also called Optical Feedback Interferometry) has been studied extensively in the last five decades in various sensing applications such as vibration, absolute distance, velocimetry, micro-scale flow monitoring, several biomedical purposes and acoustic pressure imaging. Sensors under the SMI technique have the laser diode as the light source, the interferometer, and the detector. The light from the laser diode propagates towards a distant target where it is partially reflected or back-scattered before being re-injected into the active cavity of the laser. When the laser diode experiences the external optical feedback, the reflected light imprinted with information from the distant target or from the external cavity medium induces perturbations to the operating parameters of the laser such as optical power, lasing frequency and the terminal voltage of the laser. For SMI measurement sensors such as harmonic motion and absolute distance applications, the fringe counting method is basically used to determine the target's displacement and distance respectively. However, it has been reported in recent years that a fringe disappearance phenomenon may occur at high feedback levels which can then strongly affect the reliability of the sensor.

Two different approaches to modelling the SMI phenomenon have been developed: the three-mirror cavity and the introduction of a slight perturbation of the rate equation that is also known as the Lang and Kobayashi model. For sensing applications purpose, the rate equation model is most often invoked and considering the frequency domain of the physical quantities (velocity, vibration, etc...) to be measured in these applications; the rate equations are simplified under the steady-state conditions. Such approximation can be made when the natural frequencies of the laser relaxation frequency and the natural resonant frequency of the external cavity. However, initial conditions and fast response of the laser can only be taken into account using a dynamic version of the rate equation model. In practice, most continuous-wave SMI systems operate in this

quasi-static regime which can be described in a single equation. The single equation that describes the phase condition imposed by the optical feedback is usually referred to as the excess phase equation and is applicable to single-mode lasers.

One of the most important and most useful parameters in the excess phase equation is the feedback parameter C that is used to categorise the regime of the laser under optical feedback. When the feedback level C is less or equal to 1, the excess phase equation presents only one solution and, the laser modal behaviour is stable. At the contrary, when the feedback level C is greater than 1, the excess phase equation has several solutions and more complex phenomena are observed such as hysteresis effect (the fringes in one or the other displacement direction are of different amplitudes), presence of multiple emission frequencies (including the unstable frequencies), mode hopping and what is at stake in the present dissertation: the fringe disappearance phenomenon.

The feedback parameter C is directly involved in the interferometric fringe disappearance phenomenon. However, to the best of our knowledge, no accurate explanations or theories on the mechanism of this phenomenon have been published so far.

In addition, measuring the distance between the laser source and the target based on self-mixing interferometry has been researched almost exclusively in the weak feedback regime; so it is still limited in practice where we need to limit the reflectivity level of the backscattered light from the target before entering into the laser inner cavity. Such a limitation is quite restraining for Light Detection and Ranging (LiDAR) applications for which other types of the interferometer are preferred. However, self-mixing interferometry is the only configuration that is self-aligned and does not need the extended mirrors or arm nor an external detector which could provide advantages in terms of costing or reliability in numerous LiDAR applications. We develop the theory describing how interferometric fringes disappear in the SMI laser sensors. The new approach in the modelling of the fringe disappearance phenomenon allows the determination of the feedback C values for which a pair of fringes are expected to disappear and as a consequence correlates the number of missing fringes to the value of C. This approach is validated both by a behavioural model of the laser under the optical feedback and by a series of measurements in the SMI absolute distance measurement.

The interferometric fringe disappearance has, so far, always been treated based on the observation of harmonic motion displacement signals. The core issue in this configuration is the unfeasibility to maintain a constant feedback level C over the target course due mostly to speckle or an imperfect alignment.

In this thesis, a novel approach that depicts the mechanism of interferometric fringes disappearance is proposed that highlights with a new perspective the impact of the coupling strength between the laser diode and the external cavity on the number of missing

fringes. An absolute distance measurement has been set where the laser diode is operated with modulation of the injection current. As compared to the vibration sensing scheme, the absolute distance approach guarantees a stable feedback parameter C thus allowing for more repeatable experimental conditions. The observed experimental results show an agreement with the proposed model on the fringe disappearance phenomenon which is based on the excess phase equation. The fringe disappearance phenomenon also occurs with the simulation of the rate equations where the coupling strength is proportional to the feedback parameter C.

Another often encountered problem in the distance measurement application is the displacement of the target (or of the sensor) that induces a Doppler shift. This Doppler shift will impact the number of fringes and their period/frequency. Such a phenomenon will occur in a self-mixing interferometer but this problem has almost not been treated in literature. Based on the modelling of the laser under optical feedback, we have carried out an extensive study on the combined effect of distance and velocity induced interferometric fringes. We show through a set of the experiment that it is possible to determine the distance and the speed of moving target at the same time.

The thesis manuscript has been written with the following structure.

A description of the non-contact distance measurement techniques is presented in Chapter 1. While sonar transmits acoustic waves, radar sends out electromagnetic waves in the radio-frequency range. The principle of both systems in distance measurement is based on the time of flight. With the introduction of optical technology, distance measurement techniques based on light waves such as triangulation, time of flight, and interferometry have been studied for many decades and used in various applications. In recent years, an optical distance measurement technique has been used the laser itself both as a source and a detector and it is called *Self-Mixing Interferometry* that will be discussed in this thesis. A state of the art of the SMI methods and performances in the absolute distance measurement application is presented in this chapter.

Chapter 2 describes the theory of the laser with external optical feedback first with the three-mirror cavity model in the quasi-static approximation then using the dynamic model derived from the rate equations. Both fundamental models can be used to characterise the self-mixing sensors in various sensing configurations but we show in the following chapters that some behaviour of the laser under feedback can only be taken into account using the dynamic model. This chapter aims especially to provide an insight into the laser field phase behaviour under the weak and the moderate regimes, where the fringe disappearance occurs. The resolution of the excess phase equation based on the boundary method gives an explicit demonstration of this phenomenon and of its dependency to the optical feedback level.

Chapter 3 discusses the use of self-mixing interferometry for metrology in absolute distance application and the behaviour of laser diode under different optical feedback regimes. The measurement of distance based on the SMI technique can be achieved when the laser emission frequency is modulated with an ostensibly triangle waveform. This frequency modulation can easily be obtained by modulating the laser injection current. With a fixed amplitude of current modulation at a certain frequency modulation, the SMI output power waveform monitored by the internal PD results in a triangle waveform with small ripples on the modulation ramp that are the interferometric fringes. This chapter also shows the validation of the proposed model on fringe disappearance phenomenon in chapter 2 through the experimental results. There is also an important demonstration both experimentally and theoretically that the number of missing fringes in the SMI signal can be different between the first modulation ramp as compared to the others, or just after the laser experience a discontinuity in its feedback condition.

Chapter 4 explores the combination of target's distance and velocity measurement based on the self-mixing interferometry and the behaviour of the laser phase in two different scenarios where the distance beat frequency is superior and inferior to the Doppler frequency. With this technique, it is possible to discriminate the direction of the target's velocity. In this chapter, we also proposed to evaluate the feasibility of profiling a rough target surface as a basic method for this application and designed an experimental methodology.

Finally, the thesis is brought to a close with concluding remarks.

1

Introduction to Distance Measurement

Distance is characterised as a quantity between two separate points. Measuring distance is probably one of the earliest measurements that have been performed by humans, and it becomes essential for many areas of science and technical applications. The standard direct measurement of distance, which designates the direct comparison of the distance with an adjusted ruler, is the oldest and most well-known method; but it is not applicable in many cases. Consequently, various indirect distance measurement procedures are expanded over the centuries where any distance can be obtained depending on measurement techniques rather than to access the distance itself by using physical contact. The most critical subgroup of indirect distance measurement is a non-contact distance measurement, as many technical applications require distance measurement through the non-physical contact between the source and the object. Furthermore, the non-contact measurement technique has the advantages that the contamination of the contact point does not occur to the measuring device; however, errors of the measurement are likely to rise because of several factors (for example, the surrounding environment and the measurement methods). Then the non-contact distance measurement becomes one of the most interesting research topics as many areas of technology relies on the ability of accurate determination. There are several techniques of non-contact distance measurement such as using sonar, radar and optical-based methods as shown in Figure 1.1. With the introduction of optical technology, non-contact distance measurement methods based on light waves have been studied for many decades and used in various applications such as automotive industrial, metrology and non-contact surface profiling due to their ability to make a highly accurate and precise measurement. Beside of measuring the physical length between the source and object, some of the optical techniques are capable of measuring the related parameters such as displacement, surface's profile, velocity, and

vibration. Variations in parameters of the laser light such as power density, polarisation, wavelength, spectrum, phase, and light propagation direction after interacting with a target can provide the information on a variety of processes. Each individual technique of non-contact distance measurement will be described in the following sections.

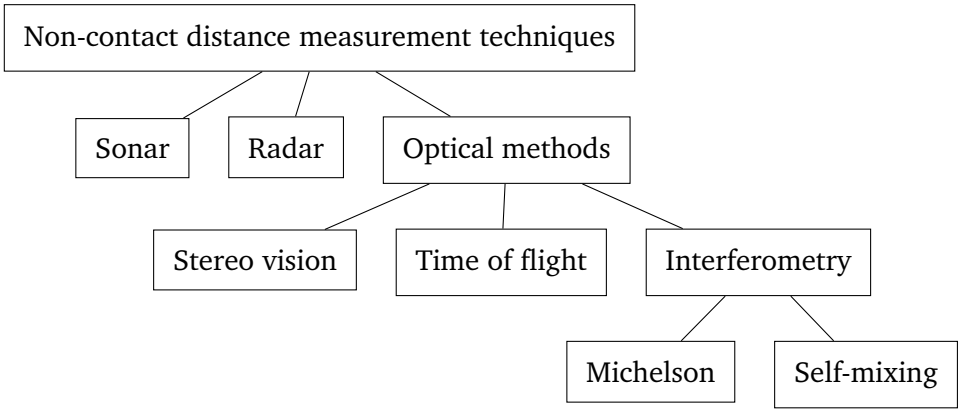

Figure 1.1: Non-contact distance measurement techniques.

1.1 | Sonar and Radar

1.1.1 | Sonar

Sonar (Sound Navigation And Ranging) systems are used to navigate, communicate with detectable objects on or under the surface of the water application. The knowledge and understanding of underwater sound were discovered in 1490 by Leonardo Da Vinci where he wrote: “If you cause your ship to stop, and place the head of a long tube in the water and place the outer extremity to your ear, you will hear ships at a great distance from you.” It was then invented and developed in 1912 as a direct consequence of the loss of *Titanic* in the basic requirement of detecting icebergs in 2 miles distance [13]. The principle of distance measurement with sonar technology is based on the time of flight (TOF) of the sound wave that propagates from the sonar device and travels forward to the object [14]. As shown in Figure 1.2, the sound as an acoustic wave travels through the supporting medium (air, water, etc.) with the propagation speed towards an object and then the wave is partially reflected. The reflection of the wave is detected that enables to measure the time between the sending to the receiving of the sound impulse [13]. The distance between the sonar device and the reflector can be estimated as follows,

$$L_{\text{ext}} = \upsilon . \frac{\tau_{\text{TOF}}}{2}, \tag{1.1}$$

where L_{ext} is the distance from the sonar device as a transmitter to the object as a target in meter (m), τ_{TOF} is the time delay between the sending and the receiving wave to the measurement signal in second (s) and v_{sound} is the velocity of the propagation wave in meter per second (m/s). The sound propagation velocity in the air can be defined as [14],

$$v_{\text{sound,air}} = 331.4\sqrt{\frac{\text{T} + 273}{273}} \quad \text{m/s}, \tag{1.2}$$

where T is the temperature in degree Celsius in the measuring condition.

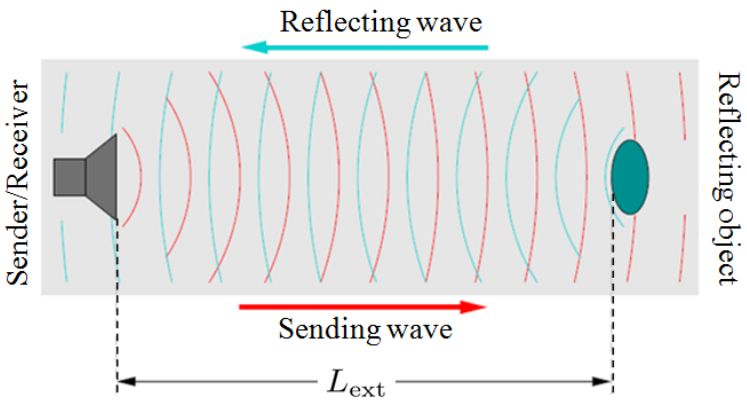

Figure 1.2: Principle of sonar distance measurement.

Sonar has been used in various applications and its frequencies range from infrasonic to above a megahertz. Normally, the lower frequencies are used for long-distance applications, while higher frequencies are used for shorter distance as it provides better resolution [13, 15]. For example, a frequency of 20 Hz has been used for long-distance sonars in submarines, while over 40 kHz of ultrasonic distance sensors are used in the automotive and industrial field and up to 1 MHz−40 MHz are found in diagnostic ultrasonic imaging in the medical ultrasound or diagnostic sonography.

The main disadvantages of this technology are the wide beam that causes poor directional resolution, the low repetition rate of the measurement resulting from the comparative slow propagation speed of sound in comparison to the electromagnetic wave and optical sensors and the random fluctuations that can be detected in the echo propagation time which depends on the measuring environment [16].

1.1.2 | Radar

Radar (Radio Detection and Ranging) technology for the distance measurement, again, based on TOF measurement. The difference between sonar and radar is that radar

uses electromagnetic waves in the radio-frequency range. Here, the radio signal of microwaves is used as a measuring signal whose TOF between the source of the wave and the object is detected [17].

High accurate distance measurement, in this case, requires a high-speed and very accurate evaluation electronics as the propagation velocity of electromagnetic waves travels at the speed of light ($c \approx 3 \times 10^8\,\mathrm{m\,s^{-1}}$) leading to a very short time delay between the emitted as received impulses. The distance measurement resolution and the characteristics of the received signal rely on the shape of the pulse which is often tailored to achieve better performance.

Radar distance measurement is used in a variety of applications ranging from short to very long distance. Examples are distance measurement for automatic cruise control in automobiles (up to 250 m) and air traffic surveillance (up to 500 km). Frequency modulation is another form and more accurate of the distance measurement based on Radar technique. Beside of the distance measurement, radar has the advantage of having the ability to measure the velocity of the target by evaluating the Doppler shift of the signal and it also can tell whether the object was in motion or stationary. Beside of those advantages, the radar system also faces some disadvantages such as their poor angular resolution properties, wide and no target specific beam range that leads to not be able to distinguish or resolve multiple targets.

1.2 | Triangulation

Triangulation optical method to determine the distance between the sensor and the object is based on the consideration of the geometries triangles that was used around 600 BC to measure the height of the pyramid of Giza and the distance to a ship at sea [18]. Triangulation technique is a geometrical approach where the target is at one point of the triangle while another two points are known by the measurement device. Then the distance between the source and the target can be calculated by determining the angle of the triangle. With the presence of optical technology, triangulation method can provide the depth information and generate 3D image data of a scene using a standard 2D imaging system. Two very common triangulation-based optics are passive triangulation (known as stereo vision) and active triangulation.

1.2.1 | Stereo vision

With the conception of roughly estimating the distance and size of an object with the human eyes approach, the stereo vision method has been adapted by using two cameras

to observe a scene from several viewpoints for building a 3D description. Stereo vision is considered as a passive technique as the measuring system does not illuminate the target; instead, the reflected light from the target is either reflected ambient light or the light produced by the target itself. Figure 1.3(a) shows two cameras aligned on a common axis separated by a distance b that observe an object while the two observation angles α and β from the right and left camera, respectively, are known. The distance from the cameras axis to the observed object, L_{ext}, can be calculated by the disparity equations which are written as [19],

$$\begin{aligned} p &= x_1 - x_2 \\ &= f.\tan\alpha - f.\tan\beta \\ &= f.\frac{y + b/2}{L_{\text{ext}}} - f.\frac{y - b/2}{L_{\text{ext}}} \\ &= b.\frac{f}{L_{\text{ext}}}. \end{aligned} \tag{1.3}$$

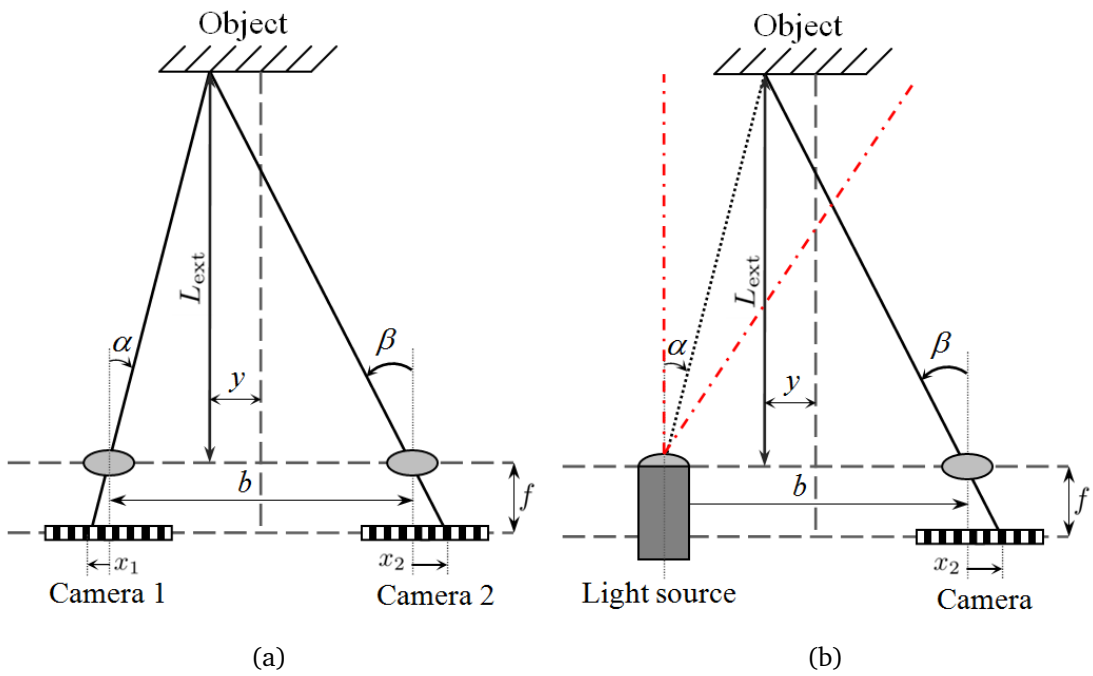

Figure 1.3: Principle of triangulation-based optical sensors: (a) Passive Triangulation (Stereo Vision); (b) Active Triangulation.

The distance L_{ext} in Eq. (1.3) can be simply calculated by replacing the disparity p of the object with the positions x_1 and x_2 of the imaging sensor camera 1 and camera 2,

respectively; so that,

$$L_{\text{ext}} = \frac{b.f}{p} = \frac{b.f}{x_1 - x_2}. \tag{1.4}$$

The disadvantage of this method is the requirement of two cameras. The larger the distance to be measured is, the longer the requirement basis width between two cameras becomes in order to maintain the resolution of the measurement. The resolution of this technique can be found as,

$$\Delta L_{\text{ext}} = \frac{b.f}{p^2}.\Delta p = \frac{L_{\text{ext}}^2}{b.f}.\Delta p. \tag{1.5}$$

Shadowing effects may be the typical problems with this system, but it can be minimised by enlarging the number of cameras known as multiple viewpoint triangulation systems where this improvement has to be paid for by an enormous increase in computation. Stereo vision method can be useful for certain defined scenes, preferably chosen with rich contrast and relatively flat surfaces for the identification of identical points in the two pictures. For this reason, for some typical scenes, it may not be suitable for the measurement.

1.2.2 | Active triangular

Contrary to the stereo vision technique, active triangulation uses only one camera to capture the scene and a light source instead of a second camera where it is used to illuminate the object to be measured as shown in Figure 1.3(b). Thus again, a form of the triangle is composed by a camera, a light source at the distance b, and the object to be measured. The direction of the light source by means of the angle α has to be known to measure the distance L_{ext}. The detecting camera, either a position sensitive detector (PSD) or colour coded triangulation (CDD), is used to determine the location of the object. Moreover, the determination of the distance here is very similar to the stereo vision technique in Eq. (1.3); so that,

$$L_{\text{ext}} = \frac{b.f}{p} = \frac{b.f}{f.\tan\alpha - x_2}. \tag{1.6}$$

Small distance to be measured, a large triangulation basic width b and a good resolution detector Δx_2 are required to obtain a high resolution in this technique. The distance resolution can be determined by,

$$\Delta L_{\text{ext}} = \frac{d^2}{b.f}.\Delta x_2. \tag{1.7}$$

Commercial device available for active triangular distance measurement sensors integrates the light source and the detector in the same package which results in a limitation

of the measuring ability, approximately from 10 mm to 1 m [18]. It generally uses a laser diode as the light source which the measurement resolution is depending on the laser beam size and the detector pixel size. Similar to the stereo vision technique, the resolution is limited where the highest resolution may be found close to the minimum sensing distance. It is interesting to know that when the measuring object increases the distance, the measurement resolution also continuously decreases.

The advantage of this sensor is its low price and fast measurement (tens or hundreds of kiloHertz refreshing rate are possible). Besides these advantages, this method has a limitation as they are not operating well with transparent objects (such as glass, water or liquid surfaces) offering a poor visibility of the laser spot. Another problem of this approach is the sensitivity towards the ambient light that may disturb the measurement.

Triangulation distance measurement systems are available in various application from millimetre range (depth in focus) to 100 km range (photogrammetry). The main difficulty of this system is that for a better resolution, the size has to be increased since it needs a large triangulation base. However, the larger the triangulation base is the more the systems are restricted by shadowing effects. Furthermore, the 3D triangulation is more expensive since the fast LCD projectors are required in the active triangulation as well as the ability of computation.

1.3 | Time of flight

Besides using sound waves (SONAR) or microwaves (RADAR) presented in section 1.1 to measure the distance with Time of Flight (TOF) methods, several TOF distance measurement procedures using light are also developed. With a similar concept, photons are emitted from the light source to the measured object to compute the distance by calculating the time which they need to propagate to the object and return to the detector device [20]. The active light source and the receiver are normally located close to each other which facilitates a compact setup and avoids the effect of shadowing. One of the well-known distance measurement based on TOF using light is LiDAR. LiDAR was originally understood as laser radar but is nowadays used as a general acronym meaning light detection and ranging [1, 21]. The introduction of the LiDAR principle dates back before the invention of the laser. In 1938, the measurement of cloud base heights was conducted for the first time by using the pulses of light [21]. Then the rapid development of modern LiDAR technology began with the invention of the laser in 1960. Ever since, LiDARs have been developed and used in many applications with the progress in optical and electronic technology, in particular laser technology. A LiDAR consists essentially

of five subsystems: (1) a transmitter that generates short light pulses with lengths of a few to several hundred nanoseconds and specific spectral properties, i.e., in all practical cases a laser; (2) a transmitter optic (a beam expander) is used to reduce the divergence of the light beam and to reduce the area density of the laser pulse energy before it is sent out into the atmosphere; (3) a receiver optic is used to collects the photons backscattered from the atmosphere and focuses it onto the detector ; (4) a detector; and (5) an electronic system for data acquisition, processing, evaluation, display, and storage. The LiDAR's configuration is displayed in Figure 1.4. Most LiDARs have additional components depending on the type and purpose. There are two types of LiDAR's system: (1) *monostatic* where the transmitter and the receiver are at the same location; and (2) *bistatic* where the transmitter and the receiver are separated by a fixed distance (usually more than several tens of meters) and a continuous wave laser can be used as a light source. TOF based on optical system use either *direct TOF pulsed based method* or *indirect TOF phase-shift based method*, and both principle methods have their specific advantages and disadvantages which will be discussed in the following sections.

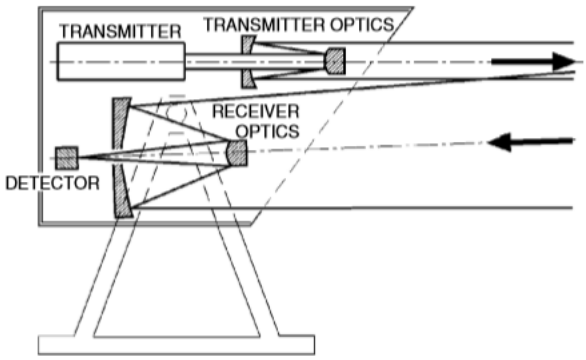

Figure 1.4: Essential optical components of a LiDAR system [1].

1.3.1 | Pulsed based direct TOF distance measurement

The direct TOF distance measurement methods take into account the time of flight of a single light pulse to determine the distance between the source and the object. The actual time determination is achieved by correlation of a start and stop signal by using a high-speed counter. The emitted pulse (typically 2 ns - 50 ns) goes through to a beam splitter which directs some fraction of the light to the first photodetector as an indication of *start* pulse to the counter, and the remaining fraction of light travels to the target in a medium with refractive index n_{ext}. The back-scattered light from the target travels back to the second photodetector to produce the *stop* pulse for the counter. Then, the

travelling time between the start and stop pulses is the TOF and the distance between the source and the target can be determined by [22],

$$L_{\text{ext}} = c\frac{\tau_{\text{TOF}}}{2}. \tag{1.8}$$

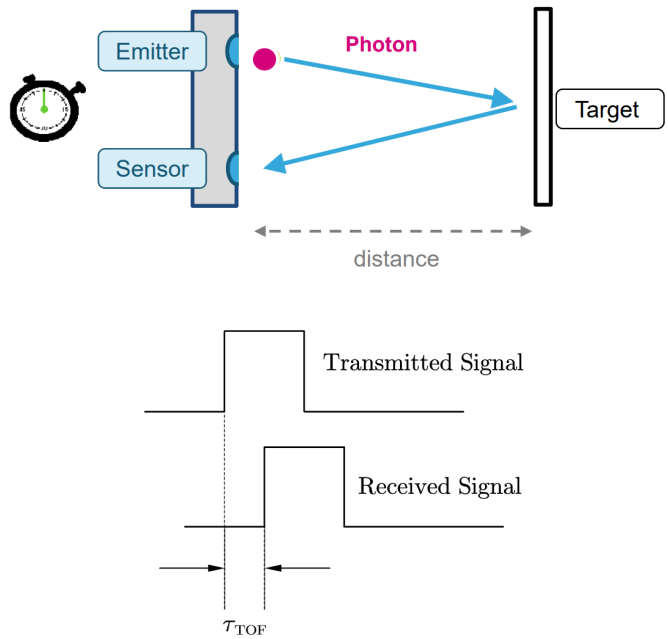

Figure 1.5: Principle of direct TOF distance measurement method [2].

Due to the complexity of detection and evaluation electronics such as the time jitter of the photodetectors, a variation of rising time and the electronic noise in the pulse, high-resolution measurement using this technique is a challenging issue even when the target is stationary. The pluses typically have durations of a few nanoseconds or sometimes even below 1 ns when using particularly compact lasers, e.g. monolithic passively Q-switched microchip lasers. Then a fast photodiode to capture the back-scattered light from the target is needed which is generally for very low received optical powers resulting from the large observation distances. As the distance of target increases, the beam divergence may lead to a substantially increased spot on the object, and atmospheric distortions cause decreasing the amount of back-scattered light illuminating the second photodetector which results in the stop pulse to be noisier contributing to the alteration of measurement resolution.

The improvement of the distance measurement based on this technique depends on several factors :

- A higher amount of energy can be transmitted in a very short time. However more concerned about the safety of the measurement environment is to expect which is a limited criterion for some measurement applications.
- A telescope can be used to increase the beam radius at the output aperture and reduce the beam divergence. The same telescope may be used to collect more light from the object. However, this approach may be limited by compactness and low weight requirement of the device.
- With some precisely aligned mirror or a kind of retroreflector set on the target, the light signal is much stronger but many applications require the operation with diffusely scattering objects.
- Eventually, the sensitivity of the photodetector, optical bandpass filtering and signal processing are key elements in the sensor performance.

1.3.2 | Phase-shift based indirect TOF distance measurement

The technique based on phase-shift estimation is based on the evaluation of the phase difference between the intensity-modulated transmitted and received waves. The source (i.e., laser or LED) emits the light pulses at a specific wavelength and frequency in which the intensity is modulated (commonly with sinusoidal modulation waveform), and the backscattered light to the detector has a phase shift with regards to the emitted one. The phase shift is used to determine the distance rather than directly measuring a light pulse's round-trip time. It can be determined as [23],

$$L_{\text{ext}} = c\frac{\varphi T}{4\pi}, \tag{1.9}$$

where T represents the full period of the signal modulation. Since the distance measurement is now made through a phase-shift measurement, the resolution $\delta\phi$ of the latter will necessarily have an impact on the resolution δL_{ext} of the first. Both parameters are indeed linked by,

$$\delta L_{\text{ext}} = \frac{c}{2}\frac{\delta\varphi T}{2\pi}, \tag{1.10}$$

Since the transmitted and received signals are periodic with the same frequency, then the observed phase-shift is limited between 0 and 2π. This method is more likely suitable for short-distance measurement in the tens of meters range. It is reported recently that this technique was able to measure the absolute inter-vehicles distances up to 25 m with a resolution under 10 cm, and up to 30 m with 30 cm resolution at a refresh rate of 267 Hz. The measurement range can be increased up to 50 m with an error over 1 m [23].

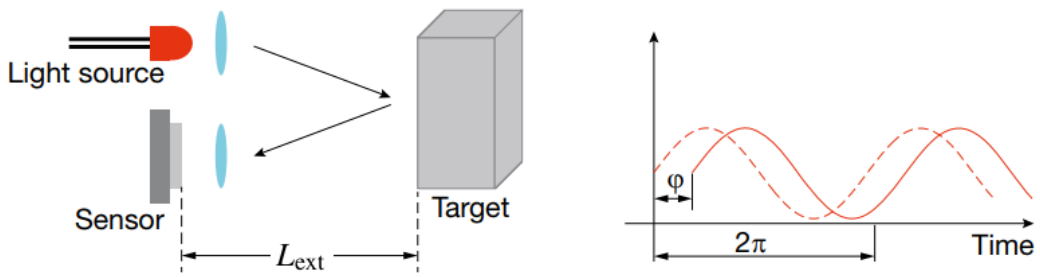

Figure 1.6: Principle of phase-shift distance measurement method [2].

1.4 | Interferometry

Interferometry is a very precise technique to measure the distance. This technique is based on the interference of the optical waves. The basic principle of distance measurement using interferometry was demonstrated for the first time by Michelson in 1892 when the wavelength of the red light from cadmium of the International Prototype Metre was measured [24]. There are many types of interferometers using various techniques; mostly laser is used as a light source and it normally is monochromatic and mono-directional. The basic principle of the interferometer technique is a superposition of two optical waves with the same wavelength. The resulting intensity of this superposition is determined by the difference in phase of those two optical waves. Each design of interferometer is suited to a particular environment and situation and it has certain advantages and disadvantages.

1.4.1 | Michelson interferometry

A basic representation of an interferometry technique is Michelson interferometry that a light wave with a certain lasing frequency coming from a light source is divided at a semi-transparent mirror or beam splitter into two parts—the reference arm and the measuring arm, schematically shown in Figure 1.7. The first part is deflected towards a mirror called a reference target with the calibrated distance and then is reflected back. The second part travels from the semi-transparent mirror to the measuring object as a target and some fraction of lights backscatters. The reflected light from both the reference and the measuring target recombines at the semi-transparent mirror into a single resulting wave and travels to the detector [25]. The detected signal by the detector contains the relative distance information of the measuring target. By evaluating the phase shift, $\Delta\varphi$,

of this signal, the relative distance can be calculated by,

$$\Delta L_{\mathrm{ext}} = c\frac{\Delta\tau_{\mathrm{TOF}}}{2} = c\frac{\Delta\varphi}{4\pi}\frac{1}{\nu_{\mathrm{th}}}, \tag{1.11}$$

where ν_{th} is the lasing emission frequency and ΔL_{ext} is the variation of the target distance and also represents the optical path difference (OPD). The OPD ΔL_{ext} is indeed double the difference in distance between the two arms of the interferometer system, as the light beam travels the distance as a round-trip. Then the distance can be measured as [26],

$$\Delta L_{\mathrm{ext}} = 2(L_{\mathrm{R}} - L_{\mathrm{ext}}), \tag{1.12}$$

where L_{ext} is the measuring distance of the movable target and L_{R} is the distance of the reference arm.

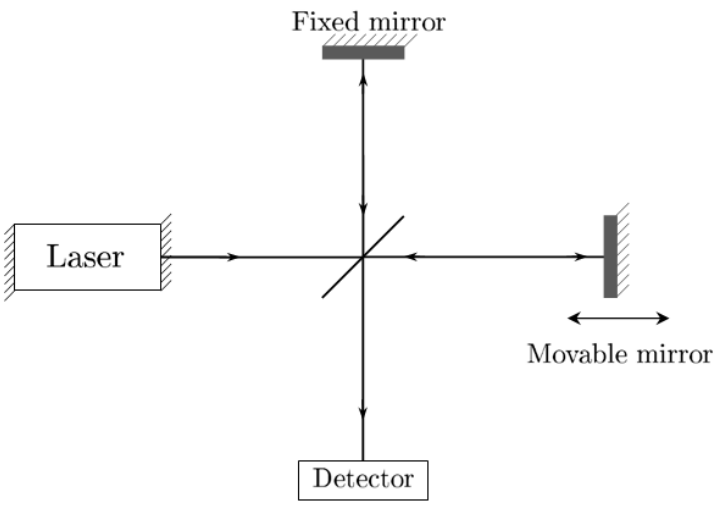

Figure 1.7: Principle of Michelson interferometer.

With up to $\lambda/100$ the achievable distance resolution is in the range of a few nanometres. The problem is only possible within a range of half-wavelength. To solve this problem, several techniques based on Michelson interferometry has been proposed.

1.4.1.1 | Multiple wavelength interferometry

Multiple wavelength interferometry technique was first proposed by Benoit [27]. The typical system setup is based on Michelson interferometer. It is performed by comparing a mechanical length (or a distance in space) against a known wavelength of light. Typically,

the optical components are arranged such that the light beam double-passes the required distance are half-wavelengths. Then, the target distance can be expressed as [28],

$$L_{\text{ext}} = \frac{1}{2}\lambda_{\text{th}}(i + \epsilon), \tag{1.13}$$

where λ_{th} is the laser emission frequency, i is the integer order and ϵ is the fraction order of interference ($0 < \epsilon < 1$). The concept of this technique is based on the observation of the interference intensities of two or multiple light waves. In the case of two beams interference, the interference intensity can be written as,

$$I = I_0\Big[1 + \gamma \cos\Big(\frac{2\pi n_{\text{ext}}}{\lambda_{\text{th}}/2}(z_1 - z_2)\Big)\Big], \tag{1.14}$$

where γ is the interference contrast and $z_1 - z_2$ is the difference between two optical pathways and n_{ext} represents the external refractive index within the path. Once the movable mirror is moving, the interference fringes cross a detector are countable. However, due to the short wavelength of light, the distance between the two measuring points has to be smaller than a half-wavelength. Then single-wavelength interferometry has been proposed by using two different wavelengths, λ_1 and λ_2; so the difference between the two interferometric phases act as a single phase of a synthetic wavelength that is expressed as $\Lambda = \lambda_1\lambda_2/(\lambda_1 - \lambda_2)$ which is longer than both optical wavelengths. The fringe counting method is not necessary within half of this synthetic wavelength which then the resolution of the distance measurement is uncertainty increased. The errors of measurement in this technique include the alignment of the path, the variation of the laser wavelength, the effect of the refractive index and the accuracy of the fringe interpolation performed in computation.

1.4.1.2 | Wavelength scanning interferometry

Wavelength scanning interferometry is another optical interferometric technique to measure the absolute distance which is dating back to the 1980s [29, 30] and it is continuously studied until more recently. A typical wavelength scanning interferometry setup is based on the Michelson interferometry technique as shown in Figure 1.7. Wavelength scanning/shifting interferometry, frequency sweeping/scanning interferometry, swept wavelength interferometry, optical frequency domain reflectometry, frequency modulated continuous wave and variable synthetic wavelength are all the synonym terms which rely on the same basic principle. When the intensity of the reference target and the measuring target are combined at the semi-transparent mirror, the intensity of the

interference pattern on the detector can be found as [31],

$$I(t) = I_1 + I_2 + \sqrt{I_1 I_2} \cos\left(\frac{2\pi\nu L_{\text{ext}}}{c}\right), \tag{1.15}$$

where I_1 and I_2 are the intensity in each arm of the interferometer and v represents the laser emission frequency. The term $2\pi\nu L_{\text{ext}}/c$ is known as the phase of the interferometer and is denoted by φ. The principle of the wavelength scanning interferometry is that by scanning the fluctuation of the frequency of light, $\Delta\nu$. Then the variation in the phase can be written as,

$$\Delta\varphi = \frac{2\pi}{c} L_{\text{ext}} \Delta\nu. \tag{1.16}$$

There are two main approaches to calculate the OPD. The first method is to determine the changes in the phase and frequency, then calculate the OPD directly [32]. The second method, which is more common [33, 34], is to calculate the unknown optical path difference with two combined interferometers, one of which (known as the reference interferometer) has a pre-determined OPD. Then the dividing between the two different phases gives,

$$\frac{\Delta\varphi_{\text{M}}}{\Delta\varphi_{\text{R}}} = \frac{L_{\text{ext}}}{L_{\text{R}}}, \tag{1.17}$$

where $\Delta\varphi_{\text{R}}$ and $\Delta\varphi_{\text{M}}$ are the phases fluctuation of the reference and measuring interferometer, respectively.

The disadvantages of the wavelength scanning interferometry are the non-linear laser tuning and the sensitivity to the vibration and environmental disturbances during measurement. Various approaches have been proposed to reduce the non-linear effect during tuning. Then, the heterodyne technique has been used to reduce the disturbance due to the environment of measurement. Recently, wavelength scanning frequency and multiple wavelength interferometry have been combined to measure the absolute distance.

Both described techniques are based on the Michelson interferometry where the external arms (mirrors) and an external photodiode are required. The disadvantage of this technique is that the precise alignment is required between the laser, beam splitter, reference mirror, and photodiode. The error of absolute distance measurement tends to increase with this configuration setup. However, new optical distance measurement based on interferometry can solve this problem where the sensor and the measured object are self-aligned. This technique is called self-mixing interferometry where the laser itself acts both as a source and a detector and this technique will be presented in this thesis.

1.4.2 | Self-mixing interferometry

1.4.2.1 | Definition and applications

In recent years, a new optical distance measurement technique has been used the laser itself both as a source and a detector. This technique is commonly called Self-Mixing Interferometry (SMI) or Laser Feedback Interferometry (LFI) [11, 35]. The optical feedback effect is especially troublesome in semiconductor laser diode due to their very high gain and low facet reflectivity. Some researchers view the extreme sensitivity of the laser diode due to the external optical feedback as an opportunity rather than a nuisance. The self-mixing interferometry has been researched extensively in the last five decades in various sensing applications [11, 36] such as vibration [37, 38], absolute distance [4, 9], velocimetry [39, 40], micro-scale flow monitoring [41], several biomedical purposes [42, 43] and acoustic pressure imaging [44]. Sensors based on the SMI technique have the laser diode as the light source, the interferometer and the detector. All lasers with self-mixing systems operate based on the same basic principle: the light from the laser diode propagates towards a distant target where it is partially reflected or backscattered before being re-injected into the active cavity of the laser. When the laser diode experiences the external optical feedback, the re-injected light imprints with information from the target through the perturbation of the laser operating parameters such as gain, optical power, lasing frequency and the terminal voltage of the laser [11, 45]. This detection technique also leads to a lower cost and higher robustness as it does not require any reference arm or external detector, it is an almost self-aligned setup. Figure 1.8 gives a schematic of the self-mixing interferometer.

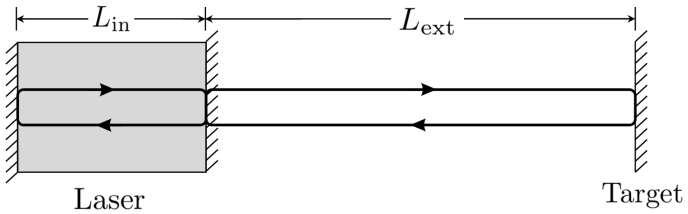

Figure 1.8: Principle of Self-Mixing interferometry.

1.4.2.2 | Historical development of the SMI effect in distance measurement

The SMI phenomenon was first demonstrated after the invention of the laser by King & Steward in 1963 [46]. They observed the variation in the output power of a He-Ne laser when the distance of the external mirror changes and the output power was periodic with the distance to the external mirror with a period of half wavelength of the laser.

The effect was observed when as little as 0.1% of the emitted radiation was reflected from the external mirror placed up to 10 m from the operating laser in continuous wave mode. Later, Barchert & Raab observed the change in behaviour of the threshold carrier density in the semiconductor laser in 1968 [47]. In the same year, Morosov *et al.* also reported that the change in the threshold of a semiconductor laser was dependent on the distance to the external mirror and that it affects its dynamical properties [48]. However, there was no theoretical model that could accurately describe the fundamental of the dynamical operation of a semiconductor laser under the optical feedback until it was addressed by the work of Land and Kobayashi in 1980 [49]. They presented the famous core model for a semiconductor laser experiencing optical feedback that induces dynamical changes in the carrier density. In the same paper, Lang and Kobayashi also explained that this information could be used to describe the dynamical behaviour in the laser output power under the optical feedback.

Later, researchers began to recognise that the SMI could also be used for metrology applications. The first demonstration was done by Dandridge *et al.* in 1980 by using the semiconductor laser with the optical feedback to measure the displacement of a target [50]. The output power of the semiconductor laser showed periodically of the target distance for a constant operating injection current. Moreover, in 1984, Chrunside used optical feedback with a CO_2 laser to measure velocity [51].

In 1986, Shinohara *et al.* demonstrated laser Doppler velocimetry using the SMI in a semiconductor laser introducing the term "self-mixing" [52]. In the same year, Beheim *et al.* demonstrated the SMI absolute distance and velocity measurement by modulating the laser emission frequency [53]. When the laser emission frequency without optical feedback called free-running frequency, ν_{th}, is tuned by modulating the laser injection current, and the laser itself experience with the optical feedback, mode hops occur which produce the discontinuities in the laser output power and are readily detected by differentiating the signal from the laser power monitor. Beheim proposed the determination of the distance between the laser and the target and the velocity by counting the number of mode hops N_{f} that resulted from a laser frequency variation of magnitude $\Delta\nu_{\mathrm{th}}$. When the object is fixed at a distant target with any motion, the number of mode hops at the optical output power in each semi-period of the triangle modulation waveform is normally equal; and the distance between the laser and the target can be determined as,

$$L\mathrm{ext} = \frac{c}{4\Delta\nu_{\mathrm{th}}}(N_{\mathrm{f1}} + N_{\mathrm{f2}}), \tag{1.18}$$

However, the object moves along the longitudinal axis of the laser beam either moving forward or backward to the laser, the number of mode hops at the optical power in each semi-period of the triangle modulation waveform is no longer equal; and this lets us

determine the velocity of the target that is expressed as,

$$v = \frac{\lambda_{\mathrm{th}}}{4T}(N_{\mathrm{f2}} - N_{\mathrm{f1}}) \tag{1.19}$$

where N_{f1} and N_{f1} are the number of mode hops during the upward and downward of the triangle modulation.

In their experiment, a single-mode laser diode lasing at 845 nm and a monitoring photodiode within the laser package are used to determine the distance and velocity of the target. The laser diode is modulated with the triangle waveform of 6 mA of amplitude at around 35 Hz of frequency modulation. Two different kinds of the target are used in this experiment−white paper and Scotchlite (a flexible retro-reflective material with high reflectivity). They observed that the accuracy decreases with the external distance of the target, i.e, from 60 to 100 cm the uncertainty in the mode hops N_{f} is ± 2, and from 110 to 150 cm the uncertainty is ± 4.

In the same paper, they introduced the combined effect of target motion and laser injection current modulation based on self-mixing technique. The target was placed on a motor-driven translator at a 9 cm range and moved in the direction of z-axis along the longitudinal dimension of the laser cavity with a speed of $\pm 210\,\mu\mathrm{m\,s}^{-1}$. In the presence of the motion target, the number of mode hops between the upward and downward triangle modulation in the output power got different results. Based on these results, the external distance from the target and its velocity can be calculated at the same time. This article became a fundamental of the research in self-mixing interferometry with the laser frequency modulation for absolute distance measurement.

In 1990, Sinohara *et al.* used the same technique by modulating the laser diode injection current in a symmetrical triangle waveform [54]. However, instead of using the number of mode hops in the optical output power to measure the external distance, they measured the mode hop time interval in the purpose of obtaining higher accuracy and wide dynamic range simultaneously. The absolute distance in Eq. (1.20) is computed as,

$$L\mathrm{ext} = \frac{cT}{4\Delta\nu_{\mathrm{th}}T_{\mathrm{M}}}, \tag{1.20}$$

where T_{M} is the mean value of the $N_1 + N_2$ mode hops time interval and it is expressed as,

$$\frac{1}{T_{\mathrm{M}}} = \frac{(N_1/T_1 + N_2/T_2)}{2}, \tag{1.21}$$

In addition, they also improved the measurement resolution by reshaping the current modulation waveform using an RC integrator. Their experimental resulted in high precision of $\pm 0.13\%$ in a wide dynamic range of 0.2 m to 1 m of the external distance.

Both Sinohara and Beheim used the current modulation to change the laser frequency. The laser emission frequency and the injection current are linked through a parameter known as frequency modulation coefficient (GHz/mA). This parameter has been studied by Chrisphe Gorecki in 1996 [3]. In his experiment, a Sharp LT080 laser lasing at 782 nm was linearly modulated to evaluate the frequency modulation coefficient. His experimental results show that the frequency modulation coefficient slowly decreases between 50 Hz and 5 kHz, and tends to decrease sharply from 5 kHz to 1 MHz as shown in Figure 1.9. He explained that optical feedback may seriously impact the dynamic properties of the laser diode. It had also been demonstrated by Lang and Kobayashi that the laser diode output power and the wavelength vary with the distance between the laser diode and the external reflecting surface [49].

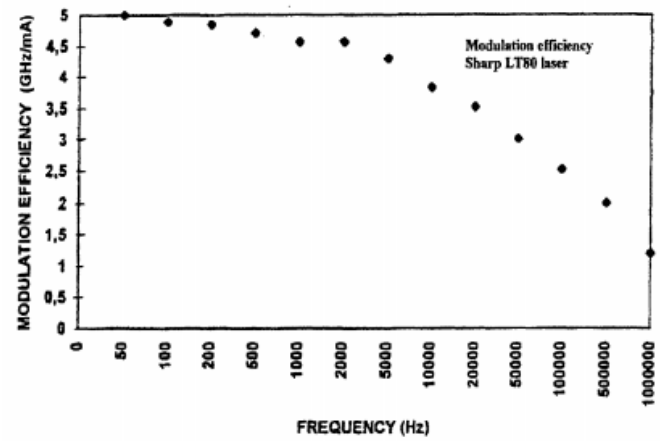

Figure 1.9: Frequency modulation coefficient of short-external-cavity Sharp LT080 laser [3].

Gouaux *et al.*, in 1998, have improved the measurement accuracy to ± 1.5 mm with the external distance range from 50 cm to 2 m by taken into account of the thermal effects in laser diode [4]. In their experiment, a laser diode lasing at 799 nm of wavelength was operated with an injection current of 100 mA and modulated with a triangle waveform under an optical frequency excursion of 36 GHz. Without the current reshaping, the laser emission frequency did not change linearly with the injection current which resulted in resolution ± 4.16 mm of distance measurement while using the fringe-counting method.

To improve this measurement resolution, the influence of the current-reshaping thermal effect can be removed by the introduction of the complex transfer function. This reshaped laser injection current gave the laser emission frequency purely triangle. However, their measurement results were determined when the laser diode was operated in weak optical feedback by means of the feedback parameter $C < 1$. For stronger feedback,

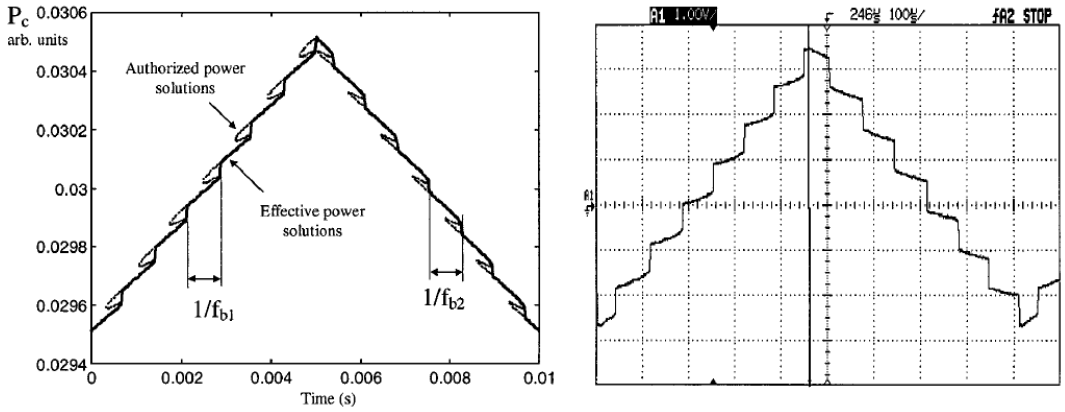

Figure 1.10: Laser optical power with hysteresis for an absolute distance measurement both theoretical and experimental result [4].

the experimental results showed that the laser diode remained in single mode, however, the optical power showed hysteresis as shown in Figure 1.10.

In the same year, based on the experiment of Gouaux's paper, Bosch *et al.* designed a self-mixing type scanning range finder to construct three-dimensional (3D) images of an object [55]. In their experiment, the target, a plastic screw, was located 1.971 m away from the laser diode. Then the 3D image was obtained with a size of 100×100 pixels as shown in Figure 1.11.

Later, in 2000, Wang *et al.* proposed a new method by using the same laser injection current modulation technique, but the Fast Fourier Transform was applied to determine the external distance [5]. An experiment using two external mirrors—a reference mirror at the distance L_1 and a target's mirror at an unknown distance L_2 is shown in Figure 1.12.

As it is a double external cavity, the frequency of the fringes are defined as,

$$f_1 = \frac{2\Delta\nu_{\text{th}} L_1}{cT}, \tag{1.22}$$

$$f_2 = \frac{2\Delta\nu_{\text{th}} L_2}{cT}. \tag{1.23}$$

By knowing the external distance of the reference mirror, the unknown external distance being measured can be determined as,

$$L_2 = L_1 \frac{f_2}{f_1}. \tag{1.24}$$

In this experiment, a laser diode lasing at 780 nm was operated with 50 mA of injection current and modulated with the amplitude of 3.5 mA at 100 Hz in a sawtooth waveform.

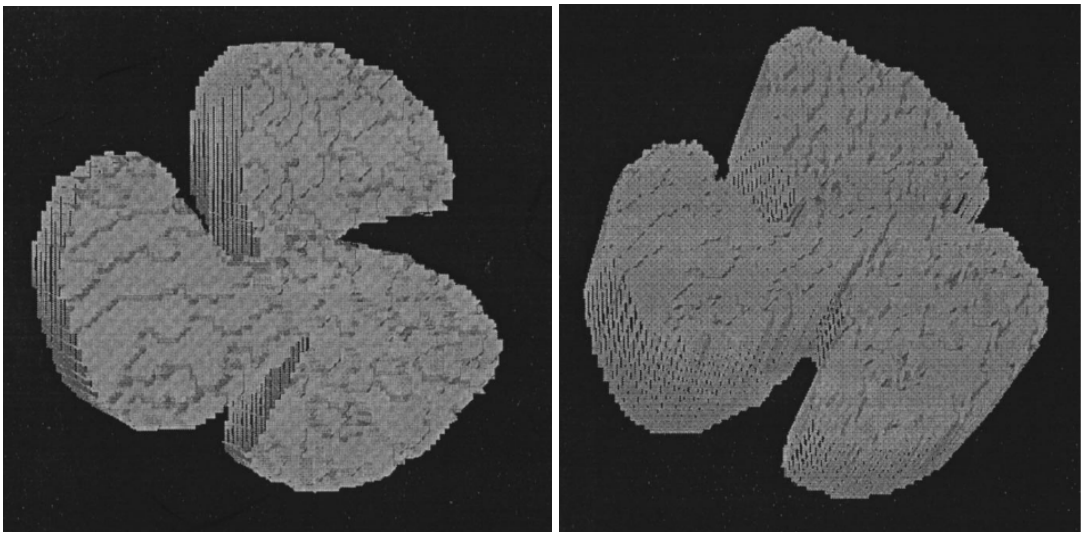

(a) (b)

Figure 1.11: (a) Front view of the screw reconstructed, (b) Another view of the target being obtained by image processing [4].

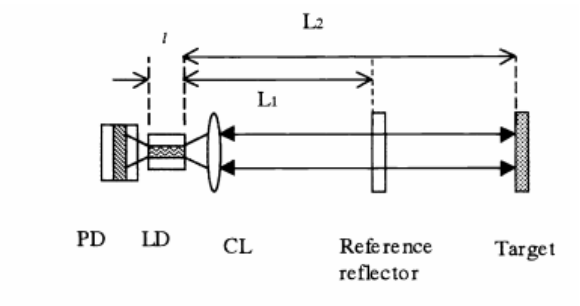

Figure 1.12: Self-mixing interferometers with double external cavities [5].

Figure 1.13(a) depicts the signal obtained by the double external cavities self-mixing interference and the plot of Figure 1.13(b) is the Fourier spectrum of the signal in (a). The distance measurement L_2 depends on the resolution in the determination of the signal frequency. The measurement accuracy was achieved at 2.5 mm with the absolute distance to be measured up to 1.25 m.

The self-mixing sensing system normally uses the photocurrent from an integrated photodiode as a detector. Then, in 2005, Lim *et al.* demonstrated that an alternative way by using the laser junction voltage as the source of the SMI signal can be used to determine the distance between the laser and the target [6]. This discovery led to potential cost saving with reductions in component costs and complexity while the same information can be obtained as the photodetector. In their experiment, the Vertical-Cavity

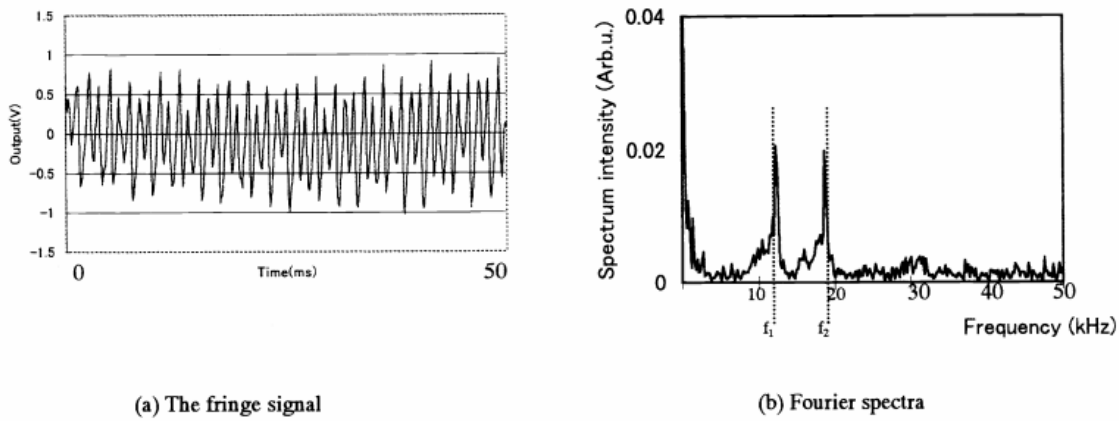

(a) The fringe signal (b) Fourier spectra

Figure 1.13: Experimental result by double external cavities [5].

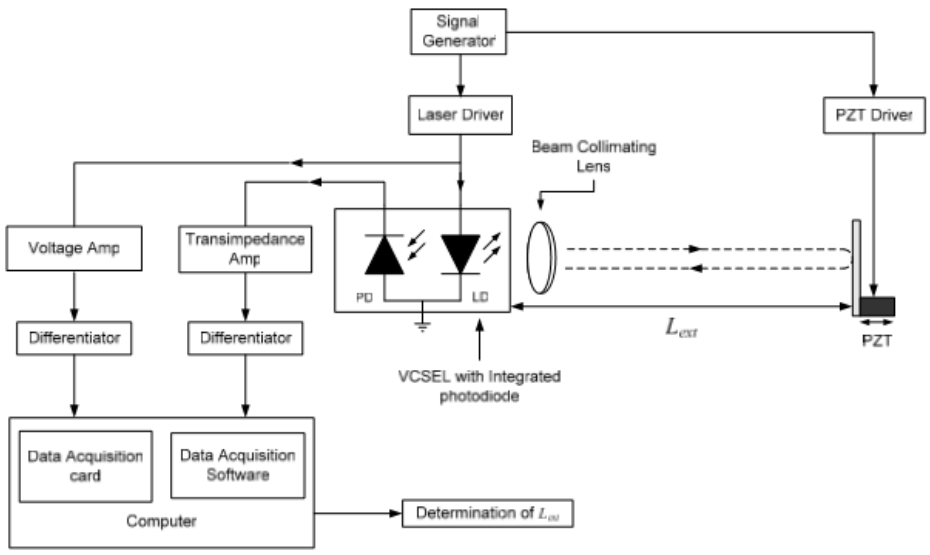

Figure 1.14: Block diagram of experimental result, signals from the photodetector and laser junction voltage are used to determine the distance between the laser and the target [6].

Surface-Emitting Laser (VCSEL) lasing at 850 nm was modulated with 0.1 mA current amplitude at 100 Hz frequency modulation in triangle waveform. The signal from both photodetector and laser junction voltage were obtained in this experiment as shown in Figure 1.14.

Further, both current and voltage signals were sent to the differentiator circuits, and an FFT algorithm was applied to produce a power spectrum array. From Figure 1.15, it was clear that both the current and the voltage waveform contain the same frequency

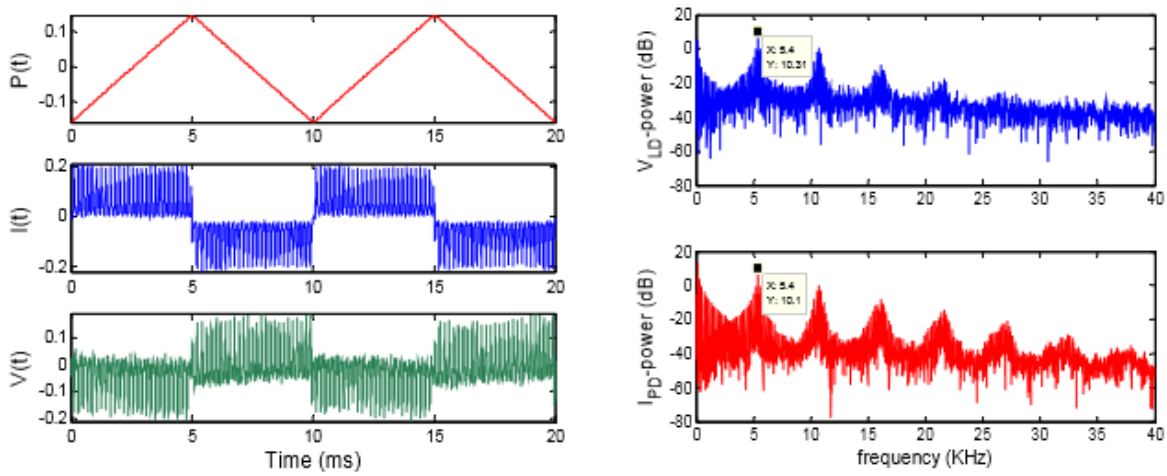

Figure 1.15: Experimental time-domain signal (a) and its frequency spectrum (b) at the target distance of 30 cm method [6].

component even though the result from the voltage waveform in the time domain was much noisier. The accuracy and precision from the two measurement systems were quite similar both in the time domain and frequency domain.

In 2006, Guo *et al.* demonstrated a new distance measurement technique based on the self-mixing effect by modulating the wavelength and the phase of the laser [7]. Wavelength modulation of the laser beam was obtained by modulating the injection current of the laser diode and phase modulation of the laser is obtained by an electro-optic crystal (EOC) in the external cavity as shown in Figure 1.16. The laser's wavelength was modulated with the current amplitude of 0.1 mA at 20 Hz of frequency modulation and the laser's phase was modulated with 1.2 rad at 2 kHz frequency modulation. Then the absolute distance of the external target was determined by Fourier analysis method. The experimental results showed that an accuracy of ± 0.3 mm could be achieved for an absolute distance of target ranging from 277 mm to 477 mm.

The distance measurement based on self-mixing was generally reported using a single-mode laser. In 2007, Tucker *et al.* demonstrated the effect of coexisting transverse modes on the measurement of the distance between the laser and the target [8]. They used two different VCSEL lasers: a single-mode VCSEL and a multi-mode VCSEL commercially lasing at 850 nm. Both lasers were operated with 4.5 mA of injection current where it resulted in different frequency modulation coefficients due to the transverse mode wavelengths without feedback, λ_{M}. To measure the distance between the laser and the target, both VSCELs were fixed to an optical rail and modulated in triangle waveform at 75 Hz

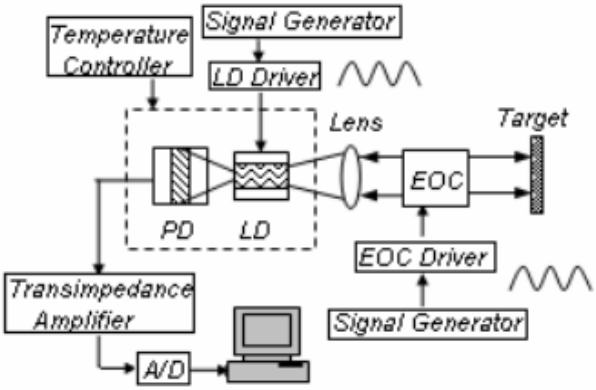

Figure 1.16: Experimental setup with double modulation−wavelength and phase [7].

of frequency modulation.

The single-mode VSCEL was modulated with a current sweep of 0.064 mA which corresponded to a frequency sweep of 8.42 GHz. The results from the single mode VCSEL shown in Figures 1.17(a) and (b) illustrate the time-domain with the external distance of 36.5 cm and 36.6 cm, respectively. In the same figure, the fast Fourier transform (FFT) were applied to both time-domain results to determine the beat frequencies. Clearly, there is no significant change in the amplitude of the time-domain waveform. However, the results shown in Figures 1.18(a) and (b) show the effect of multiple transverse modes with the multi-mode VCSEL laser that was modulated with a current sweep of 0.287 mA corresponding to a frequency sweep of 8.53 GHz. The same target distances as the single-mode VCSEL are used, and the results showed that the peak's amplitude in the time-domain waveform vary due to the different FM coefficients of the transverse modes by means of different wavelengths. Furthermore, the position of the maximum and minimum amplitudes for the peaks vary with the distance target.

Theoretically, the distance measurement resolution based on the self-mixing effect is limited with the conventional counting the number of interferometric fringes technique in the output power. The resolution can be improved by increasing the extent of the laser frequency modulation. However, continuous thermal wavelength tuning by injection current in Fabry-Pérot laser is typically limited to about 0.1 nm by longitudinal mode hopping and the attainable resolution cannot be better than a few millimetres for a single-shot measurement.

Furthermore, in practice, noises are presented, i.e., shot noise, where the measurement resolution is getting worse. In 2012, Norgia *et al.* published a paper where the resolution of the distance measurement was improved [9]. The injection current of the

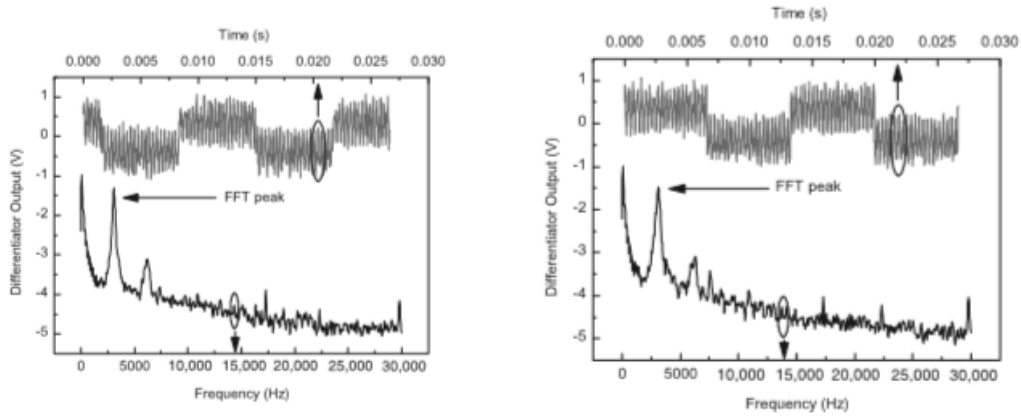

(a) (b)

Figure 1.17: Derivative of the total output power waveform (light) and FFT (dark) with the single-mode VCSEL at (a) 36.5 cm and (b) 36.6 cm [8].

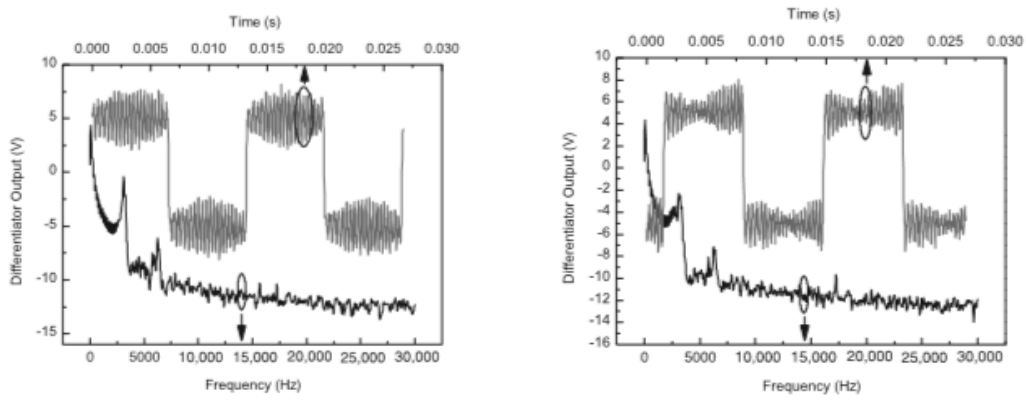

(a) (b)

Figure 1.18: Derivative of the total output power waveform (light) and FFT (dark) with the multi-mode VCSEL at (a) 36.5 cm and (b) 36.6 cm [8].

laser diode was modulated in a triangle waveform where it was reduced the duty cycle of the waveform about 10% (5% at the beginning and another 5% at the end of the triangle modulation waveform) as shown in Figure 1.19 .

In their experiment, they were strictly working when the feedback parameter $C < 1$. They explained that the accuracy of distance measurement strongly depends on the wavelength modulation coefficient. However, this parameter is not constant throughout the electrical frequency modulation which impacts the fringes beat frequency in the output power. In their experiment, they decided to work in the dashed circle shown in the Figure 1.20 which is ranging about 300 Hz to a few kHz. The measurement results were

Figure 1.19: The shape of laser current modulation [9].

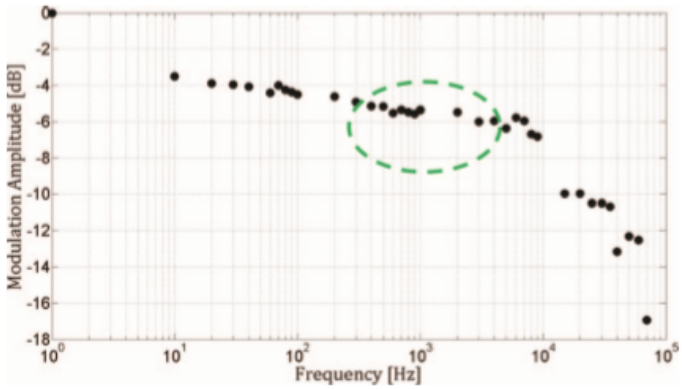

Figure 1.20: Experimental results of wavelength modulation coefficient in function of frequency modulation [9].

improved with resolution better than $100\,\mu\mathrm{m}$ for external distances up to 2 m.

The non-linearity in laser frequency under injected current tuning strongly affects the distance measurement resolution as shown by many researchers above. In 2014, Kou *et al.* demonstrated a method to linearise the laser emission frequency to attain higher measurement resolution [10]. The non-linearity between the laser emission frequency and the injection was demonstrated with the effect of temperature and carrier concentration. Figure 1.21 shows the effect of the non-linearity between the laser emission frequency and the injection current that results in non-constant of the beat frequencies.

Figures 1.22(a) and (b) represent the effect of current tuning on the spectral width of the beating signal. The proposed current reshaping method was proposed to improve the distance resolution to better than $20\,\mu\mathrm{m}$ over the range of 2.4−20.4 cm.

As described above about the absolute distance based on self-mixing technique, most experiments and results were obtained when the laser diode was operated in the weak regime by means of very low light re-injecting into the inner cavity of the laser diode.

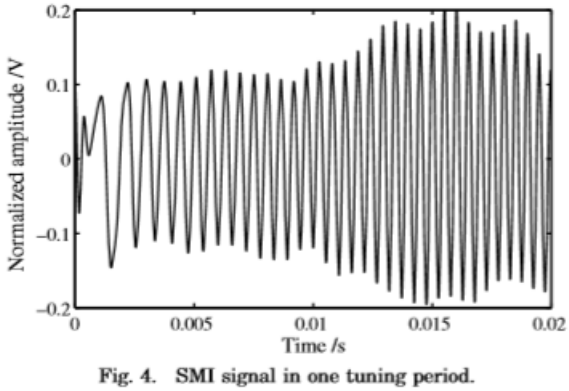

Figure 1.21: Experimental setup with double modulation−wavelength and phase [10].

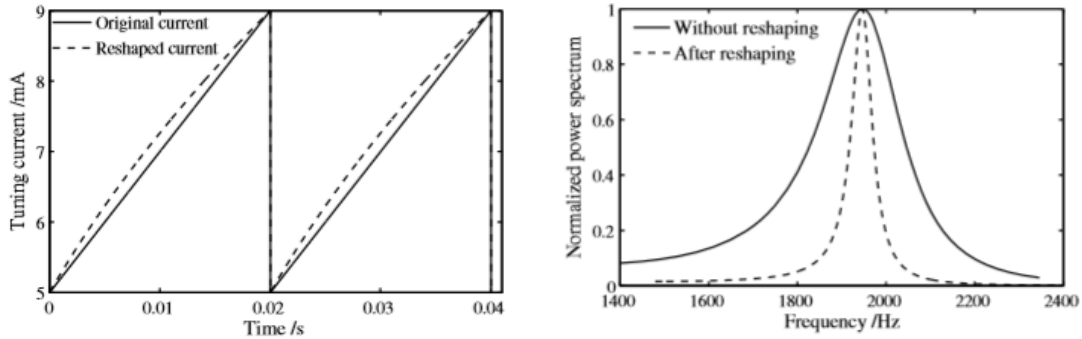

(a) (b)

Figure 1.22: (a) Power spectra of the beat signal with and without current reshaping.(b) Reshaped current versus original current [10].

However, when a high proportion of light from the external target backscatters into the laser cavity, the distance measurement has not been covered yet. The next chapter will describe the theory of the laser with external optical feedback first with the three-mirror cavity model in the quasi-static approximation then using the dynamic model derived from the rate equations. Both fundamental models can be used to characterise the self-mixing sensors in various sensing configurations but we show in the following chapters that some behaviour of the laser under feedback can only be taken into account using the dynamic model. The next chapter will also aim especially to provide an insight into the laser field phase behaviour under the weak and the moderate regimes, where the fringe disappearance occurs. The resolution of the excess phase equation based on the boundary method gives an explicit demonstration of this phenomenon and its dependency to the optical feedback level.

2

Modelling the Fringe Disappearance in a Self-Mixing Sensor

Two different approaches to modelling the SMI phenomenon have been developed: the three-mirror cavity [56] and the perturbation of the rate equation [49]. The 1980 work of Lang and Kobayashi presented the core model for a semiconductor laser experiencing optical feedback that captures the essence of laser dynamics under feedback [49]. This model has remained the foundation for phenomenological models of these systems to the present day and it is acknowledged to provide a realistic physical model. For sensing application purpose, the rate equation model is most often invoked and considering the frequency domain of these applications; the rate equations are simplified under the steady-state conditions. Such approximation can be made when the temporal changes in the stimulus are slow relative to the natural frequencies of the laser relaxation frequency and the natural resonant frequency of the external cavity [57]. The single equation that describes the phase condition imposed by the optical feedback is usually referred to as the excess phase equation and is applicable to single-mode lasers [58].

One of the most important and useful parameters in the excess phase equation is the feedback parameter C as it can be used to qualitatively categorise the regime of the laser under optical feedback [57, 59, 60, 61]. When the feedback level $C \leq 1$, the laser behaviour is stable. Most of the research publications have been reported when the laser diode under the optical feedback is operated in this regime. On the other hand, when the feedback level $C > 1$, more complex phenomena are observed such as hysteresis effect, presence of multiple emission frequencies (including the unstable frequencies [57]), apparent splitting of the emission line due to mode hopping [61], and interferometric fringe disappearance phenomenon [35].

A well-accepted approach in the community describes the regimes of the laser diode

under optical feedback, based on the number of excess phase's solutions or the value of feedback parameter C so that: weak feedback ($0.1 < C < 1$, only one solution), moderate feedback ($1 < C < 4.6$, up to three solutions) and strong feedback ($C > 4.6$, more than five solutions) [35, 36, 62, 63, 64, 65, 66]. The feedback parameter C is directly involved in the interferometric fringe disappearance phenomenon, and Bernal *et al.* [67] works have described that this phenomenon depends on the regimes described above, i.e., fringes start disappearing only in the strong feedback regime, while Yu *et al.* [68] demonstrated that the number of fringes is divided by 2 in region 2 ($7.8 < C < 14.0$), 3 in region 3 ($14.0 < C < 20.3$) and so on. Other publications proposed that two pairs of interferometric fringes for a complete period of modulation disappear when there is a variation of C by 2π [69, 70]. However, to the best of our knowledge, no accurate explanations or theories on the mechanism of this phenomenon have been published so far.

The literature mentioned above on interferometric fringe disappearance always treated the phenomenon based on the observation made for harmonic motion displacement applications. The core issue in this configuration is the unfeasibility to maintain a constant feedback level C over the target course due mostly to speckle or imperfect alignment. The fringe disappearance phenomenon in SMI measurement sensors will have a significant effect on SMI measurement sensors. As a result, the fringe counting methods will not always be accurate when the laser diode is operated in $C > 1$.

In this chapter, the theory of the semiconductor laser experiencing optical feedback and the theory describing how interferometric fringes disappear in the SMI sensor are presented.

2.1 | Three-mirror model

A vast majority of the theoretical modelling of SMI is based on the three-mirror model. In order to better understand this model, it should first be described by considering the operation of the laser diode itself with no optical feedback normally which is known as the free-running state single-mode laser diode.

A stand-alone laser diode can be modelled by a classic Fabry-Pérot cavity depicted in Figure 2.1, consisting of two mirrors, M_1 and M_2, with corresponding electric field amplitude reflection coefficients, r_1 and r_2, and an amplification medium with a refractive index, n_{in}, within the active cavity of length L_{in} [56]. The light emission is made in the form of an electromagnetic wave which is assumed to be a plane wave travelling from the mirror M_1 in the z-axis direction along the longitudinal dimension of the laser cavity

with $z = 0$ at the laser facet M_1 and to $z = L_{\text{in}}$ at the laser facet M_2.

The optical power will be amplified due to stimulated emission both in the forward direction (i.e., $P_{\text{f}}(z)$) and the backward direction ($P_{\text{b}}(z)$). The forward propagation optical power inside the laser cavity, $P_{\text{f}}(z)$ can be expressed as follows [56],

$$P_{\text{f}}(z) = P_{\text{f},0} \exp(gz - \alpha_{\text{s}} z), \tag{2.1}$$

where g is the material gain in stimulated emission, α_{s} is the coefficient representing the losses mainly due to absorption by the carrier within the laser cavity, as well as scattering losses. There are two main conditions to ensure the existence of a laser emission: the minimum gain which is related to the number of free carrier in the active area and the phase condition that determines the frequency to be emitted by the laser. The forward travelling complex electric field that propagates from $z = 0$ to $z = L_{\text{in}}$ is denoted as $E_{\text{f}}(z)$ with $P_{\text{f}}(z) \approx |E_{\text{f}}(z)|^2$ yielding,

$$E_{\text{f}}(z) = E_{\text{f},0} \exp(-j\beta z + \frac{1}{2}(g - \alpha_{\text{s}})z), \tag{2.2}$$

where β is the phase constant of the optical wave. The backward travelling wave amplitude, $E_{\text{b}}(z)$, after reflecting on the laser facet mirror M_2 can be determined in a similar fashion and it is expressed as,

$$E_{\text{b}}(z) = E_{\text{b},0} \exp(-j\beta(L_{\text{in}} - z) + \frac{1}{2}(g - \alpha_{\text{s}})(L_{\text{in}} - z)). \tag{2.3}$$

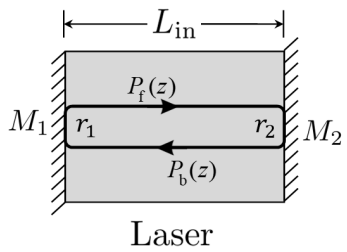

Figure 2.1: Schematic of two-mirror model of an optical cavity.

Furthermore, the amplitude reflection coefficient r_1 of the laser facet M_1 links the incident forward travelling wave $E_{\text{f}}(z = 0)$ and the reflected backward travelling wave $E_{\text{b}}(z = 0)$. It is also considered that the wave $E_{\text{f}}(z = L_{\text{in}})$ and $E_{\text{b}}(z = L_{\text{in}})$ are also linked to the amplitude reflection coefficient r_2 of the laser facet M_2 [35]. The relations are expressed as,

$$E_{\text{f}}(z = 0) = E_{\text{f},0} = r_1 E_{\text{b}}(z = 0) \quad \text{on interface } M_1, \tag{2.4}$$

$$E_{\mathrm{b}}(z = L_{\mathrm{in}}) = E_{\mathrm{b},0} = r_2 E_{\mathrm{f}}(z = L_{\mathrm{in}}) \quad \text{on interface } M_2. \tag{2.5}$$

From Eqs. (2.2) to (2.5), the stationary condition for the laser oscillation is written as,

$$r_1 r_2 \exp(-2j\beta L_{\mathrm{in}} + (g - \alpha_{\mathrm{s}})L_{\mathrm{in}}) = 1. \tag{2.6}$$

The absolute value of Eq. (2.6) yields a condition for the required gain g, while the phase yields a condition for the phase constant β. Solving this equation leads to express the threshold gain, $g_{\mathrm{th}} = g$, as,

$$g_{\mathrm{th}} = \alpha_{\mathrm{s}} + \frac{1}{L_{\mathrm{in}}} \ln(\frac{1}{r_1 r_2}). \tag{2.7}$$

With the multiple round-trips of the wave, a number of electric fields can propagate with the same amplitude. The total of the electric fields in the laser intracavity is equal to the superposition of each field in the cavity. The laser will have the maximum output power when all the fields in the cavity have the same amplitude. So the phase constant can be written as,

$$\beta L_{\mathrm{in}} = i\pi, \quad i = \text{integer}. \tag{2.8}$$

The phase constant β depends on the emission frequency ν_{th}. Then the effective refractive index inside the laser cavity for the lasing mode, n_{in}, can be introduced as [56],

$$n_{\mathrm{in}} = c\frac{\beta}{\omega_{\mathrm{th}}}, \tag{2.9}$$

where c is the speed of light in vacuum, and $\omega_{\mathrm{th}} = 2\pi\nu_{\mathrm{th}}$ is the angular frequency. Thus the possible emission frequencies ν_{th} are expressed as,

$$\nu_{\mathrm{th}} = \frac{ic}{2L_{\mathrm{in}} n_{\mathrm{in}}}. \tag{2.10}$$

By nature, a Fabry-Pérot laser has several frequencies of emissions and is called a multi-mode laser, however, modern laser diodes such as DFB, VCSEL and others introduce a Bragg selective filter in the cavity that selects a unique lasing frequency to be emitted. In this case, the laser is called single-mode and for simplicity purpose, the modelling od the self-mixing effect described below is done under the single-mode emission condition.

The two-mirror model is extended to the three-mirror model when the laser diode experience the optical feedback. The classical representation of the laser diode under the optical feedback is presented in Figure 2.2. Light leaves the internal cavity through the laser facet mirror M_2 and travels the external cavity of physical length L_{ext} with the effective refractive index n_{ext} to the surface of the target which is regarded as a third

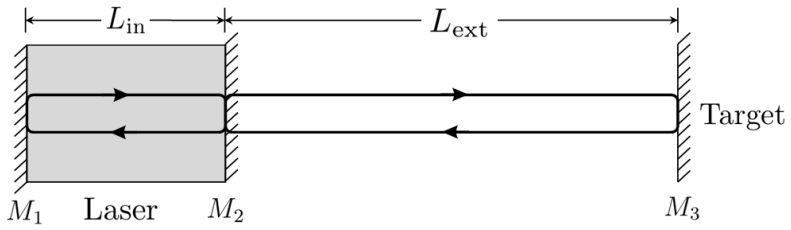

Figure 2.2: Schematic of the laser diode under optical feedback. Solid line with arrows indicates the beam light direction both in the internal and external cavity.

mirror M_3. The external round-trip propagation time is τ_{ext} and the ratio between the emitted light field amplitude and the re-injected light field amplitude r_{ext} [11, 35, 56].

The light at the mirror M_2 and the re-injected backscattered light from the external target is combined into a single term by considering the mirror M_2 and the target regarded as the third mirror as a single equivalent mirror with a new amplitude reflection coefficient, r_{eq}, and it is written as,

$$r_{\text{eq}}(\nu) = r_2 + \varepsilon(1 - |r_2|^2) r_{\text{ext}} \exp(-j2\pi\nu\tau_{\text{ext}}), \tag{2.11}$$

where ν represents the emission frequency of the laser with optical feedback, $|\varepsilon| \leq 1$ accounts for the reinjection factor which is not negligible since there are scattering and absorption losses of light through optical components and the diffraction loss of light due to a collimator lens usually put in front of the laser facet [11, 57] and τ_{ext} is the round-trip time of flight through the external cavity, and it can be expressed as [11],

$$\tau_{\text{ext}} = n_{\text{ext}} \frac{2L_{\text{ext}}}{c}. \tag{2.12}$$

The expression in (2.11) does not account for multiple reflections within the external cavity which is justified for $|r_2 r_{\text{ext}}| \ll 1$ including both the weak optical feedback $|r_{\text{ext}}| \ll |r_2|$ and the strong optical feedback $|r_{\text{ext}}| \gg |r_2|$ [56]. So the equivalent amplitude reflection can be rewritten as a single complex term,

$$r_{\text{eq}}(\nu) = |r_{\text{eq}}(\nu)| \exp(-j\varphi_{\text{r}}), \tag{2.13}$$

where $|r_{\text{eq}}(v)|$ is the amplitude of the equation and φ_{r} is the inverse of the phase of the equivalent amplitude reflection coefficient. Under the weak optical feedback, $\Re|r_{\text{eq}}(\nu)| \gg \Im|r_{\text{eq}}(\nu)|$ [71]; so that,

$$|r_{\text{eq}}(\nu)| = \Re|r_{\text{eq}}(\nu)| = r_2\Big[1 + \kappa_{\text{ext}} \cos(2\pi\nu\tau_{\text{ext}})\Big], \tag{2.14}$$

where

$$\varphi_{\mathrm{r}} = \kappa_{\mathrm{ext}} \sin(\omega \tau_{\mathrm{ext}}), \tag{2.15}$$

and

$$\kappa_{\mathrm{ext}} = \varepsilon \frac{r_{\mathrm{ext}}}{r_2}(1 - |r_2|^2). \tag{2.16}$$

κ_{ext} is the feedback coupling coefficient to the external cavity and is indicative of the quantity of light being coupled into the laser cavity.

The fluctuation in the reflectivity of the laser facet M_2 due to the external optical feedback leads to changes in the properties of the light emitted from the laser including the emission frequency, the linewidth, the threshold gain an consequently the output power. By considering that there is only a single longitudinal mode of operation, the amplitude condition for lasing with the equivalent mirror is,

$$r_1 |r_{\mathrm{eq}}| \exp\Big[(g - \alpha_{\mathrm{s}}) L_{\mathrm{in}}\Big] = 1. \tag{2.17}$$

The round-trip phase within the laser diode cavity have to be equal to an integer multiple of 2π yielding the phase condition,

$$2\beta L_{\mathrm{in}} + \varphi_{\mathrm{r}} = 2\pi m. \tag{2.18}$$

By using the effective refractive index n_{in} in Eq. (2.9) and the expression $\omega = 2\pi\nu$, then the expression in Eq. (2.18) can be re-written as,

$$\frac{4\pi\nu n_{\mathrm{in}} L_{\mathrm{in}}}{c} + \varphi_{\mathrm{r}} = 2\pi m. \tag{2.19}$$

Then the gain with the optical feedback, g_c, can be written as,

$$g_c = \alpha_{\mathrm{s}} + \frac{1}{L_{\mathrm{in}}} \ln\Big(\frac{1}{r_1 r_2 \big[1 + \kappa_{\mathrm{ext}} \cos(2\pi\nu\tau_{\mathrm{ext}})\big]}\Big). \tag{2.20}$$

The variation in the threshold gain under optical feedback, Δg, is

$$\Delta g = (g_c - g_{\mathrm{th}}) = -\frac{\kappa_{\mathrm{ext}}}{L_{\mathrm{in}}} \cos(2\pi\nu\tau_{\mathrm{ext}}). \tag{2.21}$$

Without optical feedback (the phase $\varphi_{\mathrm{r}} = 0$), the emission frequency $\nu = \nu_{\mathrm{th}}$ is obtained. Under the optical feedback, the emission frequency ν changes as well as the the threshold gain in Eq. (2.21), and thus the refractive index. Then, the total change of effective refractive index is [56],

$$\Delta(n_{\mathrm{in}}\nu) = \nu_{\mathrm{th}} \Delta n_{\mathrm{in}} + (\nu - \nu_{\mathrm{th}}) n_{\mathrm{in}}, \tag{2.22}$$

$$\Delta n_{\mathrm{in}} = \frac{\partial n_{\mathrm{in}}}{\partial N}(N - N_{\mathrm{th}}) + \frac{\partial n_{\mathrm{in}}}{\partial \nu}(\nu - \nu_{\mathrm{th}}). \tag{2.23}$$

where $\nu_{\rm th} = mc/2n_{\rm th}L_{\rm in}$ is the emission frequency at threshold of the laser, and $n_{\rm th}$ is the laser cavity effective refractive index at threshold. N and $N_{\rm th}$ are the carrier density and carrier density at threshold of the laser, respectively.

The variation of the effective refractive index with the carrier density is expressed as [56],

$$\frac{\partial n_{\rm in}}{\partial N}(N - N_{\rm th}) = -\frac{\alpha c}{4\pi\nu_{\rm th}}(g - g_{\rm th}), \tag{2.24}$$

where α represents the linewidth enhancement factor of the laser diode. It should be noticed that the value α depends on the type and laser materials, and the value was reported in the range from 3−7 for semiconductor laser, while this value is almost zero for other lasers [56]. By using the Eqs. (2.22)−(2.24), the variation of round-trip phase under optical feedback which is commonly known as the three-mirror model can be written as [56],

$$\Delta\varphi_{\rm c} = \frac{4\pi L_{\rm in}}{c}\Big[-\frac{\alpha c}{4\pi}(g - g_{\rm th}) + \nu_{\rm th}\frac{\partial n_{\rm in}}{\partial \nu}(\nu - \nu_{\rm th}) + n_{\rm in}(\nu - \nu_{\rm th})\Big] + \varphi_{\rm r}. \tag{2.25}$$

The relation between the effective refractive index and the emission frequency leads to define the effective group refractive index, $n_{\rm g}$, as [56],

$$n_{\rm g} = n_{\rm in} + \nu\frac{\partial n_{\rm in}}{\partial \nu}. \tag{2.26}$$

The expression of the three-mirror model can be rewritten as,

$$\Delta\varphi_{\rm c} = \frac{4\pi n_{\rm g} L_{\rm in}}{c}(\nu - \nu_{\rm th}) + \alpha(g - g_{\rm th})L_{\rm in} + \varphi_{\rm r}. \tag{2.27}$$

By linking the Eqs. (2.16), (2.21) and (2.27), the three-mirror model now reduces to,

$$\Delta\varphi_{\rm c} = \frac{4\pi n_{\rm g} L_{\rm in}}{c}(\nu - \nu_{\rm th}) + \kappa_{\rm ext}\Big[\sin(2\pi\nu\tau_{\rm ext}) + \alpha\cos(2\pi\nu\tau_{\rm ext})\Big]. \tag{2.28}$$

Introducing the round-trip delay of the solitary laser diode, $\tau_{\rm in}$, we get the three-model model expression as,

$$\Delta\varphi_{\rm c} = 2\pi\tau_{\rm in}(\nu - \nu_{\rm th}) + \kappa_{\rm ext}\sqrt{1+\alpha^2}\sin(2\pi\nu\tau_{\rm ext} + \arctan\alpha), \tag{2.29}$$

where

$$\tau_{\rm in} = n_{\rm g}\frac{2L_{\rm in}}{c}. \tag{2.30}$$

Considering that $\Delta\varphi_{\rm c} = 0$ for the compound cavity's frequency ν, by multiplying the factor of the external cavity round-trip time $\tau_{\rm ext}$ and the internal cavity round-trip time $\tau_{\rm in}$, and introducing the feedback parameter C which describes how effective optical

feedback changes the behaviour of the laser diode under optical feedback, the three-mirror model can be written as [56],

$$\Delta\varphi_{\mathrm{c}} = 2\pi\tau_{\mathrm{ext}}(\nu - \nu_{\mathrm{th}}) + C\sin(2\pi\nu\tau_{\mathrm{ext}} + \arctan\alpha), \tag{2.31}$$

where

$$C = \frac{\tau_{\mathrm{ext}}}{\tau_{\mathrm{in}}}\kappa_{\mathrm{ext}}\sqrt{1+\alpha^2}. \tag{2.32}$$

Every parameter is important for describing the characteristics of the laser diode under the optical feedback; however, one important and most useful parameter to figure out the characteristics is the feedback parameter C which is proportional to the reflectivity of the external mirror as well as the target distance (or external cavity length L_{ext}). To better understand the feedback parameter C, the three-mirror model in Eq. (2.32) is expressed to solve the possible optical frequencies by considering $\Delta\varphi_{\mathrm{c}} = 0$. The laser diode under optical feedback can be categorised into the following five regimes [11, 36, 56, 57, 72],

- Regime I: Very Small feedback or weak feedback ($C \leq 1$) with a single emission frequency and a broadening or narrowing of the linewidth of the laser oscillation depending on the phase of the feedback.
- Regime II: Moderate feedback ($C > 1$) which is caused to have multiple emission frequencies and instability, and mode hopping while the laser is still dependent on the phase of the feedback.
- Regime III: Strong feedback ($C \gg 1$) which results in a return to single emission frequency under feedback, and the laser diode is still dependent on the phase of the feedback.
- Regime IV: Chaotic regime where the relaxation oscillation becomes undamped, the laser linewidth is significantly broadened the laser evolves into unstable oscillations in a coherence collapse state. The level of noise is significantly enhanced under this condition, and the laser remains partially dependent on the phase of the feedback.
- Regime V: Return to stability where the internal and the external cavities behave like a single cavity and the laser oscillates in a single mode. The linewidth of the laser is extremely narrowed, and the laser is independent of the phase of the feedback.

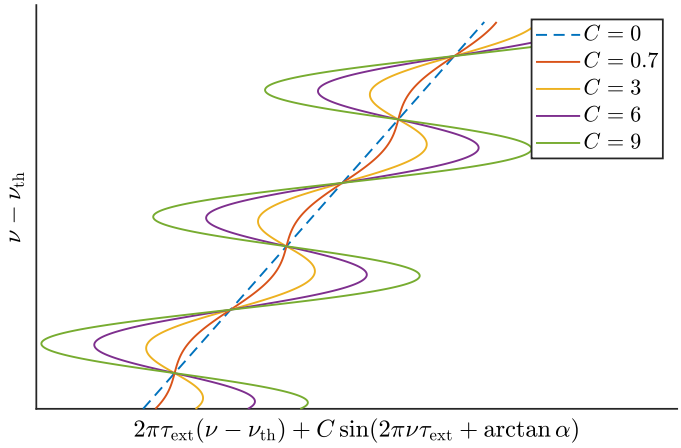

(a)

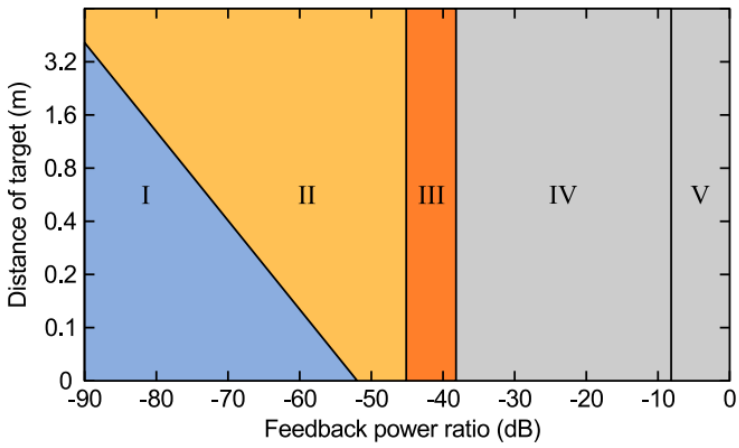

(b)

Figure 2.3: (a) Simulation of the three-mirror model versus change in emission frequency for different feedback levels. The dash line is the axis when the laser diode does not experience with the optical feedback. Unique solution can be found when the feedback parameter C is smaller than one while multiple solutions (both stable and unstable solution) can be found when the feedback parameter C is greater than one. (b) Operating regimes of LFI, after [11]. Region I, weak feedback; region II, moderate feedback; region III, strong feedback; region IV, chaos with islands of stability; region V, external cavity.

In this dissertation, We will limit our analysis of the phase behaviour of the laser under the weak and moderate/strong feedback regime as these regimes correspond to the realistic use of the phenomenon for sensing purposes.

2.2 | Dynamic model of laser under feedback

The dynamics of the laser under the optical feedback can be more accurately described with the derivation of the rate equation model. The dynamical model has the ability to perform the detail of the laser diode for small perturbation both stability and instability [57]. The laser diode under the optical feedback shows the unstable oscillations for a certain range of optical feedback level which means it is very interesting not only the viewpoint of fundamental physics but also for real-life applications since the optical feedback effects appear almost everywhere in optical systems such as optical communication systems, optical data storage and optical measurement. The rate equations for the laser diode under optical feedback can be explained by firstly considering the dynamic operation of the stand-alone laser.

There are two conventions to deal with the quantities of carriers and photons in the subsequent equations. One is using carrier and photon numbers, and another one is using carrier and photon densities. Here, we choose to develop the modelling using the carrier and photon densities, but we will express the complete set of equations for both conventions. It is interesting to notice that the phase condition for both conventions does not change.

To derive the rate equation of laser diode, we first considered the gain at the lasing condition which the same equation gives the round-trip gain within the laser cavity for the steady-state laser oscillation condition as [56],

$$G = r_1 r_2 \exp\Big(- 2j\beta L_{\mathrm{in}} + (g - \alpha_{\mathrm{s}}) L_{\mathrm{in}} \Big). \tag{2.33}$$

For dynamic operation of the laser, the emission frequency is a function of time. To simplify the following analysis, we assume that there is only a single longitudinal mode of operation, and the gain and loss coefficient are frequency independent parameters. The carrier density N deviates from the threshold carrier density value N_{th}. Under these conditions, the effective refractive index n_{in} can be linearised as [56],

$$n_{\mathrm{in}} = n_{\mathrm{th}} + \frac{\partial n_{\mathrm{in}}}{\partial \nu}(\nu - \nu_{\mathrm{th}}) + \frac{\partial n_{\mathrm{in}}}{\partial N}(N - N_{\mathrm{th}}), \tag{2.34}$$

where n_{th} is the effective refractive index at threshold. By replacing the expression of the optical frequency ν with the optical frequency at threshold ν_{th}, and using the Eq. (2.24), the relation between the laser oscillation frequency and the carrier density of laser can be written as,

$$\nu - \nu_{\mathrm{th}} = -\frac{\nu_{\mathrm{th}}}{n_{\mathrm{g}}} \frac{\partial n_{\mathrm{in}}}{\partial N}(N - N_{\mathrm{th}}). \tag{2.35}$$

The wave number β in Eq. (2.9) can be extended as,

$$\beta = \frac{\omega_{\mathrm{th}}}{c}\Big(n_{\mathrm{th}} + \frac{\partial n_{\mathrm{in}}}{\partial N}(N - N_{\mathrm{th}}) + \frac{n_{\mathrm{g}}}{\omega_{\mathrm{th}}}(\omega - \omega_{\mathrm{th}})\Big). \tag{2.36}$$

By replacing the wave number β into the Eq. (2.33), the gain can be rewritten as,

$$G = r_1 r_2 \exp\Big(-j\frac{2\omega_{\mathrm{th}}}{c}\Big[n_{\mathrm{th}} + \frac{\partial n_{\mathrm{in}}}{\partial N}(N - N_{\mathrm{th}}) + \frac{n_{\mathrm{g}}}{\omega_{\mathrm{th}}}(\omega - \omega_{\mathrm{th}})\Big]L_{\mathrm{in}} + (g - \alpha_{\mathrm{s}})L_{\mathrm{in}}\Big). \tag{2.37}$$

The gain G can be split up into two terms−the frequency independent term, G_1, and the frequency dependent term, G_2, where $G = G_1 G_2$ so that

$$G_1 = r_1 r_2 \exp(-j\frac{2\omega_{\mathrm{th}} L_{\mathrm{in}}}{c}\frac{\partial n_{\mathrm{in}}}{\partial N}(N - N_{\mathrm{th}}) + (g - \alpha_{\mathrm{s}})L_{\mathrm{in}}), \tag{2.38}$$

$$G_2 = \exp(-j\frac{2\omega_{\mathrm{th}} L_{\mathrm{in}} n_{\mathrm{in}}}{c} - j\frac{2\omega_{\mathrm{th}} L_{\mathrm{in}} n_{\mathrm{g}}}{c}(\omega - \omega_{\mathrm{th}})). \tag{2.39}$$

The frequency independent term G_1 can be separated into real and imaginary parts in the following forms,

$$G_1 = r_1 r_2 \exp((g - \alpha_{\mathrm{s}})L_{\mathrm{in}}) \exp(-j\varphi_{\mathrm{G}}), \tag{2.40}$$

where

$$\varphi_{\mathrm{G}} = \frac{2\omega_{\mathrm{th}} L_{\mathrm{in}}}{c}\frac{\partial n_{\mathrm{in}}}{\partial N}(N - N_{\mathrm{th}}). \tag{2.41}$$

The first term argument of exponential function of the frequency dependent term gain G_2 in Eq. (2.39) is related to the emission frequency for lasing in Eq. (2.10) at threshold which term $2\omega_{\mathrm{th}} L_{\mathrm{in}} n_{\mathrm{th}}/c$ must be equal to an integer multiple of 2π. The second term argument of exponential function can be reduced by using the internal round-trip propagation time expression τ_{in}. Then the term G_2 can be reduced to,

$$G_2 = \exp(-j\tau_{\mathrm{in}}\omega) \exp(j\tau_{\mathrm{in}}\omega_{\mathrm{th}}). \tag{2.42}$$

In order to analyse the field dynamics operation of the laser, the complex time-dependent electric field of the forward travelling wave at $z = 0$, $E_{\mathrm{f},0}(t)$, will be considered. Since the change in the emission frequency is small enough, the electric field essentially oscillates at the threshold, $\omega = \omega_{\mathrm{th}}$. This assumption is commonly known as the slowly-varying complex amplitude. This allows the change in the amplitude of the electric field to be easily describe by a slowly-varying complex amplitude $\hat{E}_{\mathrm{f},0}$ [56],

$$E_{\mathrm{f},0}(t) = \hat{E}_{\mathrm{f},0}(t) \exp(j\omega_{\mathrm{th}} t). \tag{2.43}$$

Then the electric field with a round-trip in the laser cavity can be expressed as,

$$E_{\mathrm{f},0}(t) = G_1 G_2 E_{\mathrm{f},0}(t) = G_1 \exp(j\omega_{\mathrm{th}}\tau_{\mathrm{in}}) \exp(-j\omega\tau_{\mathrm{in}}) E_{\mathrm{f},0}(t). \tag{2.44}$$

Since an exponential term contains a factor of frequency in the phase, it is equivalent to a time delay in the time domain: $d/dt = j\omega$. The exponential $\exp(-j\omega\tau_{\rm in})$ term then requires the time-shifting property of $\tau_{\rm in}$.

$$\hat{E}_{\rm f,0}(t)\exp(j\omega_{\rm th}t) = G_1\exp(j\omega_{\rm th}\tau_{\rm in})\hat{E}_{\rm f,0}(t-\tau_{\rm in})\exp(j\omega_{\rm th}(t-\tau_{\rm in})). \tag{2.45}$$

This leads to the conclusion that,

$$\hat{E}_{\rm f,0}(t) = G_1\hat{E}_{\rm f,0}(t-\tau_{\rm in}). \tag{2.46}$$

This equation tells us that the slowly-varying amplitude is equal to its original value at the start of the previous round-trip multiplied by the gain G_1. To express the rate of variation of the electric field amplitude, it is possible to describe the time-delayed function of the electric field in Eq. (2.46); so that,

$$\hat{E}_{\rm f,0}(t-\tau_{\rm in}) = \hat{E}_{\rm f,0}(t) - \tau_{\rm in}\frac{d\hat{E}_{\rm f,0}(t)}{dt}. \tag{2.47}$$

Then by using the expression $\hat{E}_{\rm f,0}(t-\tau_{\rm in}) = \hat{E}_{\rm f,0}(t)/G_1$ in Eq. (2.46), rate equation for the complex amplitude of the slowly-varying electric field is,

$$\frac{d\hat{E}_{\rm f,0}(t)}{dt} = \frac{1-1/G_1}{\tau_{\rm in}}\hat{E}_{\rm f,0}(t). \tag{2.48}$$

Since the frequency dependent gain G_1 is very close to unity for the laser oscillation, we approximate the gain from Eq. (2.40) as,

$$\begin{aligned}\frac{1}{G_1} &= \exp(\ln(\frac{1}{r_1r_2}) - (g-\alpha_{\rm s})L_{\rm in} + j\varphi_{\rm G})\\ &\approx 1 + \ln(\frac{1}{r_1r_2}) - (g-\alpha_{\rm s})L_{\rm in} + j\varphi_{\rm G}.\end{aligned} \tag{2.49}$$

By using the expression of the round-trip time of flight inside the laser cavity $\tau_{\rm in}$ and combining the expressions in Eqs. (2.35) with (2.41), the rate equation for the electric field in Eq (2.48) can be rewritten as,

$$\begin{aligned}\frac{d\hat{E}_{\rm f,0}(t)}{dt} &= \Big[j\frac{\varphi_G}{\tau_{\rm in}} + \frac{gL_{\rm in}}{\tau_{\rm in}} - \frac{\alpha_{\rm s}L_{\rm in} + \ln(1/r_1r_2)}{\tau_{\rm in}}\Big]\hat{E}_{\rm f,0}(t)\\ &= \Big[(\omega-\omega_{\rm th}) + \frac{1}{2}\Big(g\Big(\frac{c}{n_{\rm g}} - \frac{1}{\tau_{\rm ph}}\Big)\Big)\Big]\hat{E}_{\rm f,0}(t).\end{aligned} \tag{2.50}$$

where $\tau_{\rm ph}$ is the photon lifetime which is proportional to the threshold gain $g_{\rm th}$ and it is defined as [12],

$$\frac{1}{\tau_{\rm ph}} = \frac{c}{n_{\rm g}}\Big[\alpha_{\rm s} + \frac{1}{L_{\rm in}}\ln(\frac{1}{r_1r_2})\Big]. \tag{2.51}$$

In practice, the optical output power P is measured and is proportional to the square of the magnitude of the complex electric field such that $P \sim |E_{\mathrm{f},0}|^2$. Moreover, the optical output power is also proportional to the photon density inside the laser cavity S. Therefore, to model the rate of change in the laser output power, it is convenient to introduce a normalised complex field amplitude $E(t) = \sqrt{S(t)}\exp(j\varphi(t))$, where $\varphi(t)$ corresponds to the phase of the slowly varying amplitude of the forward travelling electric fields $\hat{E}_{\mathrm{f},0}(t)$, yielding instead of Eq. (2.48); so the absolute square of the magnitude of this field corresponds to the photon density S inside the laser cavity,

$$S(t) = E(t)E^*(t) = |E(t)|^2, \tag{2.52}$$

where * denotes as the conjugate complex value. Therefore, the rate equation for the electric field is,

$$\frac{dE(t)}{dt} = \Big[j(\omega - \omega_{\mathrm{th}}) + \frac{1}{2}\Big(g\frac{c}{n_{\mathrm{g}}} - \frac{1}{\tau_{\mathrm{ph}}}\Big)\Big]E(t). \tag{2.53}$$

The rate equation for the photon density can now be solved with the following relation,

$$\begin{aligned}\frac{dS(t)}{dt} &= \frac{d(E(t)E^*(t))}{dt} = E(t)\frac{dE^*(t)}{dt} + E^*(t)\frac{dE(t)}{dt} \\ &= \Big(g\frac{c}{n_{\mathrm{g}}} - \frac{1}{\tau_{\mathrm{ph}}}\Big)S(t).\end{aligned} \tag{2.54}$$

It should be noticed that the term $g = \Gamma g_{\mathrm{st}}$, where g_{st} is the stimulated gain coefficient, and Γ is the confinement factor which is a consequence of the photon and carrier population occupying different volumes such that $\Gamma = V/V_{\mathrm{P}}$ (V is the cavity volume and V_{P} is the effective cavity volume occupied by photons) [11, 56]. Due to the group velocity $v_{\mathrm{g}} = c/n_{\mathrm{g}}$, the general form gain G can be modified by linearising the logarithm of the stimulated gain coefficient, and it is expressed as [11],

$$G = v_{\mathrm{g}}g_{\mathrm{st}} = v_{\mathrm{g}}a(N - N_{\mathrm{tr}}), \tag{2.55}$$

where N_{tr} is the transparency carrier density in the laser cavity and a is the differential gain. Then the rate equation of photon density can be simply written as [11],

$$\frac{dS(t)}{dt} = \Big(\Gamma G - \frac{1}{\tau_{\mathrm{ph}}}\Big)S(t). \tag{2.56}$$

In order to obtain the rate equation for the phase, $\varphi(t)$, of the slowly varying envelope of the electric field, note that

$$\varphi(t) = \arctan\Big(\frac{\Im(E(t))}{\Re(E(t))}\Big). \tag{2.57}$$

Differentiating this equation, we obtain,

$$\frac{d\varphi(t)}{dt} = \frac{1}{[\Re(E(t))]^2 + [\Im(E(t))]^2} \times \Big[\Im\Big(\frac{dE(t)}{dt}\Big)\Re(E(t)) - \Re\Big(\frac{dE(t)}{dt}\Big)\Im(E(t))\Big] \quad (2.58)$$

It should be noticed that the two complex numbers$-x$ and y, the natural algorithm can be written as $\Im(x)\Re(y) - \Re(x)\Im(y) = \Im(y^*x)$ and using the Eq. (2.52), the rate equation of phase is obtained as [11],

$$\frac{d\varphi(t)}{dt} = \frac{1}{S(t)}\Big[\Im\Big(E^*(t)\frac{dE(t)}{dt}\Big)\Big] \quad (2.59)$$

Using the expression (2.53), the phase rate equation is then,

$$\begin{aligned}\frac{d\varphi(t)}{dt} &= \omega - \omega_{\mathrm{th}} \\ &= -\frac{\omega_{\mathrm{th}}}{n_{\mathrm{g}}}\frac{\partial n_{\mathrm{in}}}{\partial N}(N(t) - N_{\mathrm{th}}),\end{aligned} \quad (2.60)$$

By inserting Eq. (2.23) with the expression of the photon lifetime term in Eq. (2.51) and the gain term in Eq. (2.55), then the rate equation of phase in Eq. (2.60) is rewritten as,

$$\frac{d\varphi(t)}{dt} = \frac{1}{2}\alpha\Big(\Gamma G - \frac{1}{\tau_{\mathrm{ph}}}\Big), \quad (2.61)$$

To complete the description of the laser operation under dynamical operation, it is required the variation of the carrier density in the laser cavity. According to the Eqs. (2.56) and (2.61), the carrier density can be written as,

$$\frac{dN(t)}{dt} = \frac{\eta_{\mathrm{i}} I}{qV} - \frac{N(t)}{\tau_{\mathrm{n}}} - GS(t), \quad (2.62)$$

where η_{i} is the operation current injection efficiency, q is the electron charge, I is the operating current of the laser diode and τ_{n} represents the carrier lifetime.

The phase and amplitude condition for a laser diode with external reflections have been considered with the steady-state condition in Section 2.1. In this section, we will now turn to the dynamic condition of the laser diode under the optical feedback. In the steady state condition model for the laser under optical feedback, a complex reflection mirror, which is combined with the target mirror and the front mirror of laser facet, has been used. A similar analysis is also applied to the rate equations model for the optical feedback except that the time-dependent of the amplitude of the electric field is required.

The equivalent reflected coefficient of the three-mirror model in Eq. (2.13) remains the same in the rate equation except that the laser oscillates at the threshold frequency due to the slow-varying complex amplitude. The amplitude of the electric field that is

injected into the laser cavity at a time t is $E(t-\tau_{\text{ext}})$. To conclude this effect into the rate equation, the feedback term in the equivalent reflected coefficient is multiplied by $E(t-\tau_{\text{ext}})$ instead of $E(t)$. According to the Eq. (2.60), the rate equation with the optical feedback of the electric field is,

$$\frac{dE(t)}{dt} = \Big(j(\omega-\omega_{\text{th}}) + \frac{1}{2}(\Gamma G - \frac{1}{\tau_{\text{ph}}})\Big)E(t) + \frac{\kappa_{\text{ext}}}{\tau_{\text{in}}}E(t-\tau_{\text{ext}})\exp(-j\omega_{\text{th}}\tau_{\text{ext}}). \quad (2.63)$$

The modified rate equations for the laser under optical feedback for the photon density and the optical phase can be written by using the relations in Eqs. (2.54) and (2.61), and the rate equation of carrier density in Eq. (2.62) remains the same. So the rate equations in term of density with the optical feedback of laser diode can be described as,

$$\begin{cases} \dfrac{dS(t)}{dt} = \Big(\Gamma G - \dfrac{1}{\tau_{\text{ph}}}\Big)S(t) + \dfrac{2\kappa_{\text{ext}}}{\tau_{\text{in}}}\sqrt{S(t)S(t-\tau_{\text{ext}})}\cos\Big[\omega_{\text{th}}\tau_{\text{ext}} + \varphi(t) - \varphi(t-\tau_{\text{ext}})\Big] \\ \dfrac{d\varphi(t)}{dt} = \dfrac{1}{2}\Big(\Gamma G - \dfrac{1}{\tau_{\text{ph}}}\Big) - \dfrac{\kappa_{\text{ext}}}{\tau_{\text{in}}}\sqrt{S(t-\tau_{\text{ext}})/S(t)}\sin\Big[\omega_{\text{th}}\tau_{\text{ext}} + \varphi(t) - \varphi(t-\tau_{\text{ext}})\Big] \\ \dfrac{dN(t)}{dt} = \dfrac{\eta_{\text{i}}I}{qV} - \dfrac{N(t)}{\tau_{\text{n}}} - GS(t). \end{cases} \quad (2.64)$$

Eq. (2.64) is the standard set of rate equations expressed in terms of densities. To change the equations from density to number, the confinement factor must be used in this converting. So we use the term of $\widetilde{S}$ and $\widetilde{N}$ as photon number and carrier number respectively. The photon number is expressed as, $\widetilde{S} = V_{\text{P}}S$ and carrier number is described as $\widetilde{N} = VN$.

So the rate equations in term of number with the optical feedback of laser diode can be written as,

$$\begin{cases} \dfrac{d\widetilde{S}(t)}{dt} = \Big(\Gamma G - \dfrac{1}{\tau_{\text{ph}}}\Big)\widetilde{S}(t) + \dfrac{2\kappa_{\text{ext}}}{\tau_{\text{in}}}\sqrt{\widetilde{S}(t)\widetilde{S}(t-\tau_{\text{ext}})}\cos\Big[\omega_{\text{th}}\tau_{\text{ext}} + \varphi(t) - \varphi(t-\tau_{\text{ext}})\Big] \\ \dfrac{d\varphi(t)}{dt} = \dfrac{1}{2}\Big(\Gamma G - \dfrac{1}{\tau_{\text{ph}}}\Big) - \dfrac{\kappa_{\text{ext}}}{\tau_{\text{in}}}\sqrt{\widetilde{S}(t-\tau_{\text{ext}})/\widetilde{S}(t)}\sin\Big[\omega_{\text{th}}\tau_{\text{ext}} + \varphi(t) - \varphi(t-\tau_{\text{ext}})\Big] \\ \dfrac{d\widetilde{N}(t)}{dt} = \dfrac{\eta_{\text{i}}I}{q} - \dfrac{\widetilde{N}(t)}{\tau_{\text{n}}} - G\widetilde{S}(t) \end{cases} \quad (2.65)$$

As mentioned in Section 2.1, the SMI signal is observed by monitoring the fluctuations in either the laser output power (through the photodiode inside the package), or its terminal voltage. Linking optical output power variation to the rate equations model can be obtained as simple as noting that photon density is proportional to output optical power. By assuming that the rate of stimulated emission is approximately equal to the inverse of the photon lifetime above the threshold, and spontaneous emission is negligible,

then the total optical power emitted from both laser facets can be found as [11, 12],

$$P_{\mathrm{Total}}(t) = \hbar\omega v_{\mathrm{g}}\alpha_{\mathrm{m}}V_{\mathrm{P}}S(t) = \hbar\omega v_{\mathrm{g}}\frac{1}{2L_{\mathrm{in}}}\ln(\frac{1}{r_1 r_2})V_{\mathrm{P}}S(t), \tag{2.66}$$

where $\hbar$ is the reduced Plank's constant, and α_{m} is effective mirror loss which is proportional to the length of the laser cavity and the reflectivity coefficients of laser's two facets. The laser terminal voltage, V_{T}, can be determined by [73],

$$V_{\mathrm{T}}(t) = \frac{2k_{\mathrm{B}}T}{q}\ln(\frac{N(t)}{N_{\mathrm{i}}}), \tag{2.67}$$

where k_{B} is Boltzmann's constant and N_{i} represents the intrinsic carrier density of the active region.

The dynamic rate equation model for a laser diode with optical feedback can be investigated by numerically solving the above equation. In the rate equations model for a solitary laser diode, the phase does not affect the other variables, which means the laser diode is only described by photon density S and the carrier density N. However, it is not a suitable option for self-mixing, since the phase is proportional to other variables as shown in the equation above.

Under steady state condition, the rate equation can be reduced to excess phase equation. It occurs when the photon density S and the carrier density N change slowly and the frequency of system stimuli (in the form of changing current I, external cavity round-trip time τ_{ext}, or the coupling strength κ_{ext}) are slow relative to the natural frequencies of the system−the laser relaxation frequency and the natural resonant frequency of the external cavity. The steady-state solutions for $S(t) = S_{\mathrm{s}}, \varphi(t) = (\omega - \omega_{\mathrm{th}})t$, and $N(t) = N_{\mathrm{s}}$ from Eq. (2.64) can be written as [57, 74],

$$S_{\mathrm{s}} = \frac{\eta_{\mathrm{i}}I/qV - N_{\mathrm{s}}/\tau_{\mathrm{n}}}{v_{\mathrm{g}}a(N_{\mathrm{s}} - N_{\mathrm{tr}})}, \tag{2.68}$$

$$\omega - \omega_{\mathrm{th}} = \frac{1}{2}\alpha\Big(\Gamma G - \frac{1}{\tau_{\mathrm{ph}}}\Big) - \frac{\kappa_{\mathrm{ext}}}{\tau_{\mathrm{in}}}\sin(\omega\tau_{\mathrm{ext}}), \tag{2.69}$$

$$N_{\mathrm{s}} = N_{\mathrm{tr}} + \frac{1}{\Gamma v_{\mathrm{g}}a\tau_{\mathrm{ph}}} - \frac{2\kappa_{\mathrm{ext}}}{\Gamma v_{\mathrm{g}}a\tau_{\mathrm{in}}}\cos(\omega\tau_{\mathrm{ext}}). \tag{2.70}$$

Assuming the linear gain function in Eq. (2.55) and noting that, at threshold, the cavity gain is equal to material losses $1/\tau_{\mathrm{ph}}$, one obtains,

$$N_{\mathrm{s}} = N_{\mathrm{th}} - \frac{2\kappa_{\mathrm{ext}}}{\Gamma v_{\mathrm{g}}a\tau_{\mathrm{in}}}\cos(\omega\tau_{\mathrm{ext}}). \tag{2.71}$$

The photon density in Eq. (2.64) at the steady-state condition can be written as,

$$0 = \Big(\Gamma G - \frac{1}{\tau_{\mathrm{ph}}}\Big) + \frac{2\kappa_{\mathrm{ext}}}{\tau_{\mathrm{in}}}\cos(\omega\tau_{\mathrm{ext}}). \tag{2.72}$$

Combining the Eqs. (2.69) and (2.72) leads to,

$$\omega - \omega_{\mathrm{th}} = -\frac{\alpha\kappa_{\mathrm{ext}}}{\tau_{\mathrm{in}}}\cos(\omega\tau_{\mathrm{ext}}) - \frac{\kappa_{\mathrm{ext}}}{\tau_{\mathrm{in}}}\sin(\omega\tau_{\mathrm{ext}}). \tag{2.73}$$

The expression in Eq. (2.73) can be simplify by using the trigonometric formulas, $A\cos(\omega t)+B\sin(\omega t) = \sqrt{(A^2+B^2)}\cos(\omega-\arctan(B/A))$, $\arctan(1/\theta) = \pi/2-\arctan\theta$, and $\cos(\theta-\pi/2) = \sin\theta$, with the term of feedback parameter C in Eq. (2.32), then we obtain,

$$\varphi_{\mathrm{FB}} - \varphi_{\mathrm{s}} + C\sin(\varphi_{\mathrm{FB}} + \arctan\alpha) = 0, \tag{2.74}$$

where $\varphi_{\mathrm{FB}} \stackrel{\mathrm{def}}{=} \omega\tau_{\mathrm{ext}}$ represents a phase response, corresponding to the actual phase accumulated on transmission through the external cavity and $\varphi_{\mathrm{s}} \stackrel{\mathrm{def}}{=} \omega_{\mathrm{th}}\tau_{\mathrm{ext}}$ is a phase stimulus, corresponding to the phase accumulated on through the external cavity when the laser was not experiencing optical feedback [11]. In practice, the phase response φ_{FB} is not directly observable; so the observation of variation in laser power or variation in voltage across the laser terminal is experimentally performed. As we know that the optical power is proportional to the photon number and by considering the carrier rate equation in steady state (and a linear gain function), the optical power at steady state then can be found as [11],

$$P_{\mathrm{s}} \propto S_{\mathrm{s}} = \frac{1}{G}\Big(\frac{\eta_{\mathrm{i}}I}{qV} - \frac{N_{\mathrm{s}}}{\tau_{\mathrm{n}}}\Big). \tag{2.75}$$

By using the photon density and the carrier density at steady-state in the Eqs. (2.68) and (2.71) respectively, the optical power at steady-state can be rewritten as,

$$P_{\mathrm{s}} \propto \Big(\underbrace{\frac{\eta_{\mathrm{i}}I}{qV} - \frac{N_{\mathrm{th}}}{\tau_{\mathrm{in}}}}_{P_{\mathrm{s},1}} + \underbrace{\frac{2\kappa_{\mathrm{ext}}}{\Gamma v_{\mathrm{g}} a\tau_{\mathrm{in}}\tau_{\mathrm{n}}}\cos\varphi_{\mathrm{FB}}}_{P_{\mathrm{s},2}}\Big)\frac{\Gamma\tau_{\mathrm{ph}}}{1-2\kappa_{\mathrm{ext}}\tau_{\mathrm{ph}}\cos\varphi_{\mathrm{FB}}/\tau_{\mathrm{in}}}. \tag{2.76}$$

By considering that $2\kappa_{\mathrm{ext}}\tau_{\mathrm{ph}} \ll 1$, and noting that $(1-x)^{-}1 \approx (1+x)$ for $x \ll 1$, and normally the term $P_{\mathrm{s},1} \gg P_{\mathrm{s},2}$, the optical power then becomes,

$$P_{\mathrm{s}} \propto \Gamma\tau_{\mathrm{ph}}\Big(\frac{\eta_{\mathrm{i}}I}{qV} - \frac{N_{\mathrm{th}}}{\tau_{\mathrm{n}}}\Big)\Big(1 + \frac{\kappa_{\mathrm{ext}}\tau_{\mathrm{ph}}}{\tau_{\mathrm{in}}}\cos\varphi_{\mathrm{FB}}\Big). \tag{2.77}$$

This equation of the laser's power under the SMI phenomenon will then be used to plot figures in this thesis when using the excess phase equation by modifying the laser injection current if needed in any form of modulation.

2.3 | Phase condition

When the laser diode is operated under moderate/strong feedback regimes, the dynamics of the laser leads to several lasing solutions among which some are stable while others

are unstable [57]. The number of solutions of laser in the excess phase equation is defined by the value of the feedback parameter C in (2.31) and (2.74). An example of the evolution of the laser phase and its associated solutions for different values of the feedback parameter C is shown in Figure 2.3. For the sensing application, the external round-trip phase at the free-running state, also called the phase stimulus, changes over time either because of the modulation of the laser injection current or the change of the external round-trip propagation time (i.e., the variation of external cavity length or the fluctuation of the external refractive index).

2.3.1 | When $C \leq 1$

When the feedback parameter C is less or equal to one, the excess phase equation has a unique solution and it is dynamically stable. The relationship between phase stimulus and phase response is a simple monotonic function. The self-mixing laser is considered operating in weak feedback regime [57, 67].

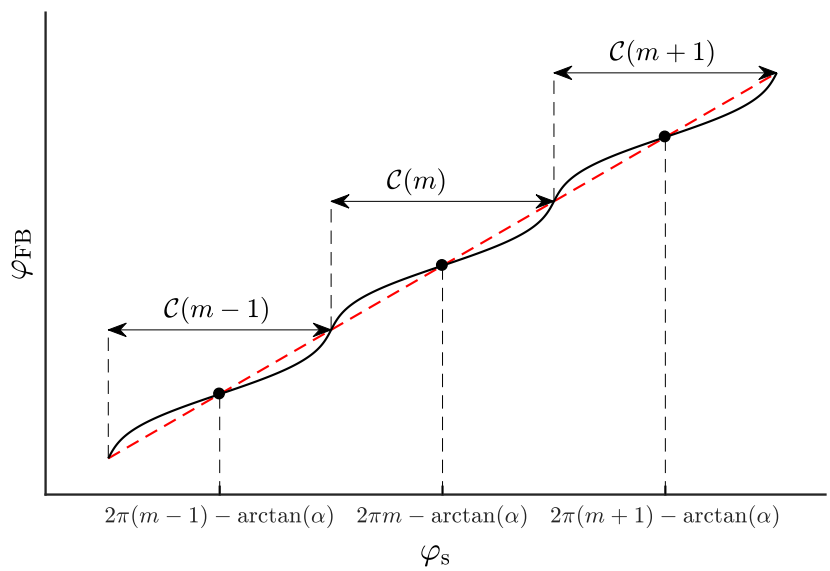

Figure 2.4: Plot of the excess phase equation for $C = 0.7$, and $\alpha = 5$. The red broken line is the axis where there is no optical feedback, and the black solid line indicates the solution path of φ_{FB}.

Figure 2.4 shows that the solution of the excess phase equation are segments of curves $\mathcal{C}(m-1), \mathcal{C}(m), \mathcal{C}(m+1)$ where m is an integer. Each segment is symmetrical to the point with coordinates $[\varphi_{\mathrm{s}} = 2\pi m - \arctan\alpha, \varphi_{\mathrm{FB}} = 2\pi m - \arctan\alpha]$ [75]. The solutions ex-

hibit path without any hysteresis effect which increases the phase φ_{FB} by 2π per segment of curve.

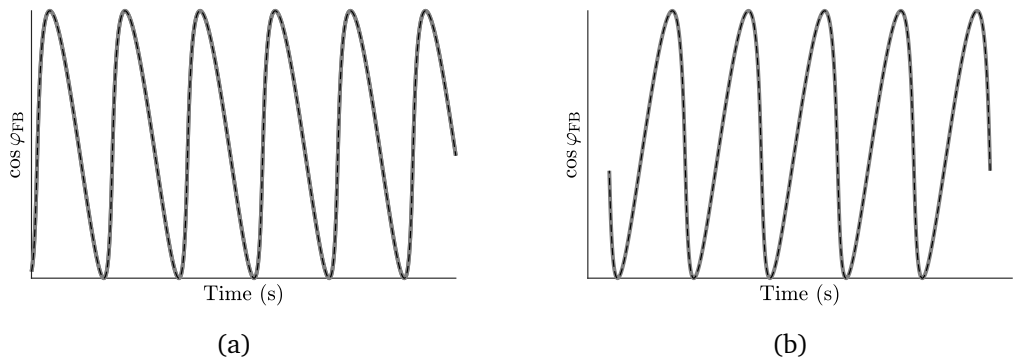

Figure 2.5: Plot the behaviour of $\cos\varphi_{\mathrm{FB}}$ under the feedback level $C = 0.7$. (a) In case of the phase stimulus decreases over time; (b) In case of the phase stimulus increases over time.

The orientation of the optical power function strongly depends on the shape of the phase response φ_{FB}. In the numerical simulation shown in Figure 2.5(a), it is assumed that the phase stimulus φ_{s} increases, i.e., the target is moving away from the laser. In contrary, if the phase stimulus φ_{s} decreases, the laser output power shows the reversed waveform which is shown in Figure 2.5(b). Therefore in case of SMI harmonic motion application, the direction of the target's moment can be determined from the shape of the waveform of the output power.

It is interesting to highlight that increasing the level of feedback C, the shape of the signal can be deformed from a sinusoidal for $C \ll 1$, to a non-symmetrical sinusoidal-like shape for $0.1 < C < 1$ as shown in Figure 2.5.

2.3.2 | When $C > 1$

When the feedback parameter C is greater than one, the laser under optical feedback is considered operating in moderate or strong feedback regime, multiple solutions can be found. The relation between φ_{FB} and φ_{s} becomes more complex but it is still maintaining the same symmetrical point for each curve.

Figure 2.6 shows the numerical simulation with the feedback parameter C is greater than one that the stable solutions of each curve indicated in the solid line region increases over the feedback level C. This phenomenon creates unstable solutions in the phase response and boundaries−high and low for each curve segment $\mathcal{C}$. Their boundaries of each curve segment $\mathcal{C}$ can be calculated as being zero of the first derivative of excess

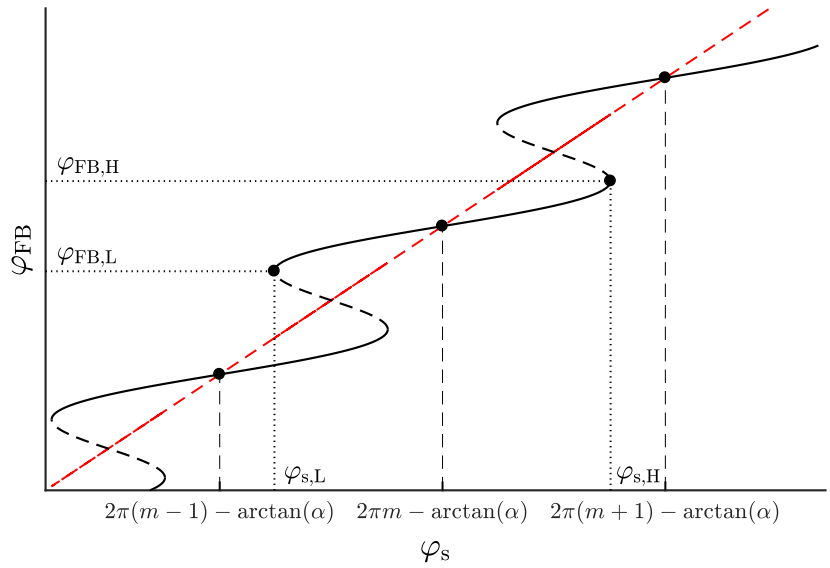

Figure 2.6: Plot of the excess phase equation for $C = 3$, and $\alpha = 5$. The red broken line is the axis where there is no optical feedback, and the black solid and broken lines indicate the region of stable and unstable solution of φ_{FB} respectively.

phase equation [57, 75],

$$\begin{aligned} 0 &= \frac{d}{d\varphi_{\mathrm{FB}}}[\varphi_{\mathrm{FB}} - \varphi_{\mathrm{s}} + C\sin(\varphi_{\mathrm{FB}} + \arctan\alpha)] \\ &= 1 + C\cos(\varphi_{\mathrm{FB}} + \arctan\alpha). \end{aligned} \tag{2.78}$$

By using the sign of the second derivative at the solution to identify the low and high boundary of the curve $\mathcal{C}(m)$ in the phase response, we get,

$$\varphi_{\mathrm{FB,L}} = (2m-1)\pi + \arccos(1/C) - \arctan\alpha \qquad \text{for the low boundary} \tag{2.79}$$

$$\varphi_{\mathrm{FB,H}} = (2m+1)\pi - \arccos(1/C) - \arctan\alpha \qquad \text{for the high boundary} \tag{2.80}$$

Then by inserting the phase response of Eq. (2.79) and Eq. (2.80) into the excess phase equation, the corresponding value of the phase stimulus can be found; and by using the trigonometric identity, $\sin(\arccos\alpha) = \sqrt{1-\alpha^2}$; we obtain,

$$\varphi_{\mathrm{s,L}} = (2m-1)\pi + \arccos(1/C) - \arctan\alpha - \sqrt{C^2-1}, \tag{2.81}$$

$$\varphi_{\mathrm{s,H}} = (2m+1)\pi - \arccos(1/C) - \arctan\alpha + \sqrt{C^2-1}. \tag{2.82}$$

Furthermore, the length of the stable solutions segments per segment of the curve $\mathcal{C}(m)$ varies with the feedback parameter C and it can be calculated as,

$$\varphi_{\mathrm{FB,H}} - \varphi_{\mathrm{FB,L}} = 2\pi - 2\arccos(1/C), \tag{2.83}$$

$$\varphi_{\mathrm{s,H}} - \varphi_{\mathrm{s,L}} = 2\pi - 2\arccos(1/C) + 2\sqrt{C^2 - 1}. \tag{2.84}$$

The expression (2.84) shows that the stable solution from the low to the high boundary of the phase stimulus is increasing with the feedback parameter C and is always greater than 2π. On the contrary, the stable solution of phase response in (2.83) gets smaller when the level of feedback C increases; and this phenomenon results in the discrepancy of the fringes amplitudes.

Figure 2.7 illustrates the laser phase behaviour in the case of a linear triangular modulation of the phase stimulus with an amplitude of 6π−from 2π to 8π (Figure 2.7(a)) when the parameter C is bigger than one. The solution to the excess phase equation and physical behaviour is then plotted in Figure 2.7(b).

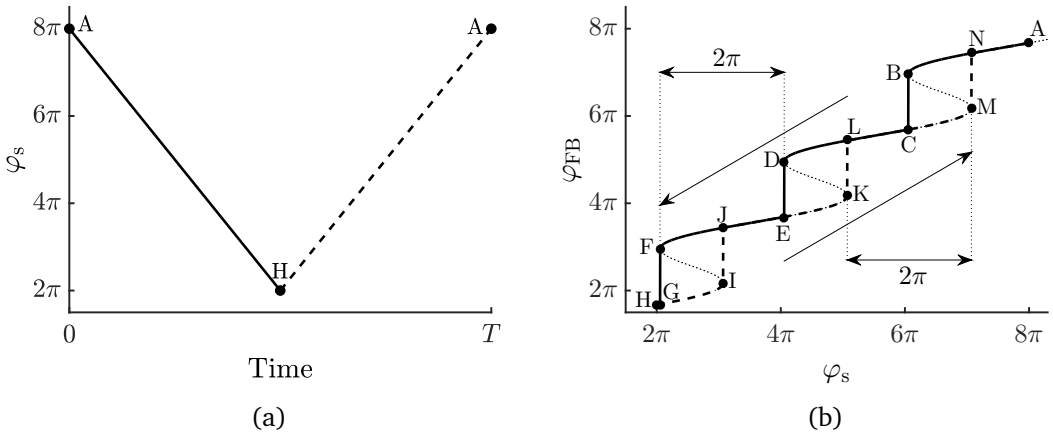

Figure 2.7: Plot (a) show the phase stimulus φ_s is modulated in triangle waveform with a period T and plot (b) is the resulting of phase response φ_{FB} with the change of φ_{s} from 8π to 2π, the feedback parameter $C = 3$, and $\alpha = 5$. The thin dotted lines shows the unstable solutions to the excess phase equation, the thick solid and dotted lines trace the locus of solution in plot (b) to the phase stimulus in plot (a).

The lasing phase starts dwelling solution from point A to B when the phase stimulus φ_{s} decreases, then jumps infallibly to the next closest solution in the vicinity of the other curve by means of point C and continues to D - E - F - G and H. At H, the minimum value of the phase stimulus ($\varphi_{\mathrm{s}} = 2\pi$) is reached. Then the phase stimulus φ_{s} increases for another half of ramp of modulation, the lasing phase dwells solution from point H to I, then jumps to in the vicinity of region J and continues with the path K - L - M - N and back to A at the maximum value of the phase stimulus ($\varphi_{\mathrm{s}} = 8\pi$). It is to be highlighted that from each jumping point to the low or high boundary the stimulus phase changes lengthen 2π.

2.3.3 | Fringes disappearance mechanism

The SMI phase behaviour described in the previous subsection is fundamental to explain the interferometric fringe disappearance phenomenon. The novelty of our approach to the fringe disappearance mechanism in SMI is that we use the phase boundary method. An interferometric fringe disappears whenever the low or high boundary of the stable solution exceeds the limit of the phase stimulus's minimum and maximum respectively. Figure 2.8 depicts the phenomenon in the case of a phase stimulus triangle modulation with the amplitude of 6π (same as for Figure 2.7). Figure 2.8(a) represents the phase's behaviour of the SMI under the optical feedback $C = 3$ which results in the derivative of optical output power in Figure 2.8(b). Under this feedback and as discussed the phase's dwelling in the previous section, there are no boundaries of stable solution that are reached within the idem of the phase stimulus. Then Figures 2.8(c) and 2.8(d) represent the phase paths and the derivative of output power for $C = 4.6$ whereas the lowest phase boundary would correspond to a phase stimulus that is the range of the actual stimulus thus leading to one missing fringe at each ramp (increasing decreasing) of the modulation. The phase paths and derivative of output power plotted in Figures 2.8(e) and 2.8(f) are computed for $C = 7.5$ where the highest phase boundary of the third stable region exceeds the maximum of the phase stimulus. An other fringe disappears at each ramp of the modulation leaving a single transition over the 6π of modulation. Eventually, for a parameter $C = 10$, no more phase transitions are within the range of the modulation and no interferometric fringes appear as shown in Figures 2.8(g) and 2.8(h).

It is to be highlighted that the absence of fringes is a consequence of a high feedback parameter C combined with a limited phase stimulus range (6π), as with an extended modulation range, fringes would have remained (for example, 12π modulation amplitude would have induced three fringes for the same $C = 10$ as shown in Figure 2.9). Thus the so-called strong optical feedback regime [36] is not literally a laser regime as it depends mostly on the stimulus modulation (i.e., the bias current modulation or the target displacement amplitudes).

2.3.4 | Feedback parameter C and fringe disappearance

The simulation shows that the low boundaries of the curve segments $\mathcal{C}$ at the left side always reach to the minimum of the phase stimulus as shown in Figure 2.9. In contrary, the high boundaries of the curve segments $\mathcal{C}$ at the right side always reach to the maximum of the phase stimulus. This can theoretically calculate the value of the feedback

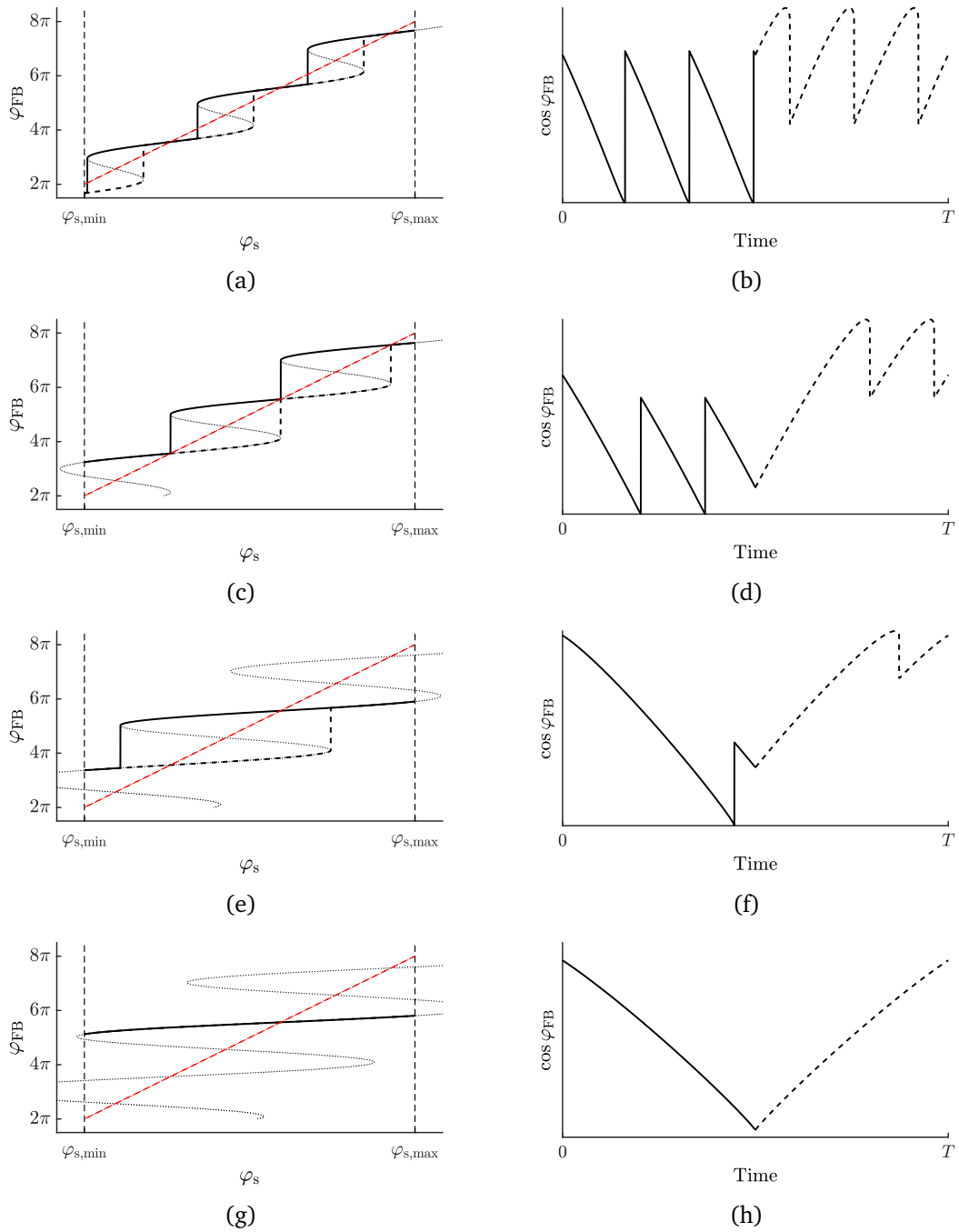

Figure 2.8: Numerical simulation with 6π phase stimulus's amplitude modulation. Plots (a), (c), (e), (g) are the phase behaviours under different feedback parameters C. Plots (b), (d), (f), and (h) are the results of derivative of output power under different feedback parameters C which correspond to (a), (c), (e), (g) respectively. (a) and (b) are plotted with $C = 3$; (c) and (d) are plotted with $C = 4.6$; (e) and (f) are plotted with $C = 7.5$; (g) and (h) are plotted with $C = 10$.

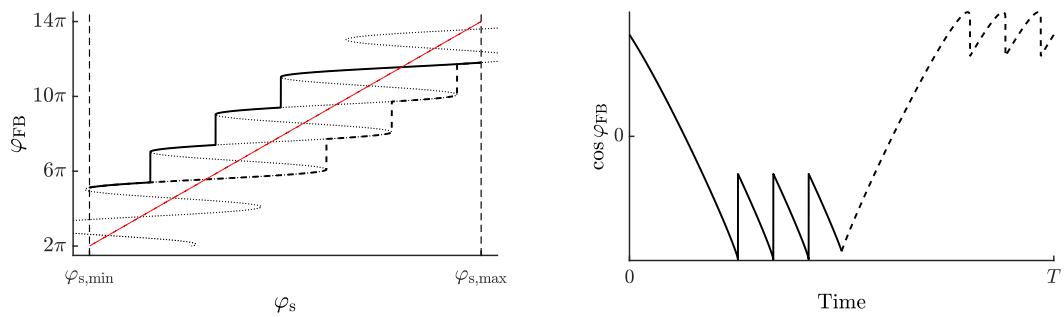

Figure 2.9: Numerical simulation with 12π phase stimulus's amplitude modulation. Plot (a) is the phase behaviour under different feedback parameters $C = 10$. Plot (b) is the result of derivative of output power which correspond to (a).

parameter C for which a fringe will disappear. For that, it is necessary to determine the integer number m that contains between 0 and $\varphi_{\mathrm{s}}(t)$ and this number satisfies the simple inequality as [75],

$$2\pi(m-1) - \arctan\alpha \leq \varphi_{\mathrm{s}} \leq 2\pi(m+1) - \arctan\alpha. \tag{2.85}$$

Then it gives,

$$m = \mathrm{round}\Big(\frac{\varphi_{\mathrm{s}} + \arctan\alpha}{2\pi}\Big). \tag{2.86}$$

The minimum and maximum number ($m_{\min}$ and $m_{\max}$) are determined by the value of the phase stimulus's minimum $\varphi_{\mathrm{s,min}}$ and maximum $\varphi_{\mathrm{s,max}}$, respectively. It is interesting to be highlighted that the number of interferometric fringes in the SMI system can also be found by subtraction the calculated maximum and minimum of integer ($m_{\max} - m_{\min}$). The pair of missing interferometric fringe occurs when either the low boundary or the high boundary exceeds the minimum or the maximum of the phase stimulus, respectively.

2.3.4.1 | The low boundary

After determining the integer number $m_{\min}$ from Eq. (2.86), let's consider that the low boundary of curve $\mathcal{C}(m_{\min})$ is for a given C value at the limit of the phase stimulus. The low boundary of the next curve $\mathcal{C}(m_{\min}+1)$ will reach the lower phase stimulus bound when,

$$\varphi_{\mathrm{s,L}}(m_{\min}+1) = \varphi_{\mathrm{s,min}}. \tag{2.87}$$

Using Eq. (2.81) with $m_{\min}+1$, then we get,

$$(2m_{\min}+1)\pi + \arccos(1/C) - \arctan\alpha - \sqrt{C^2-1} = \varphi_{\mathrm{s,min}}. \tag{2.88}$$

2.3.4.2 | The high boundary

THe same calculation is now done for the high boundaries of curves segment $\mathcal{C}$. Let's consider that for a given C value, the high boundary of the curve $\mathcal{C}(m_{\max})$ is just at the phase stimulus's bound; then the high boundary of the previous curve $\mathcal{C}(m_{\max}-1)$ will reach this bound when C increases so that,

$$\varphi_{\mathrm{s,H}}(m_{\max}-1)=\varphi_{\mathrm{s,max}}. \tag{2.89}$$

Using the high boundary of phase stimulus in Eq. (2.82) with $m_{\max}-1$, we obtain,

$$(2m_{\max}-1)\pi-\arccos(1/C)-\arctan\alpha+\sqrt{C^2-1}=\varphi_{\mathrm{s,max}}. \tag{2.90}$$

Numerical solving for the Eq. (2.88) and Eq. (2.90) can easily be found; so that the feedback parameter C where the first and second pair of interferometric fringes disappear in a complete period of modulation can be found. Since fringes are lost alternatively at the lower end and the higher end of the stimulus, the increment of ΔC of the feedback parameter C results in the loss of two interferometric fringe which can be written as,

$$\Delta C=C_{k+2}-C_k, \tag{2.91}$$

where k is whole number that indicates the number of disappeared pair of interferometric fringe. By considering that for a given feedback parameter C, the $m_{\min}+1$ stable solution limit (respectively $m_{\max}-1$) will be equal to the stimulus limit $\varphi_{\mathrm{s,L}}(m_{\min}+2, C+\Delta C)=\varphi_{\mathrm{s,min}}$ (respectively $\varphi_{\mathrm{s,H}}(m_{\max}-2, C+\Delta C)=\varphi_{\mathrm{s,min}}$) for a given feedback parameter $C+\Delta C$. Then we get,

$$\sqrt{(C+\Delta C)^2-1}-\arccos\frac{1}{(C+\Delta C)}=\sqrt{C^2-1}-\arccos\frac{1}{C}+2\pi. \tag{2.92}$$

Figure 2.10 shows the graphical solution of equation (2.92) where it can be observed that ΔC is a function of C evidentially reaching 2π for large C values.

By assuming that the two interferometric fringes disappear in increasing of the feedback parameter C in 2π, then the number of fringes disappearance gives the value of feedback parameter C in between two values and it can be expressed as,

$$(k-1)\pi+1\leq C\leq(k+1)\pi+1. \tag{2.93}$$

With the example of simulation result shown in Figure 2.8(f), two interferometric fringes have disappeared for semi-period of modulation at the derivative of output power; then we can estimate that this SMI system would be operated under the feedback level: $\pi+1\leq C\leq 3\pi+1$ ($4.14\leq C\leq 10.42$).

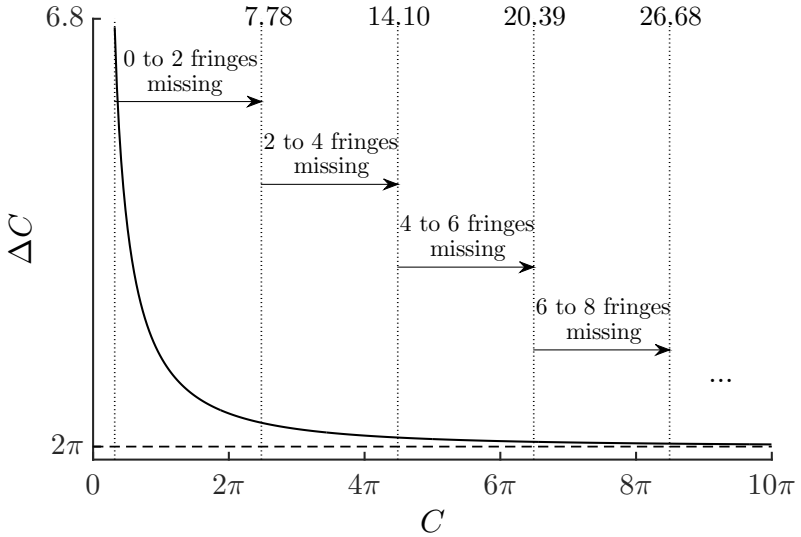

Figure 2.10: Evolution of the increment of C that results in the loss of two more fringes as a function of C and definition of the C ranges for which a pair of fringes have disappeared.

2.4 | Conclusion

The fringe disappearance phenomenon can be explained by the resolution of the excess phase equation considering the boundary method that has been exposed in this chapter. The main cause of the exceeding the low-high boundary of a curve $\mathcal{C}$ is due to the feedback parameter C. The parameter C is proportional to the coupling strength κ_{ext} varies mainly with the reflection coefficient of the target (the fraction of light coupled back into the lasing mode). The increase of the feedback parameter C in moderate/strong optical feedback regime exceeds the stable solution that can trespass the phase stimulus's boundary. The interferometric fringes are lost alternatively at the lower end and the higher end that results in space before a solid interferometric fringe appears in the optical output power. Then, in phase stimulus and phase response plane, each jumping point to the low or high boundary the stimulus phase by means the space between two interferometric fringes lengthen 2π. The number of missing interferometric fringes can be predicted by a proposed model, i.e., the value of feedback parameter C between 1 and 7.78, zero to two fringes are predicted to disappear in the output power. This interferometric fringe disappearance boundary method generated from the excess phase equation is also applied to the rate equations. However, it is interesting to know that the disappearance of interferometric fringe does not depend only with the feedback parameter C by means of

the coupling strength between the target and the laser cavity, but it is also known that it is proportional to the laser's structure and the photon lifetime. It means that the exactly defined parameter feedback C where an interferometric fringe disappears in the excess phase equation may not be applied in the rate equations (the photon lifetime and the carrier lifetime are proportional to carrier density and photon density, respectively). To validate this proposed model, an experiment of the self-mixing absolute distance application will be conducted in the next chapter. In addition, this experiment will demonstrate for the first time in SMI absolute distance measurement that interferometric fringes may disappear. Missing those fringes in the output power can strongly affect the measurement resolution.

3

Absolute Distance Measurement

This chapter discusses the use of self-mixing interferometry for metrology in absolute distance applications and the behaviour of the laser diode that performs in this application thoroughly. Distance measurement under the SMI technique is traditionally modelled with the three-mirror model by means of the excess phase equation. However, it can also be modelled with the rate equation based on Lang and Kobayashi equation which will present in section 3.1. Later, we also show the behaviour of the laser phase when it operated in the moderate/strong optical feedback regime in section 3.2 in both models. Finally, the experimental results will be conducted and validated with the describing theories proposed in Chapter 2.

3.1 | Modelling

Measuring based on the SMI technique, the emission frequency of the laser at free-running state diode needs to be modulated which is typically achieved by modulating the laser bias injection current with the triangle waveform [4]. With a fixed amplitude of current modulation at a certain frequency modulation, the SMI output power waveform monitored by the internal PD results in a triangle waveform with small ripples on the modulation ramp. Those small ripples correspond to the longitudinal modes in the external cavity whose numbers or time spacing between the ripples are proportional to the distance between the laser and the target [76]. The relationship between injection current and laser emission frequency at free-running state is generally considered as linear which is not entirely correct in practice. Thermal and plasma effects are presented when the injection current is modulated in any waveform and we will explain thoroughly about these effects in further sections. The laser emission frequency without the optical feedback, ν_{th}, varies with the laser emission frequency. To model this effect, the fre-

quency modulation coefficient, Ω, is introduced which indicates the linear relationship between the laser injection current and the laser emission frequency without the optical feedback is taken into account. This parameter is usually expressed in GHz/mA [76, 77], and the exact value depends on the type and materials of the laser diode itself and must be determined experimentally.

The variation in the laser emission frequency, $\triangle\nu_{\mathrm{th}}$, is related to the laser bias injection current, $\triangle I$,

$$\triangle\nu_{\mathrm{th}} = \Omega\triangle I. \tag{3.1}$$

Modulating the laser injection current of the active region results in a modulation of both the photon density and the carrier density which then modulates the laser gain. Thus, the rate equations are based on the slowly-varying envelope approximation (SVEA) where the change in laser emission frequency are written as a function of time. So, under the optical feedback, the laser emission frequency is not just functioned with time varying from the modulated bias injection current, $\nu_{\mathrm{th}}(t)$, but instead with time in presence of the feedback that is expressed in $\nu_{\mathrm{th}}(t-\tau_{\mathrm{ext}})$ term. Then the rate equations with optical feedback and laser emission frequency modulation are conventionally written in the form,

$$\begin{cases} \dfrac{dS(t)}{dt} = \Big(\Gamma G - \dfrac{1}{\tau_{\mathrm{ph}}}\Big)S(t) + \dfrac{2\kappa_{\mathrm{ext}}}{\tau_{\mathrm{in}}}\sqrt{S(t)S(t-\tau_{\mathrm{ext}})}\cos\varphi_{\mathrm{R}} \\ \dfrac{d\varphi(t)}{dt} = \dfrac{1}{2}\Big(\Gamma G - \dfrac{1}{\tau_{\mathrm{ph}}}\Big) - \dfrac{\kappa_{\mathrm{ext}}}{\tau_{\mathrm{in}}}\sqrt{S(t-\tau_{\mathrm{ext}})/S(t)}\sin\varphi_{\mathrm{R}} \\ \dfrac{dN(t)}{dt} = \dfrac{\eta_{\mathrm{i}}\big(I+\triangle I(t)\big)}{qV} - \dfrac{N(t)}{\tau_{\mathrm{n}}} - GS(t), \end{cases} \tag{3.2}$$

where

$$\varphi_{\mathrm{R}} = \omega_{\mathrm{th}}(t-\tau_{\mathrm{ext}})\tau_{\mathrm{ext}} + \varphi(t) - \varphi(t-\tau_{\mathrm{ext}}), \tag{3.3}$$

and

$$\omega_{\mathrm{th}}(t) = \omega_{\mathrm{th}} + 2\pi\triangle\nu_{\mathrm{th}}(t) \tag{3.4}$$

where $\omega_{\mathrm{th}} = 2\pi\nu_{\mathrm{th}}$ is angular lasing frequency in the absence of optical feedback at threshold.

A simulation of the rate equations for SMI absolute distance in this section is performed with the In-Plane laser parameters given in Table 3.1 and assuming that the In-plane laser diode is operated with an injection current of 60 mA and has -3 GHz/mA of frequency modulation coefficient [77], the laser modulation with 0.5 mA peak-to-peak amplitude at 50 Hz produces a SMI signal for the absolute distance that can be plotted. In this simulation, the fourth order Runge-Kutta numerical integration method is used to solve these rate equations [78]. For the initial condition, the values of the photon

Table 3.1: In-Plane laser parameters [12].

Symbol	Comment	Value
λ_{th}	Laser wavelength at threshold	$1550\,\mathrm{nm}$
r_1, r_2	Reflection coefficient of the laser mirrors M_1 and M_2	0.56
L_{in}	Laser cavity length	$250\,\mu\mathrm{m}$
α	Linewidth enhancement factor	3
n_{g}	Laser cavity group refractive index	4.2
n_{in}	Laser cavity (effective) refractive index	3.253
n_{th}	Laser cavity effective refractive index at threshold	3.16
a	Differential gain	$5.34 \times 10^{-16}\,\mathrm{cm}^2$
Γ	Optical confinement factor, $\Gamma = V/V_{rmp}$	0.032
α_{m}	Effective mirror loss	$45.6\,\mathrm{cm}^{-1}$
η_{i}	Current injection efficiency	0.9
τ_{ph}	Photon lifetime	$2.77\,\mathrm{ps}$
τ_{n}	Carrier lifetime	$2.71\,\mathrm{ns}$
V	Cavity volume	$4 \times 10^{-12}\,\mathrm{cm}^3$
V_{p}	Effective cavity volume occupied by photons	$1.25 \times 10^{-10}\,\mathrm{cm}^3$
N_{tr}	Carrier density in the laser cavity at transparency	$1.8 \times 10^{18}\,\mathrm{cm}^{-3}$

and carrier density in the absence of the optical feedback are first calculated without the presence of the feedback term by setting all the rate equations to zero. As we discussed before, the rate equations will give us a great detail of the complex behaviour of a laser experiencing optical feedback. Figure 3.1 shows the SMI output power under the feedback level $C = 0.7$ resulting from the numerical simulation.

Figure 3.1(a) shows the triangle-modulated laser injection. This variation of the driving current produces an assumed linear variation in the laser emission frequency as shown in Figure 3.1(b). In the presence of optical feedback under $C = 0.7$, the SMI output power results in the triangle waveform with a number of low-contrast ripples in each ramp of triangle modulation that is proportional to the external cavity length as shown in Figure 3.1(c). Then the small ripples output power can be made more distinct by derivating the output power waveform which then results in a series of sharp peaks as shown in Figure 3.1(d).

The classical method to calculate the distance between the laser and the target is by counting the integer number of observed interferometric fringes. Assuming that these

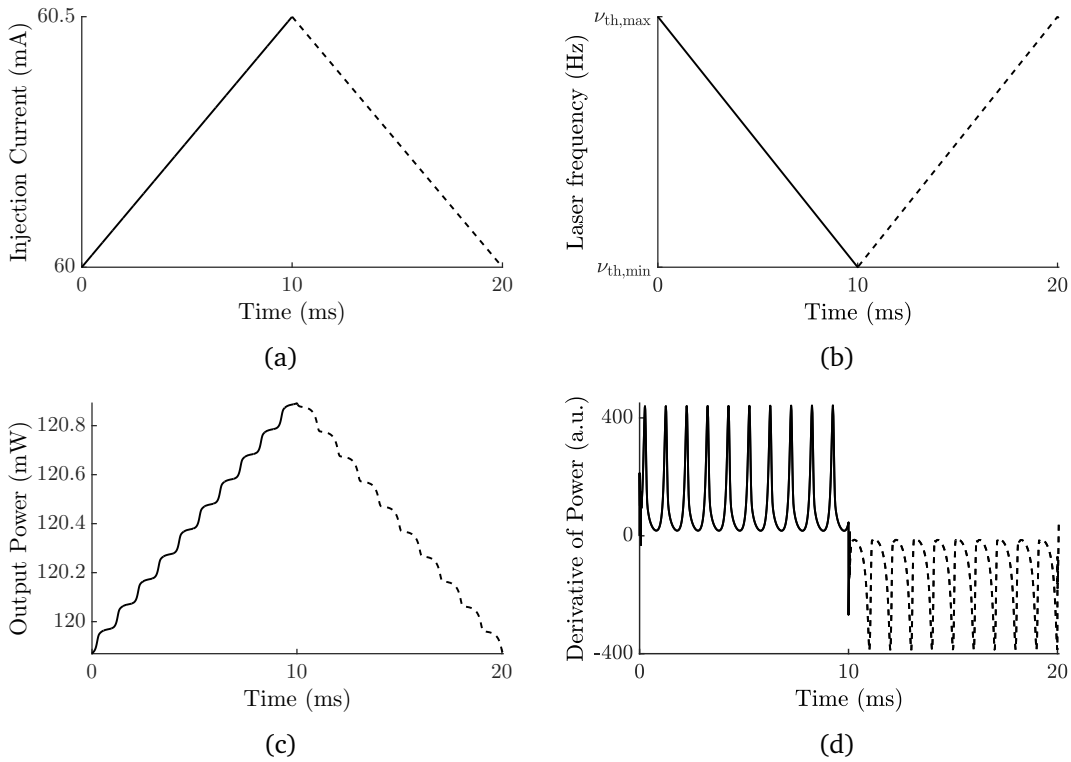

Figure 3.1: (a) Simulation of modulated injection current in triangle waveform varies from 60 mA to 60.5 mA at frequency modulation of 50 Hz−the increase and decrease ramp depicted in solid and broken line, respectively. (b) Simulation of laser emission frequency changes over time with the given FM coefficient $-3\,\mathrm{GHz/mA}$ and the amplitude of current modulation $0.5\,\mathrm{mA}$ peak-to-peak. (c) Simulation of optical output power of SMI signal with the small ripples in triangle waveform under the optical feedback $C = 0.7$ within the given parameter. (d) Simulation of the derivative of output optical power resulting from plot (c).

numbers for each half of the triangle waveform are $N_{\mathrm{f},1}$ and $N_{\mathrm{f},2}$, respectively, then the number of fringes recording during one complete period, T, is $N_{\mathrm{f}} = N_{\mathrm{f},1} + N_{\mathrm{f},2}$. So the external cavity of physical length can be calculated by [35],

$$L_{\mathrm{ext}} = \frac{cN_{\mathrm{f}}}{4\triangle I\Omega n_{\mathrm{ext}}}, \tag{3.5}$$

where n_{ext} is the refractive index of the medium in the external cavity. It is interesting to notice that the refractive index is dependent on temperature, pressure, humidity and CO_2 proportion [79, 80]. Automation of the counting fringes method is to set a threshold level where each peak with an amplitude over this level can be counted.

The other method that is considered more accurate to determine the distance is to calculate the average time between the fringes t_{avg}. This method can be done by first

counting the number of fringes and then divide it by the time between the first and the last fringe. The distance between the laser and the target can be finally calculated as [76],

$$L_{\text{ext}} = \frac{c}{4\triangle I\Omega n_{\text{ext}} f_{\text{m}} t_{\text{avg}}}. \tag{3.6}$$

There are numerous problems that arise when using this method in practice. In some cases, the heights of the fringes are not always constant where the signal is very noisy and thus requires a higher threshold and leads to the loss of some fringes in the counting. This phenomenon occurs in particular when increasing the distance, a high amplitude of current modulation causing the laser light dimmer at low current, poor reflectivity from the target and the transient response or thermal effect [76].

To counter this problem, an alternative algorithm has been described that uses the frequency domain. This method computes the average frequency of the fringes. The frequency is the inverse of the average time, t_{avg}, in Eq. (3.6) and the distance between the laser and the target can be determined by rearranging Eq. (3.6) to give,

$$L_{\text{ext}} = \frac{c f_{\text{b}}}{4\triangle I\Omega n_{\text{ext}} f_{\text{m}}}, \tag{3.7}$$

where f_{b} is the distant fringe frequency. The FFT method is usually considered as more robust than the spacing average time method for low signal levels and too noisy signal. On the other hand, it usually requires more computing resources. In the next section, we will discuss about the fringe disappearance phenomenon in SMI absolute distance.

3.2 | Fringe disappearance in absolute distance

The interferometric fringe phenomenon in the absolute distance application occurs when the feedback parameter C is greater than one by means of moderate/strong optical feedback regime. In this section, we will discuss the behaviour of laser under these regimes in the absolute distance application. An interferometric fringe will appear if there is a transition of the stable solutions between two curves $\mathcal{C}$ in the phase, and an interferometric fringe will disappear when the transition point of the curve $\mathcal{C}$ makes it to the boundary of phase stimulus by means of its minimum or maximum. We will discuss this behaviour with both models-the excess phase equation and the rate equations for SMI absolute distance application.

3.2.1 | Laser behaviour under the excess phase equation

The core of the excess phase equation is to solve the phase response φ_{FB}, and this parameter is inevitably depended on the phase stimulus φ_{s}, the feedback parameter C and the linewidth enhancement factor α. As we mentioned before, the linewidth enhancement factor α is usually modelled as a constant. So the phase response varies dependently only with the phase stimulus and the feedback parameter C. In the self-mixing absolute distance application, the laser injection current is modulated with a fixed peak-to-peak amplitude at a certain frequency modulation which then lengthens the phase stimulus with fixed boundaries which is written as,

$$\varphi_{\mathrm{s}}(t) = 2\pi\tau_{\mathrm{ext}}\left[\nu_{\mathrm{th}} + \triangle\nu_{\mathrm{th}}(t)\right], \tag{3.8}$$

By using the same simulation parameters in section 3.1, Figure 3.2 displays the behaviour of the laser phase and the derivative of output power resulting from the dwelling of the lasing mode in the phase.

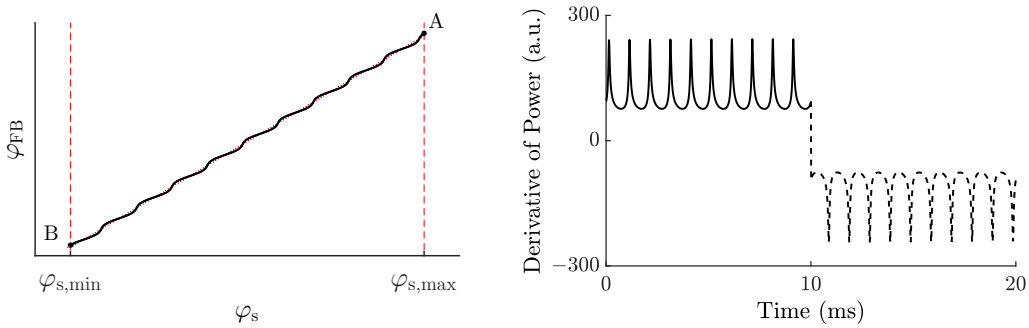

(a) (b)

Figure 3.2: The behaviour of the laser diode phase under weak optical feedback $C = 0.7$. (a) Plot phase response in function of phase stimulus. (b) Plot the derivative of output power resulting from the dwelling stable solution from (a).

The numerical simulation depicted in Figure 3.2(a) displays that the phase stimuli are composed of ten segments of the curve $\mathcal{C}$. Under the weak feedback regime, the lasing frequency does not show any anti-mode, so the lasing mode will dwell the stable solution in the phase stimuli without any mode hopping. The dwelling solutions of the lasing mode results in ten small ripples in the SMI output power which are then converted into the sharp peaks in the derivative of output power as shown in Figure 3.2(b). When the phase stimulus decreases over time for a semi-period of the triangle waveform indicated in solid line as shown in Figure 3.2(b), the lasing mode will delve the stable solution starting from the point A (the maximum of the phase stimulus $\varphi_{\mathrm{s,max}}$) to point B (the

minimum of the phase stimulus $\varphi_{\mathrm{s,min}}$) where the laser solution is no longer valid. At this point, the lasing mode will seek stable solutions from point B back to A in the way that the phase stimulus increases over time for another semi-period of the triangle waveform as indicated in broken lines. As a consequence, the derivative of output power displayed the same number of observed interferometric fringe between each half of the triangle waveform.

By using the Eq. (2.86) the integer number m of the curve $\mathcal{C}$ in the operation can be found. With the previous simulation, it gives $m_{\mathrm{min}} = 1289864$ and $m_{\mathrm{max}} = 1289764$ where it results in exactly ten interferometric fringes by subtracting its values. This result matches perfectly with the observed number of fringes in the derivative of output power. With these value of integer m, the value of the feedback C where the first and second interferometric fringe per semi-period of modulation can theoretically be found through the Eqs. (2.88) and (2.90). Numerical solution for these equations gives that the first and second pair fringes would be disappeared in the SMI output power when the feedback parameter C reaches to 2.20 and 6.97, respectively. By applying these values, C_1 and C_2, in the previous simulations, the laser phase behaviours and the SMI derivative of output powers can be re-plotted as shown in Figure 3.3.

With the feedback parameter $C = 2.20$, Figure 3.3(a) shows that the lasing frequency displays both the stable and unstable solution. As observed, the highest boundary extends to the maximum of phase stimulus which results in the disappearance a pair of interferometric fringes in the derivative of output power. The lasing mode starts delving the stable solution from point A ($\varphi_{\mathrm{s,max}}$) to B ($\varphi_{\mathrm{s,min}}$) with nine transitions as indicated in thick solid lines when the phase stimulus linearly decreases over time. Later, when the phase stimulus linearly increases for another half of the triangle waveform, the lasing mode seeks for the stable solutions from point B back to A in a different path with another nine transitions as indicated in the thick broken lines. This occurrence gives the change in shape and amplitude of the interferometric fringes at the output power as shown in Figure 3.3(b).

With further increasing value of the parameter feedback C to 6.97, another pair of interferometric fringes are missing in the derivative of output power. Figure 3.3(c) displays that the stable solutions of each curve are wider, and the lowest boundary enlarges to the minimum of phase stimulus. The dwelling of the lasing mode shows in a similar manner to the previous simulation with eight transitions of stable solutions that later results in eight interferometric fringes in the output power for each half of the triangle waveform as shown in Figure 3.3(d).

The next value of feedback parameter C (third and so on) where the interferometric fringes would be disappeared can be determined in a similar fashion. Once the feedback

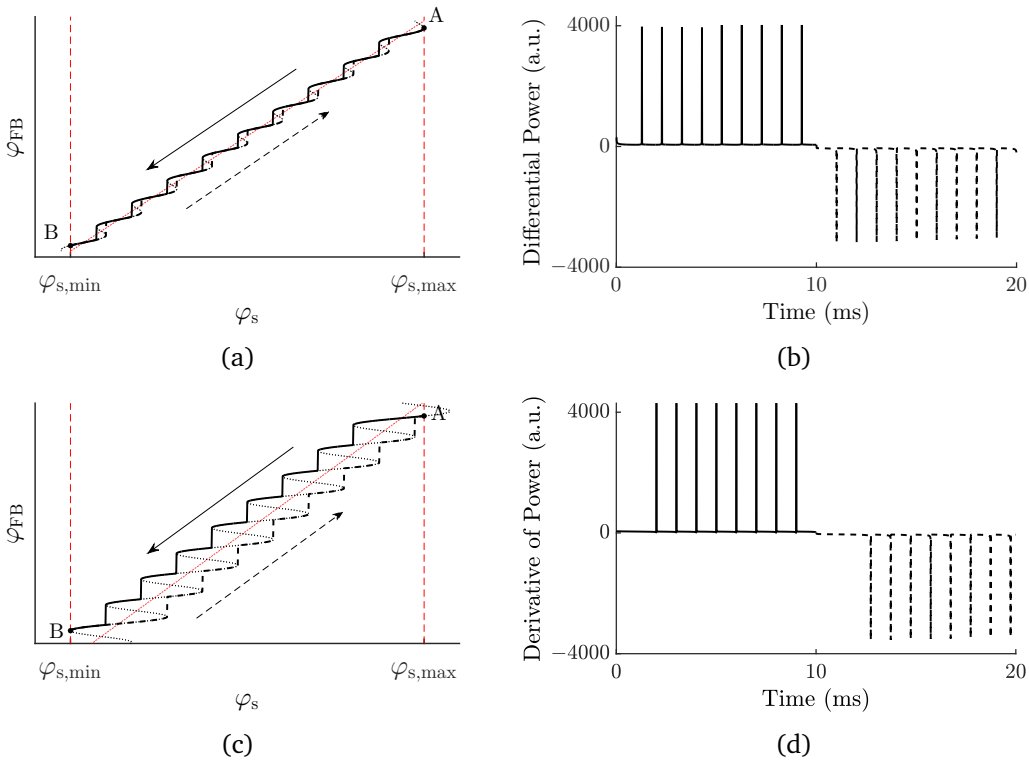

Figure 3.3: Simulation self-mixing absolute distance that the thick solid and broken lines indicate the direction of the phase stimulus during the decreasing and increasing respectively. (a) Plot of phase response φ_{FB} in function of phase stimulus φ_{s} under the optical feedback $C = 2.20$. (b) Plot of derivative of output power in the result from the dwelling phase in (a). (c) Plot of phase response φ_{FB} in function of phase stimulus φ_{s} under the optical feedback $C = 6.97$. (d) Plot of derivative of output power in the result of from the dwelling phase in (c).

parameter C equals to 32.16, the lasing mode will dwell on the stable solution back and forth on the same single curve by means of no more transitions of the stable solutions. So, the output power will result in no interferometric fringe and the distance calculation cannot be produced.

3.2.2 | Laser behaviour under the rate equations

In the section 3.2.1, we have seen that the first two pair of interferometric fringes will disappear when the feedback parameter C equals to 2.20 and 6.97, respectively. With the simulation parameters in Figure 3.1, the output power results in ten fringes for each half of the triangle waveform under the weak feedback regime. When the laser is in moderate/strong feedback regimes, the observed number of interferometric fringes in the

output power is different between the first modulation ramp and the others. Figure 3.4 depicts the situation when the laser diode first experiences the current modulation under the moderate/strong feedback regimes. The lasing mode does not follow the stable solution from point A as described in the previous section, but it starts from the starting point S. It should be noticed that both points A and S are at the same coordinate of the phase stimulus. So from point S, the lasing mode will seek stable solutions to point B with ten transitions when the phase stimulus linear decreases for the semi-period of modulation indicated in thick solid lines. Then, the lasing mode will follow the stable solution from point B with the linear increasing portion of the phase stimulus. However, the stable solution at the starting point S is never reached and the point A will be the maximum phase stimuli after only nine transitions will occur as indicated in the thick broken lines. For the following modulation cycles, the lasing mode will follow the stable frequency solution from point A back and forth between A and B. As a result, ten fringes shall be observed for the first half of the triangle waveform and nine fringes for the following modulation ramps as seen in Figure 3.4(b).

In a similar fashion, with a feedback C equals to 6.97, Figure 3.5(a) shows that the lasing mode will start from the starting point S to B and back to A for the first triangle waveform indicated in thick solid and broken lines, respectively, which then results in nine and eight fringes in the first modulation cycle output power. Later, for the following modulation cycle, the lasing mode will navigate back and forth between A and B resulting in eight fringes in each half of the triangle waveform as seen in Figure 3.5(b).

For the moderate values of the factor C simulated in Figures 3.4 and 3.5, the first half of the triangle waveform results in one more fringe to the number of fringes in the next following modulation ramps. However, the number of excess fringes in the first modulation ramp does vary with the coupling factor C. As discussed in the previous section, when the feedback parameter C increases to a larger value, no more interferometric fringes appear in the laser power. For example, with a value of feedback level $C = 32.16$, the computation of rate equations shown in Figure 3.6 essentially results in five observed fringes in the first half of the triangle waveform while no fringe appears in the following modulation ramps as shall be expected from the description in the previous simulations.

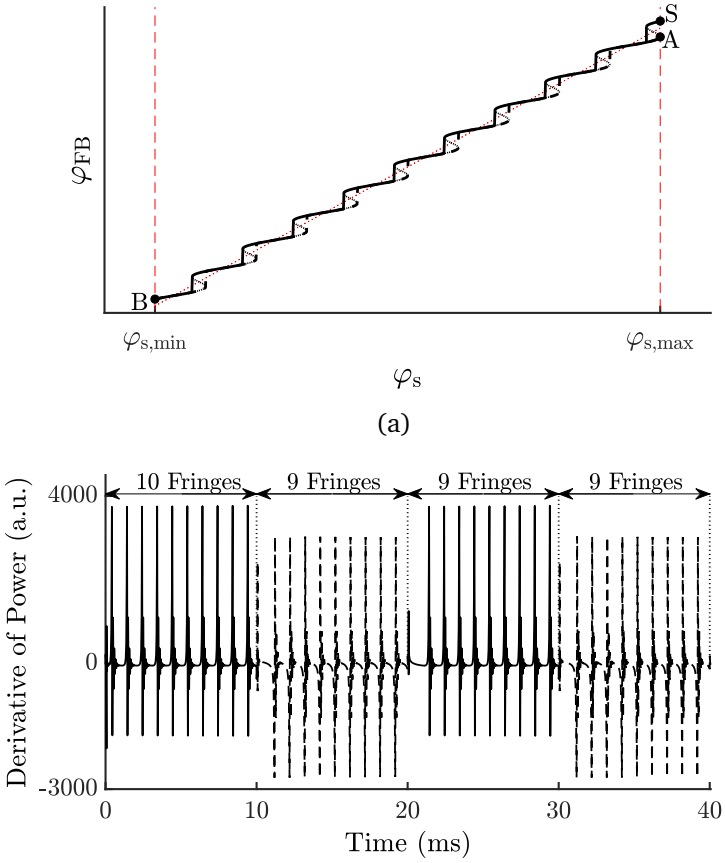

Figure 3.4: Simulation of output power from the rate equations under feedback parameter $C = 2.20$. (a) Plot of the phase response φ_{FB} in function of the phase stimulus φ_s; the thick solid and broken lines indicate the direction of the phase stimulus during decreasing and increasing respectively. (b) Plot of derivative of output power resulting from the evolution of the phase in (a).

3.3 | Experiments

3.3.1 | Feedback power ratio profile

The feedback parameter C in the excess phase equation or the coupling coefficient in the rate equation has proven to have a major effect on the self-mixing sensors signal shape and amplitude as well as the measurement resolution and the stability of laser diode. The variation of the feedback parameter C mainly depends on the external reflection coefficient of the fraction of light coupled back in the laser cavity. In practice, the coupling coefficient does not only depend on the target surface but also the external length of the

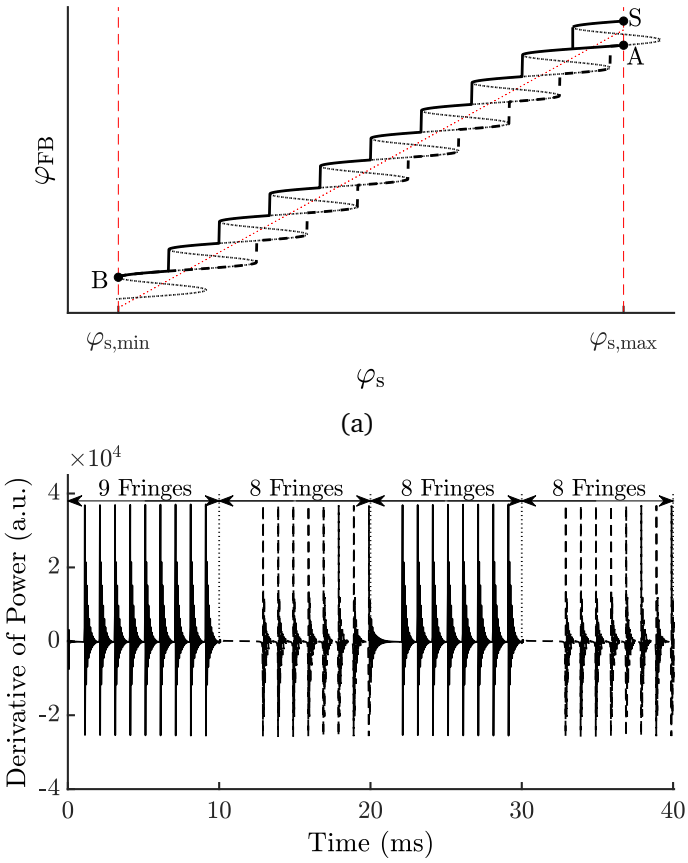

Figure 3.5: Simulation of output power from the rate equations under feedback parameter $C = 6.97$. (a) Plot of the phase response φ_{FB} in function of the phase stimulus φ_s; the thick solid and broken lines indicate the direction of the phase stimulus during decreasing and increasing respectively. (b) Plot of derivative of output power resulting from the evolution of the phase in (a).

target L_{ext}. Therefore, an experiment of the variations in the target surface's reflectivity and the external cavity length is accomplished.

The experimental setup is displayed in Figure 3.7. It consists of a DFB laser diode (L1550P5DFB) lasing at 1550 nm with a package including a monitoring photodiode that is associated to a collimating lens which focuses the laser beam onto the target surface. A 50/50 beam splitter is used to split the incident light beam from the laser−half goes to a tilt mirror to avoid the reflected light back to the beam splitter, and another half traverses the distance target to the target's surface. Then the beam splitter collects the 50% of the reflected light from the traget in the front-end detector of a power-meter

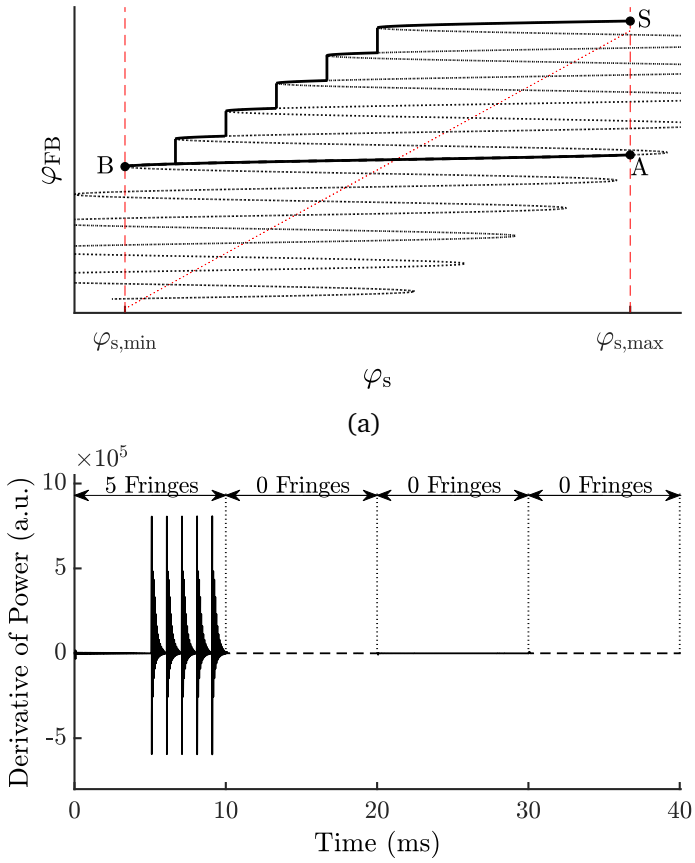

Figure 3.6: Simulation of output power from the rate equations under feedback parameter $C = 32.16$. (a) Plot of the phase response φ_{FB} in function of the phase stimulus φ_s; the thick solid and broken lines indicate the direction of the phase stimulus during decreasing and increasing respectively. (b) Plot of derivative of output power resulting from the evolution of the phase in (a).

through a collimating lens with the same model and it is installed with the same distance as the one located in front of the laser diode. The different target surfaces used for this experiment are a white paper, flat metal, microprismatic reflective tape and microsphere reflective tape. Each of the surfaces is installed on a long range translation stage. Thus, the laser beam is always pointing on the same area of the target surface. The feedback power ratios profile are measured with distances ranging from 20 cm to 1.5 m. The laser diode is operated with 17.5 mA injection current about 3 times its threshold current. Then the target power reflectivity R_{ext} can be calculated as,

$$R_{ext} = \frac{P_{FB}}{2P_0}, \tag{3.9}$$

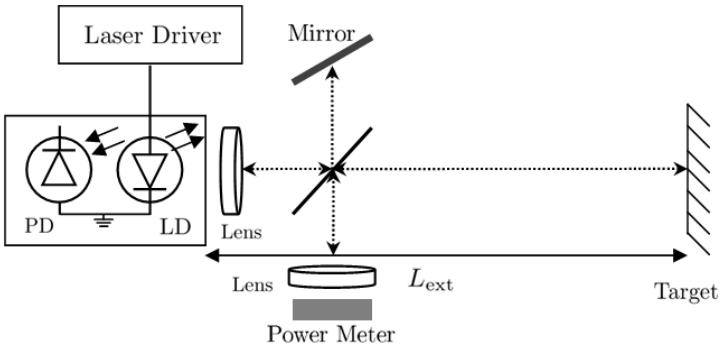

Figure 3.7: Experimental setup for measuring the target surface's reflectivity.

where P_0 is the half of unperturbed emitted power from the laser diode through the beam splitter and P_{FB} represents the half reflected power from the target. Then the amplitude reflection coefficient can easily be found as,

$$r_{\text{ext}} = \sqrt{R_{\text{ext}}}. \tag{3.10}$$

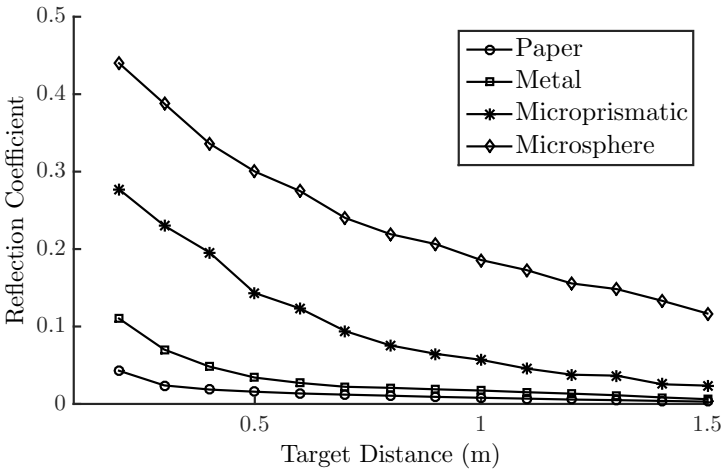

Figure 3.8: Amplitude reflectivity coefficient for different surface−white paper, flat metal, microprismatic reflective tape, and microsphere reflective tape.

Different target surfaces at the same distance from the laser result in different amplitude reflectivities as shown in Figure 3.8. Furthermore, when the distance between the laser and the target increases, the amplitude reflectivity of the target decreases. However, it does not mean that the feedback parameter C also decreases over the distance in the same way as the amplitude reflection coefficient. The feedback parameter C is also proportional to the external round-trip propagation time that is related to the external cavity

length as seen in Eq. (2.32). Assuming that the laser diode in this experiment is driven with the parameters of Table 3.1, with the constant of the loss re-injection factor of 0.1, and the half of the amplitude reflection coefficient (due to the 50/50 beam splitter−half goes back and re-injects into the laser cavity and other half goes to the power-meter), the expression of the feedback parameter C in Eq. (2.32) gives the results of each target surface.

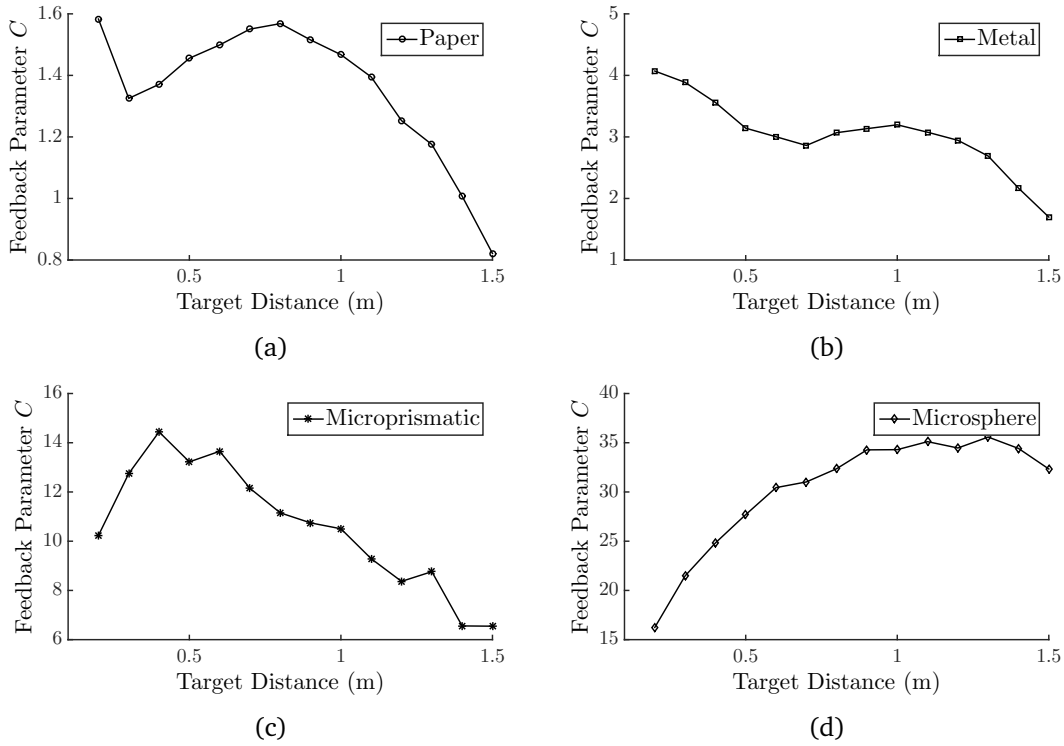

Figure 3.9: Variation of feedback parameter C as a function of the external cavity L_{ext} with different target's surfaces. (a) White paper. (b) Metal. (c) Microprismatic reflective tape. (d) Microsphere reflective tape.

It should be highlighted that different spots on the same surface and external cavity length may result in different amplitude reflection coefficient due to the speckle effect. Moreover, it is interesting to notice that the external amplitude reflection coefficient from the target is also changed due to the optical components i.e., the collimating lens used in front of the laser facet.

3.3.2 | Frequency modulation coefficient

The parameter known as FM coefficient symbolises the variation between the laser injection current and the emission frequency, it needs to be determined experimentally as it depends on the type, material, structure of the laser diode and the process of fabrication.

In this experiment, the FM coefficient is determined through the expression (3.6) by counting the number of fringes for a given external cavity length L_{ext}. To determine is set the value of this parameter more precisely, the laser diode under the optical feedback should be in the weak regime with the target surface covered by white paper located at the distance of 1.2 m from the laser facet that ensures a high number of interferometric fringes. The laser is biased with an injection current of 20 mA (around 3.34 times its threshold current of 6 mA) and modulated with a 8 mA peak-to-peak amplitude in triangle waveform. The photodetected signal from the photodiode is then converted to a voltage by a transimpedance amplifier with a gain of 40 dB and a selective bandwidth ranging from 40 Hz to 300 kHz.

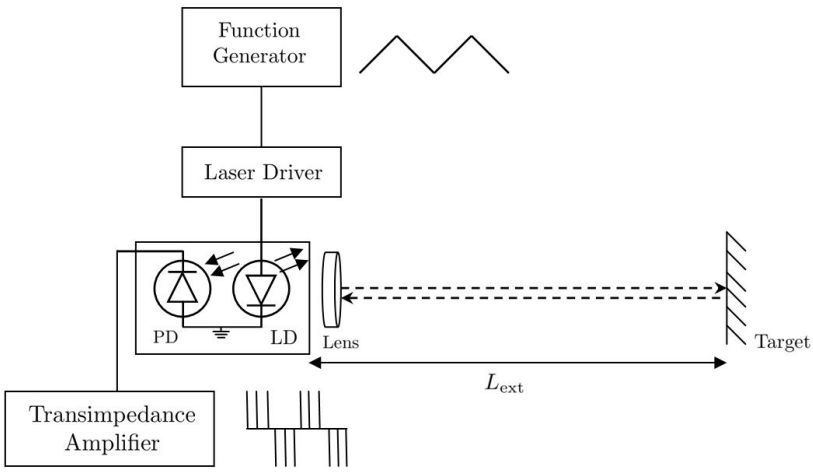

Figure 3.10: Block Diagram of experimental setup: laser and photodetector are in the same package; the laser bias injection current is modulated in triangle waveform from the function generator, and the target is a white paper located at 1.2 m from the laser facet.

The FM coefficient measurements are done for different modulation frequency ranging from 100 mHz to 1 kHz in order to determine its dependency to the frequency of the modulation signal. Figure 3.11 shows the results of SMI signal with different modulation frequency−100 mHz and 1 kHz. To determine the FM coefficient, the observed fringes in the SMI signal are counted. The number is then divided by the time between the first

and the last detected fringes. This has to be done two times for a full cycle of the triangle waveform-increase and decrease ramp. The computed FM coefficients are plotted in Figure 3.12.

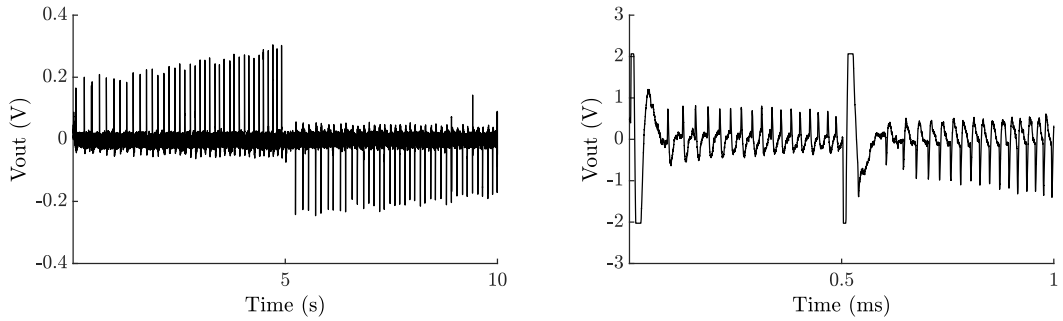

(a) (b)

Figure 3.11: Experimental SMI signals resulting from modulating the laser with different modulation frequency when the target is fixed at 1.2 m from the target: (a) 100 mHz. (b) 1 kHz.

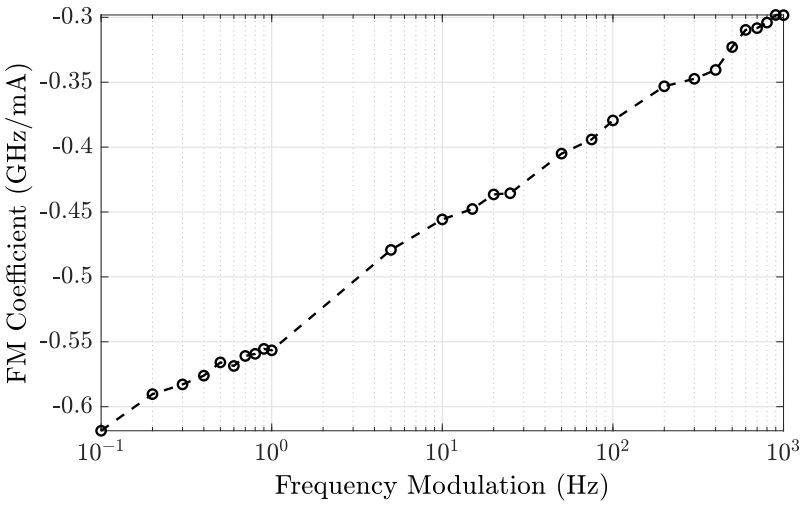

Figure 3.12: Experimental measurement of FM coefficient as a function of modulation frequency.

These results show that the FM coefficient decreases with the increase of frequency modulation. It should be highlighted that the change between the modulation ramps induces ring oscillation in the SMI signal. With higher frequency modulations and it becomes larger in time causing the reducing the number of interferometric fringes as shown in Figure 3.11(b) when the laser diode is modulated with 1 kHz of modulation

frequency compare to the 100 mHz modulation frequency shown in Figure 3.11(a). The next section will discuss how the bias injection current changes the SMI absolute distance measurement.

3.3.3 | Laser injection current

As we can see in Eq. (2.77), the SMI output power is proportional to the laser injection current in any form of modulation. As we will demonstrate in this section, it also largely affect the behaviour of the SMI sensor. The changes in the injection current affect the lasing wavelength by two different processes−the plasma effect and the thermal effect. The plasma effect refers to the impact of injection current in the refractive index of the material inside the laser diode which in turn affects the laser wavelength. Otherwise, the thermal effects are the result of the heat being built up inside the laser cavity which causes the changes to various properties of the laser diode including the intracavity L_{in} and the refractive index of the cavity by means of the optical gain profile. Those changes properties are proportional to the laser emission frequency. It is very interesting to highlight that the thermal effect seems to be dominant when the laser diode is modulated at lower frequencies. On the other hand, the plasma effect becomes dominant when the laser diode is modulated at higher frequencies [56].

First, we investigate the influence of the laser injection current on the number of interferometric fringes in the SMI signal. By using the same experimental setup shown in Figure 3.10, the laser diode is biased with different values of DC current and modulated with 10 mA peak-to-peak of amplitude at 50 Hz of frequency with triangle waveform. The target is a white paper that is fixed at 1.2 m from the laser. The SMI signals with different values of laser injections current are shown in Figure 3.13.

As can be seen in Figure 3.13, the number of interferometric fringes in the SMI signal changes with the laser biasing current while the other parameters (L_{ext}, modulation amplitude and frequency, ...) are kept constant. The SMI signal results in twenty-five interferometric fringes in each half of the triangle waveform when the laser diode is operated with injection current 12.5 mA. However, this number changes to twenty-six, twenty-eight and twenty-nine when the laser diode is injected with the current of 15 mA, 17.5 mA and 20 mA, respectively.

Figure 3.14 shows the SMI signals for the same distance between the laser and the target from the previous experiment, but we covered the target surface with the microsphere reflective tape instead of white paper. When the laser diode is operated with 12 mA of laser injection current (2 times of its threshold), the SMI signal exhibit a chaotic behaviour in Figure 3.14(a); while, for the same feedback level, the SMI signal

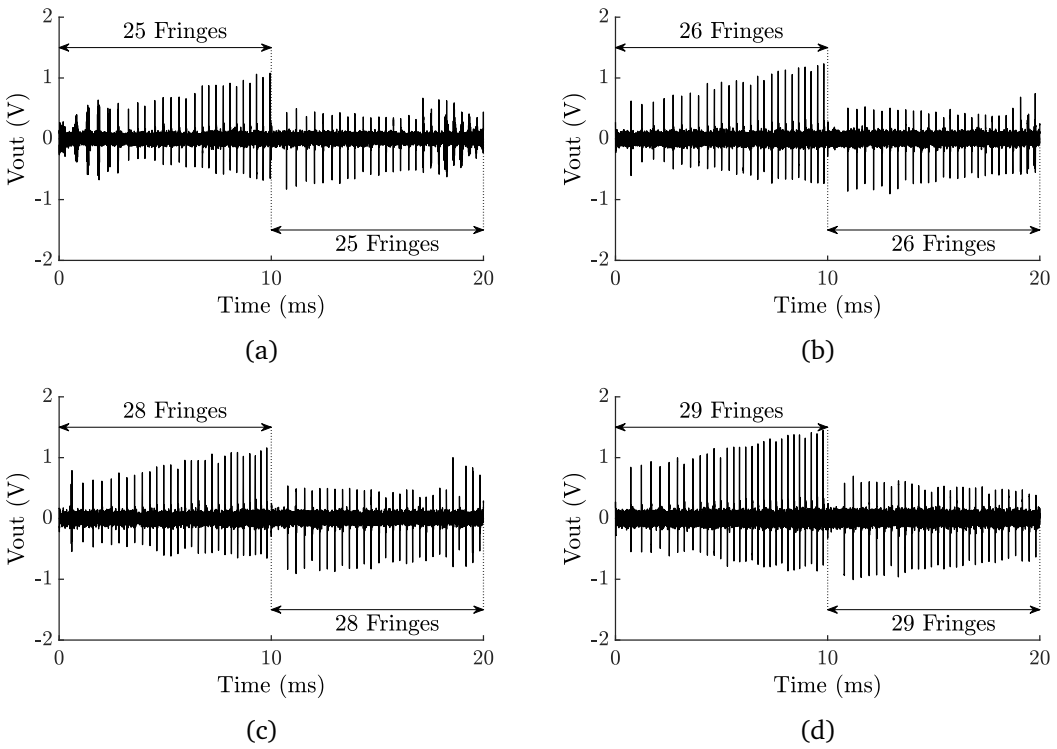

Figure 3.13: The results of experiment of SMI absolute distance with different injection currents under $10\,\mathrm{mA}$ peak-to-peak of current amplitude at $50\,\mathrm{Hz}$ frequency modulation with the target distance of 1.2 m. (a) $12.5\,\mathrm{mA}$. (b) $15\,\mathrm{mA}$. (c) $17.5\,\mathrm{mA}$. (d) $20\,\mathrm{mA}$.

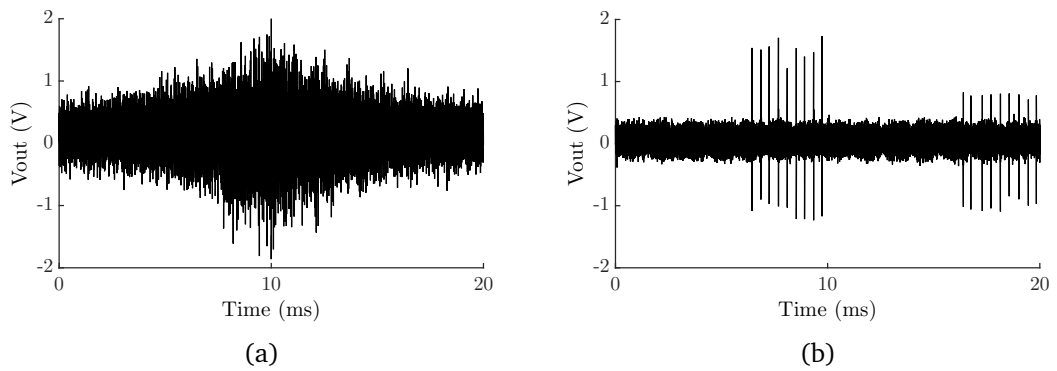

Figure 3.14: The results of experiment of SMI absolute distance with different injection currents under $10\,\mathrm{mA}$ peak-to-peak of current amplitude at $50\,\mathrm{Hz}$ of the frequency modulation. (a) $12\,\mathrm{mA}$. (b) $20\,\mathrm{mA}$.

keep showing interferometric fringe when the laser is operated with 20 mA of injection current (3.35 times of its threshold) in Figure 3.14(b).

3.3.4 | Distant fringe frequency

The non-linearity between the laser injection current and the laser emission frequency produces a non-linear emission frequency ramping while the current is modulated in a linear fashion by a triangle signal. A 5 mA peak-to-peak of current amplitude at 10 Hz frequency modulates a 20 mA biased laser diode. The target surface covered by a white paper is fixed at 1.5 m from the laser facet. The SMI signal results in twenty-one visible fringes for each half of the triangle waveform.

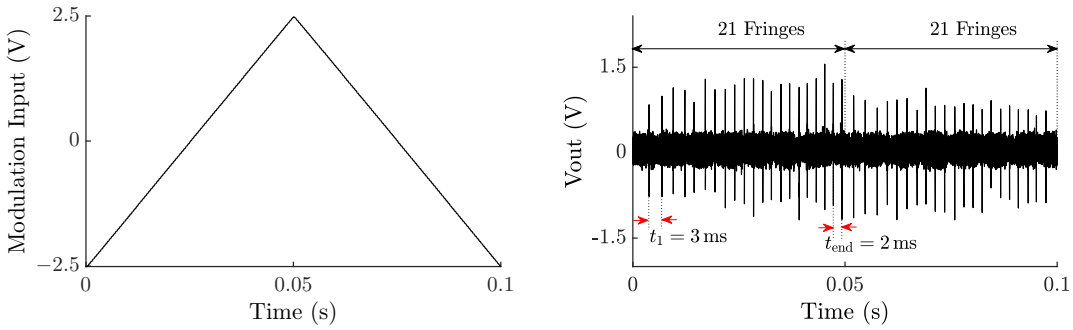

(a) (b)

Figure 3.15: Experimental signal acquisition for the distance of $1.5\,\mathrm{m}$ with $20\,\mathrm{mA}$ injection current: (a) The input voltage to the driving circuit which then converted in to a current with corresponding current fluctuation of $5\,\mathrm{mA}$ peak-to-peak triangle modulation at $10\,\mathrm{Hz}$ of frequency; (b) the SMI distant signal resulting from a linear modulated current ramping.

The fringe frequency in each half of the triangle waveform keeps increasing over time. Considering the $f_{\mathrm{b},1}$ and $f_{\mathrm{b},2}$ are the fringe frequencies during the increase and decrease ramp of the modulation, the expression (3.7) can be rewritten as,

$$f_{\mathrm{b},1} = f_{\mathrm{b},2} = \tau_{\mathrm{ext}} \frac{d\nu_{\mathrm{th}}}{dt}. \tag{3.11}$$

We suppose that the modulated emission frequency resulting from the linear current modulation in the triangle waveform is $\nu_{\mathrm{th}}(t) = \nu_{\mathrm{th}} + A.\exp(t/\tau)$, where A is either positive or negative depending on the laser emission frequency modulation ramps. Then the fringe frequencies in (3.11) can be re-written in the function of time as,

$$f_{\mathrm{b},1} = f_{\mathrm{b},2} = \frac{\tau_{\mathrm{ext}}.A}{\tau} \exp(t/\tau). \tag{3.12}$$

Since the derivations of both $f_{\mathrm{b},1}$ and $f_{\mathrm{b},2}$ have the same sign, then the fringe frequencies in each half of the triangle waveform are expected to increase over time. Figure 3.16 sketches a linear triangle modulation in laser injection current that results in non-linear

in the laser emission frequency. As a result, the fringe frequencies in the SMI signal are not constant and keeps increasing over time. This can also be seen experimentally in the SMI signal shown in Figure 3.15(b) where the fringe frequencies for both modulation ramps keep increasing.

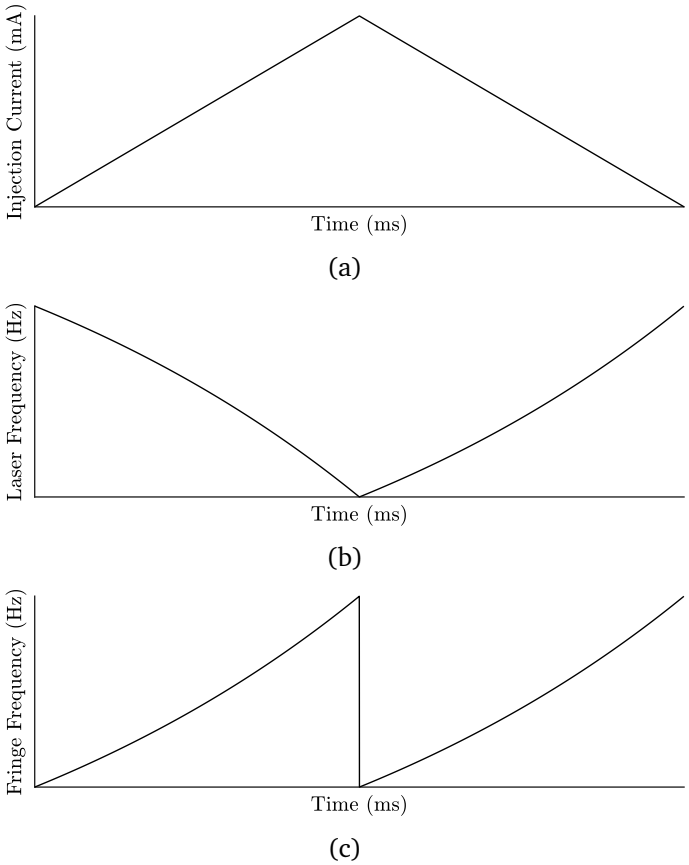

Figure 3.16: An assuming plot: (a) A full cycle of linear triangle modulation of injection current in function of time. (b) The non-linearity of the laser frequency caused by linear modulation of triangle waveform. (c) The result of non-constant of fringe frequency in the optical output power.

With the experimental result in Figure 3.15(b) and the assuming the interpretation depicted in Figure 3.16, parameters A and τ in Eq. (3.12) can be determined by applying the curve fitting toolbox in MATLAB to fit the curve of the fringe frequency resulting from the SMI signal. With the curve fitting toolbox, it gives $A\tau_{\text{ext}}/\tau = 362.67$ and $\tau = 0.132$. As the target is fixed at a distance of 1.5 m from the laser, the external round-trip propagation time results in 10 ns with the external refractive index $n_{\text{ext}} = 1$. By applying these values of A and τ into the expression of laser emission frequency without feedback, then into the excess phase equation, the derivative of output power can be

plotted in Figure 3.17(b).

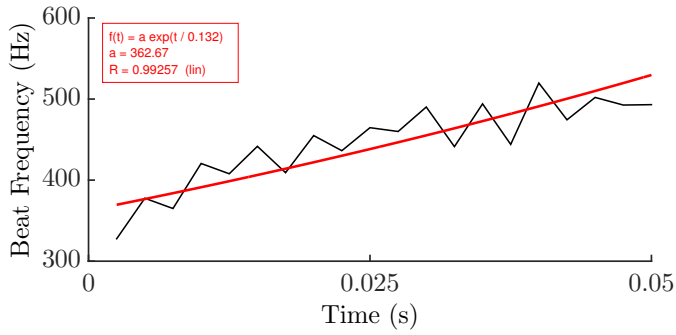

(a)

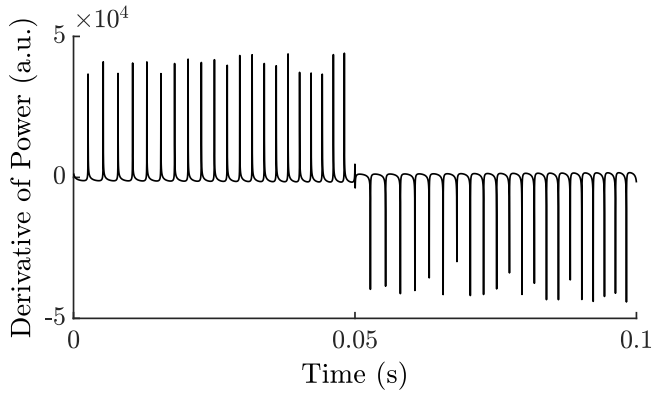

(b)

Figure 3.17: (a) Plot the measurement result of fringe frequency indicated in black solid lines and the curve fitting from MATLAB Toolbox indicated in the red solid line. (b) Plot SMI absolute distance with the obtained parameters in (a) under the optical feedback level $C = 0.9$.

The simulation of the SMI derivated signal shows twenty-one interferometric fringes in each half of the triangle waveform which agrees to the experimental result in Figure 3.15(b). Moreover, the simulation result also demonstrates that the fringe frequencies are varying in both ramps of modulation. This variation will affect on the measurement resolution and it will be discussed later.

3.3.5 | Fringe disappearance experiment

A block diagram of the experimental setup is depicted in Figure 3.18. The two variable optical attenuators (Thorlabs NDC-50S-1 and NDC-50S-3) are displayed along the laser-target path to control the back-scattered light intensity. A 50/50 beam splitter is used to split the incident light beam from the laser—half goes to a tilt mirror to avoid the

reflected light back to the beam splitter and maintain the SMI system in a single cavity mode, and another half traverses the distance target to another mirror via the two variable optical attenuators. Then the beam splitter collects 50% of the reflected light from the target in the front-end detector of a power-meter through a collimating lens. The target is a protected silver mirror (Thorlabs PF10-03-P01) located at a distance of 1.5 m from the sensor. The laser diode is operated with a bias current of 20 mA (around 3.34 times its threshold current of 6 mA) and modulated with a 5 mA peak-to-peak amplitude triangle waveform. The photodetected signal then is converted to the voltage by a transimpedance amplifier with a gain of 40 dB and a selective bandwidth ranging from 40 Hz to 300 kHz thus allowing to reject the triangle modulation of frequency 10 Hz.

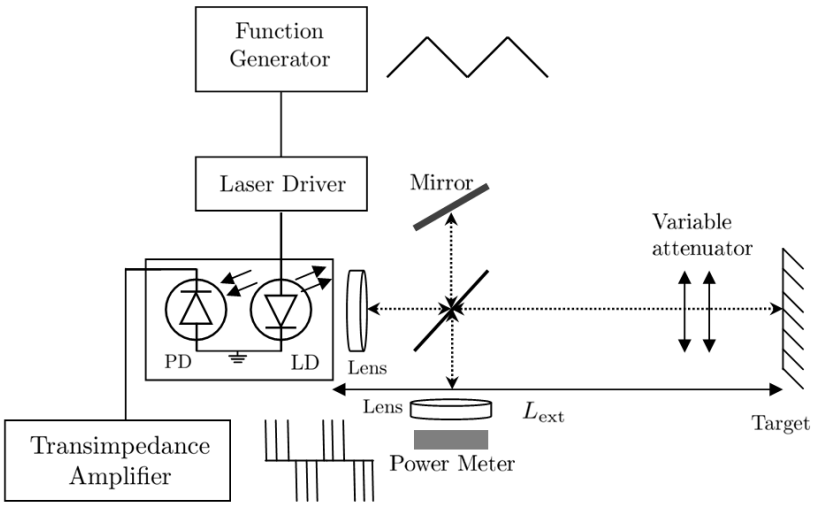

Figure 3.18: Block diagram of experimental setup. Laser and photodiode are in the same package.

Two parameters are characterized experimentally: the FM coefficient Ω and the amplitude reflectivity of the back-scattered light r_{ext} for the different attenuation conditions in the external cavity. The frequency modulation coefficient is estimated through the experimental results of counting the interferometric fringes in the weak feedback regime, and it results -430 MHz/mA at 10 Hz of frequency modulation.

The two variable optical attenuators propose eight different attenuation values resulting in sixty-four different feedback levels. Without any attenuators, the amplitude reflectivity coefficient r_{ext} is measured to be 30.12%. The lowest amplitude reflectivity is 0.24%, and twenty-one interferometric fringes per ramp of the triangle modulation are observed. The output power keeps resulting with twenty-one fringes with the target's

amplitude reflectivity up to 1.79%. When the amplitude reflectivity is 2.37%, a pair of fringes disappears, then another pair of fringes disappears for a reflectivity of 2.97%. The fringes keep on disappearing as the reflectivity increases, and once it reaches to 25.54%, all the twenty one fringes are lost.

Figure 3.19 shows some experimental results with different reflectivities: 1.77%, 2.37%, 2.97%, 8.61%, 13.06%, 15.86%, 21.08% and 25.54%. The experiment in Figure 3.19(a) shows twenty-one interferometric fringes at the output with 1.77% of amplitude reflectivity while for the different reflectivities. Figures 3.19(b), and 3.19(c), the number of fringes decreases to twenty and nineteen respectively. Then fifteen, eleven, nine and three interferometric fringes appears in the output power when the reflectivity coefficient continues to increase as shown in Figures 3.19(d), Figures 3.19(e), Figures 3.19(f), and Figures 3.19(g) respectively. In the Figure3.19(h), no interferometric fringe appears which means twenty-one fringes are lost.

Using the feedback parameter C in Eq. (2.32), the excess phase equation in Eq. (2.74) to solve the phase response, the phase stimulus in Eq. (3.8) and the output optical power in Eq. (2.77) with realistic intrinsic parameters in Table 3.1, the reinjection loss factor ε, with the values measured for the FM coefficient and the reflectivities r_{ext} and the MATLAB scripts, Figure 3.20 shows the simulation of the derivative of laser power for one period of modulation. The simulation results show a good agreement with the experimental results in particular as concerning the number of missing fringes in each case.

In order to validate the expression in (2.92), the evolution of the interferometric fringes disappearance as a function of the feedback parameter C is plotted in Figure 3.21, both experimentally and theoretically taking optimized value $C_1 = 4.84$ and $C_2 = 7.44$ as the value where the first and the second fringes would have disappeared. As can be observed, the model depicted by Eq. (2.92) is in great agreement with the observed experimental results, and thus they validate the explanation of fringe disappearance.

It should be highlighted that the experiments in this section are achieved without the initial condition when the laser diode first experiences the current modulation. So the number of interferometric fringes in each half of the triangle waveform is equal.

3.3.6 | Fringes disappearance behaviour

The fringe disappearance behaviour in the SMI absolute distance has been theoretically discussed with the rate equations in Section 3.2.2. The number of missing fringes is not always the same between the first and the following ramp of the triangle waveform in the output power when the laser first experience with current modulation. This behaviour in the simulation is also observed in practice. The same experimental setup in Figure 3.18

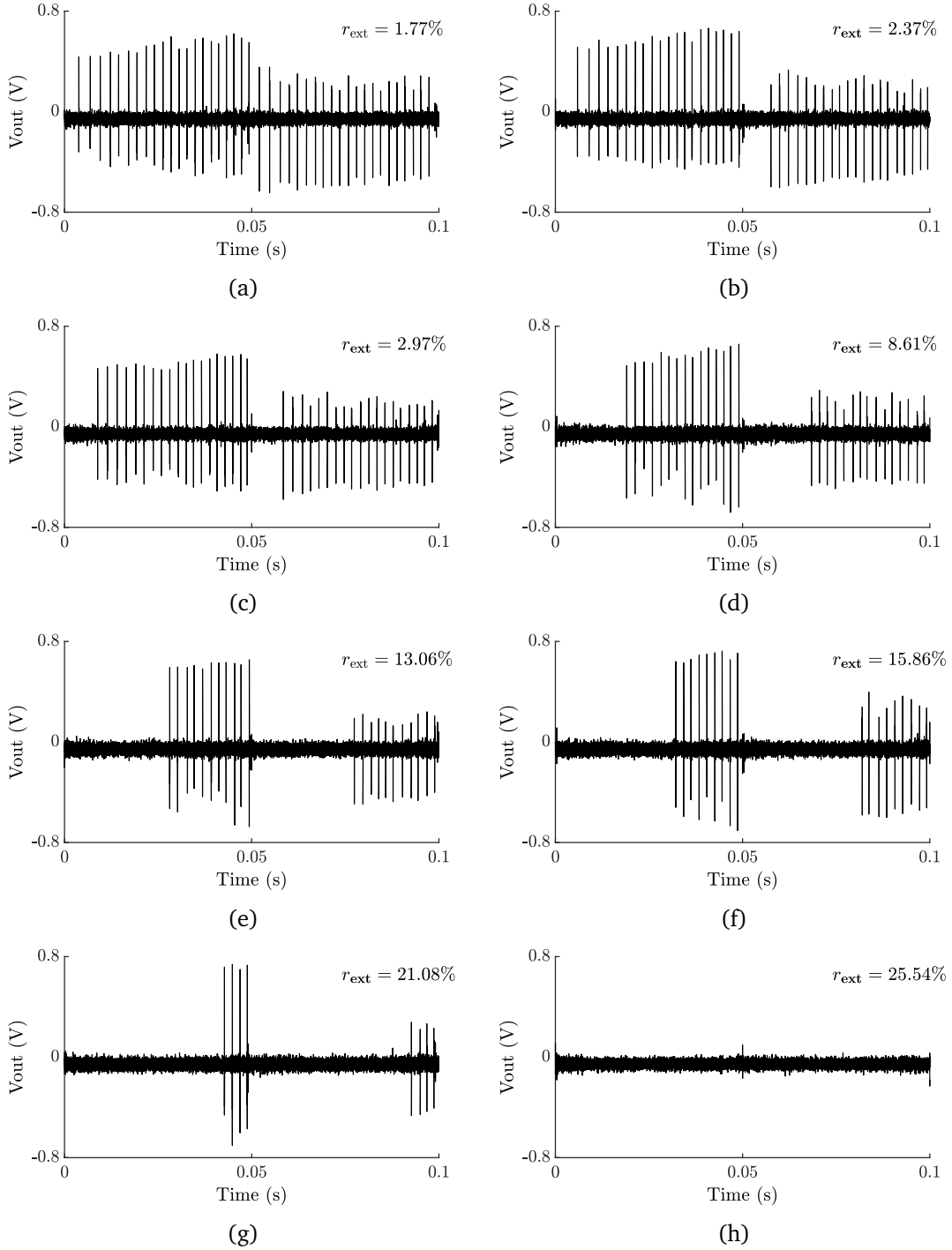

Figure 3.19: Experimental SMI signal acquisition for the distance of 1.5 m with different target's amplitude reflectivities. (a) 1.77%. (b) 2.37%. (c) 2.97%. (d) 8.61%. (e) 13.06%. (f) 15.86%. (g) 21.08%. (h) 25.54%.

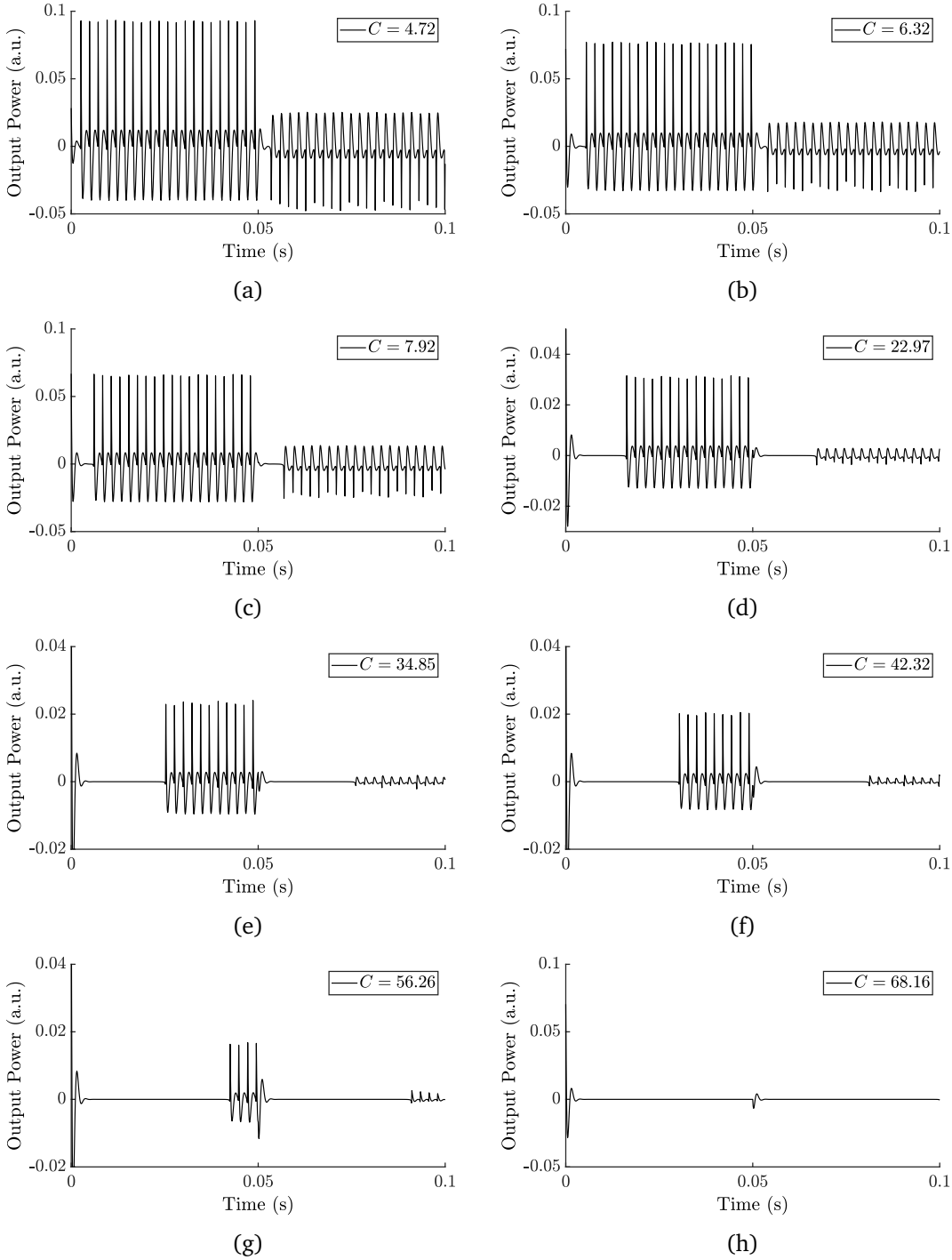

Figure 3.20: Simulation SMI output power in time for the distance of 1.5 m with different target's amplitude reflectivities. (a) 1.77%. (b) 2.37%. (c) 2.97%. (d) 8.61%. (e) 13.06%. (f) 15.86%. (g) 21.08%. (h) 25.54%.

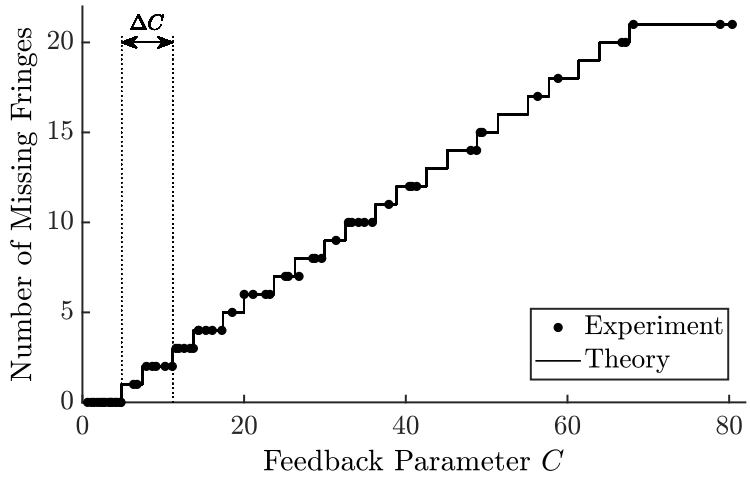

Figure 3.21: The behaviour of the interferometric fringe disappearance and the feedback parameter C. The thin solid lines show the result of interferometric fringes disappearance in theory and the marker points shows the results of the experiment.

is used for the demonstration. The target is a mirror that fixed at a distance of 1.2 m. The laser diode is operated with a bias injection current of 20 mA and modulated with a 5 mA peak-to-peak amplitude at 1 Hz frequency with the triangle waveform. The FM coefficient is calculated to be -543 MHz/mA in this measurement condition.

With a very low reflection from the target, the SMI signal would have resulted in 22 interferometric fringes in each ramp of the triangle modulation. With high re-injected lights from the target, the SMI output power experiences the fringe missing phenomenon, and Figure 3.22 demonstrates some of the experimental results of the SMI signals under three different external reflection coefficients including the initial condition where the laser diode first experiences with the current modulation.

Figure 3.22(a) displays the SMI signal with fourteen and seven observed interferometric fringes in the first then the following ramp of the triangle modulation. By ignoring the first modulation ramp, fourteen fringes have been disappeared in the SMI signal. This number of missing fringes can be used to estimate the feedback C through the graph displayed in Figure 2.10 or the expression (2.92).

With fourteen of missing fringes per each half of the triangle waveform, the laser with the optical feedback should be operated under the feedback level C between $13\pi + 1 < C < 15\pi + 1$. Using a feedback level $C = 47$ into the model SMI derivative of output power is plotted in Figure 3.23(a) where it shows a good agreement with the experimental result.

With a similar approach with the experimental result shown in Figure 3.22(b), only three fringes appear in the second and following modulation ramp while twelve fringes appear in the first ramp of the modulation signal. So, eighteen fringes are considered as missing fringes in the SMI signal; then the feedback level C should be in between $17\pi + 1 < C < 19\pi + 1$. By applying $C = 60$ to the SMI absolute distance rate equation, output power numerical solution infallibly corresponds to the experimental result as shown in Figure Figure 3.23(b). Last but not least the experimental result of the SMI output shown in Figure 3.22(c), the first half of the triangle waveform displays ten interferometric fringes, but no fringes can be observed in the following ramps. The laser should be operated under the feedback parameter C greater than $22\pi+1$. Then we try the feedback $C = 75$ to the distance rate equation, the simulation result displayed in Figure 3.23(c) corresponds to the experimental result shown in Figure. 3.22(c).

As discussed and explained in Section 3.2.2 with the experimental results in Figure 3.22 and simulation results in Figure 3.23, it is clear that that the lasing mode in the moderate/strong feedback regimes would dwell the stable solution starting from the high beginning of the phase stimulus. It is interesting to notice that if the current modulation is paused for a period of time and the laser diode does not turn off, the lasing mode would keep the previous solution path. It means if the laser injection current is re-modulated, the lasing mode will dwell on the stable solution back and forth with the same path from the previous modulation cycle.

Figure 3.24(a) displays the extension of injection current triangle modulation including a period of constant time. The laser injection current is first modulated with two cycles in the triangle waveform then stays constant for a period of time without any form of modulation before being re-modulated with another two more cycles of the triangle waveform with the same amplitude and frequency modulation. Figure 3.24(b) shows the simulation of the SMI absolute distance rate equations resulting from the current modulation in Figure 3.24(a).

As we can see in the simulation result, the derivated power of the first and second cycle of triangle modulation gives the same result depicted in Figure 3.23(a); then no fringe appears when the injection current remains constant for an amount of time (causing no fluctuation in laser emission frequency). Later, when the laser injection current is re-modulated again, the derivative of output power produces in the same number of fringes as in the second modulation cycle of the previous modulation phase. It can be explained as the lasing mode does not jump back to the initial condition the lasing solution, but dwells the stable path as in the previous modulation.

Figure 3.25(a) shows the experimental result with the current modulation of Figure 3.24(a) that shows a good an agreement with the simulation result depicted in Fig-

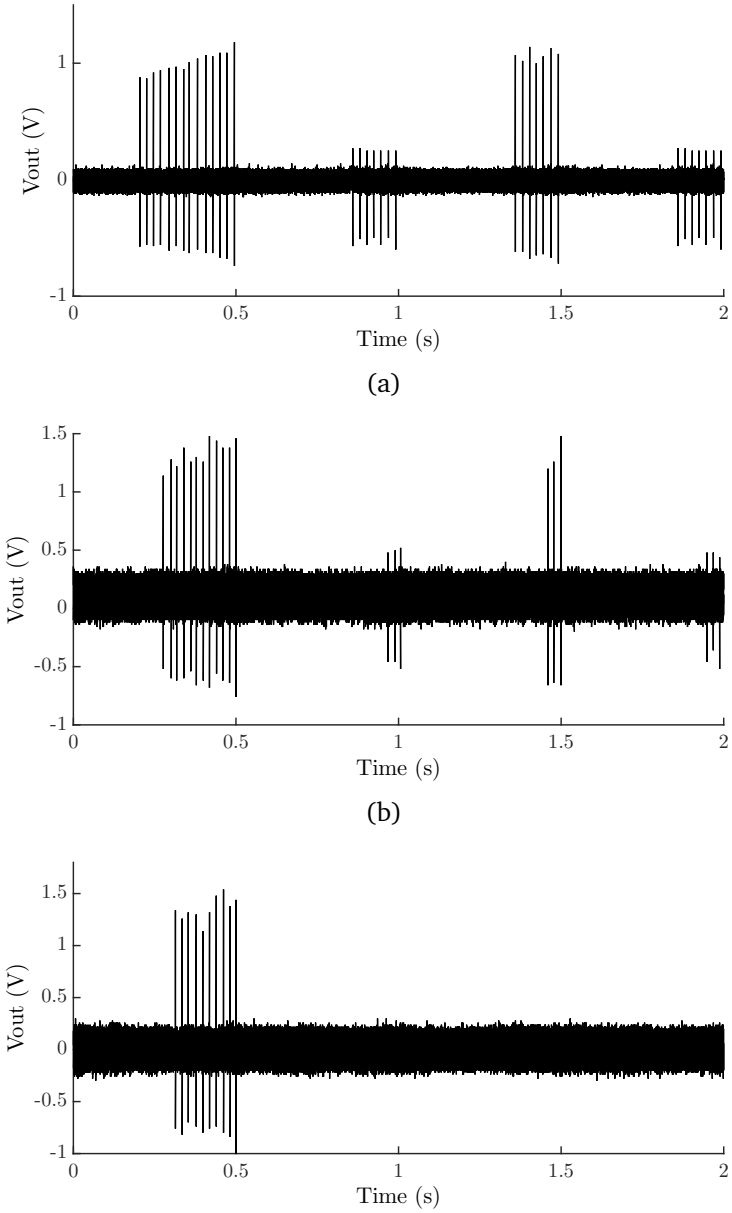

Figure 3.22: Experimental SMI signal acquisition for the target distance of 1.2 m with different amplitude reflection coefficients when the laser diode is operated with 20 mA of injection current and 5 mA of current's amplitude at 1 Hz of frequency modulation.

ure 3.24(b).

However, if there is any perturbation in the lasing frequency after being modulated the injection current, the lasing mode will restart from the lasing solution of the ini-

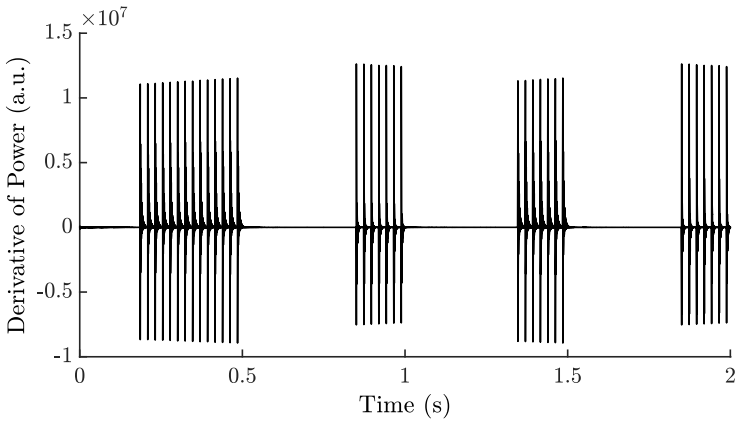

(a)

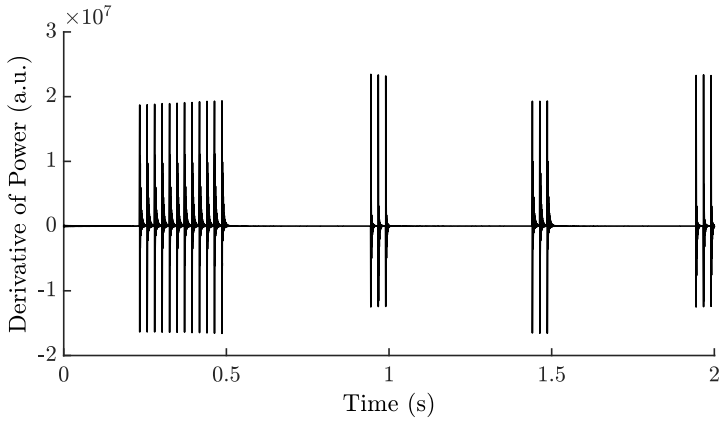

(b)

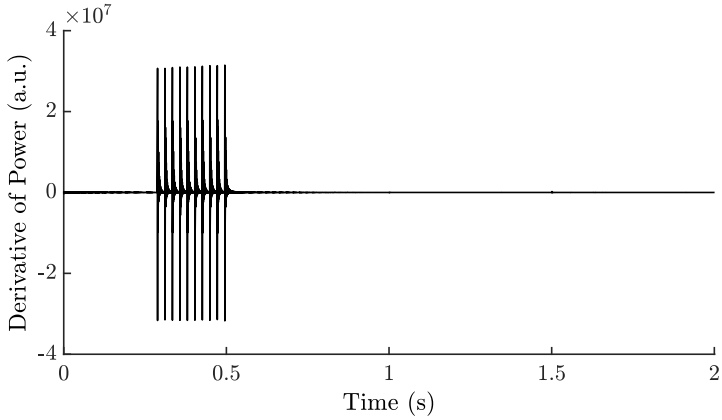

(c)

Figure 3.23: Simulation SMI output power in time for the distance of 1.2 m with different values feedback parameter C. (a) $C = 47$. (b) $C = 60$. (c) $C = 75$.

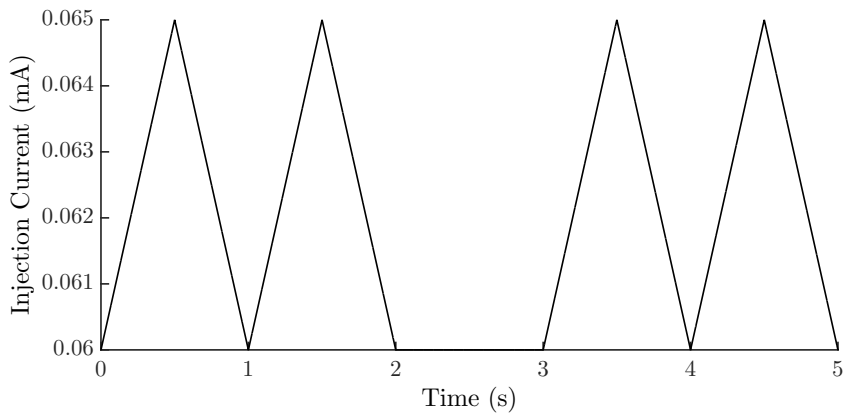

(a)

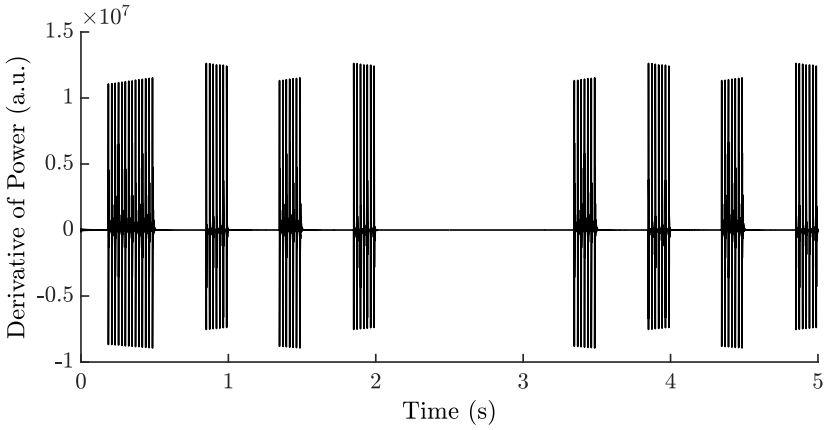

(b)

Figure 3.24: (a) Plot laser diode bias injection current in triangle waveform and constant. (b) Plot SMI absolute distance through the rate equation with the form of injection current in (a) under the feedback parameter $C = 47$.

tial condition that corresponds the highest/lowest stable solution of the phase stimulus (depending on increasing or decreasing portion sweeping). Figure 3.25(b) displays the experimental result when the perturbations occur at a time where the laser injection current is constant without any form of modulation. The perturbations are caused by an object inserted between the laser and the target. The perturbation causes the lasing solution to return back to the initial condition where fourteen interferometric fringes appear on the half of the triangle waveform in the SMI signal−the same observed number of fringes when the laser first experiences current modulation.

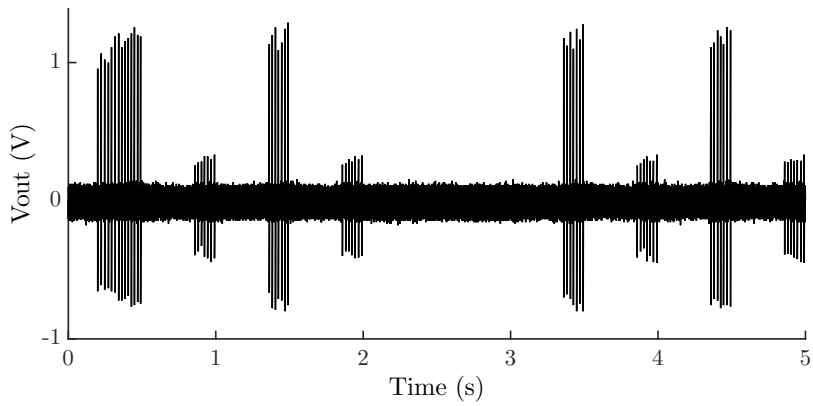

(a)

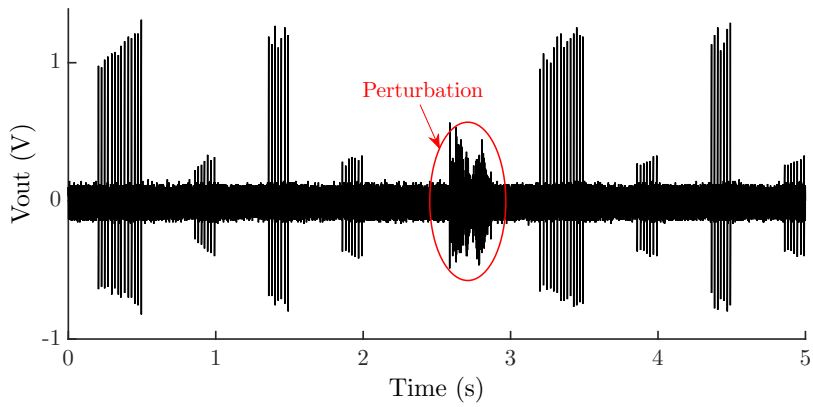

(b)

Figure 3.25: Experimental SMI signal acquisition with the same target's amplitude reflectivities. (a) Without any perturbation during the propagation of light between the laser and the target. (b) With perturbation occurring during light propagation which then restarts the lasing mode from the previous solution path.

3.3.7 | Measurement error

The experiment setup is described in Figure 3.10. The target is located at distances ranging from 20 cm to 1.5 m from the sensor. The target surface is covered by microprismatic reflective tape. The laser diode is operated with 20 mA of injection current and modulated with 10 mA peak-to-peak amplitude at 100 Hz frequency. The FM coefficient is experimentally measured to be -354 MHz/mA through the average time spacing between the fringes method and at the distance of 1.2 m in the weak feedback regime; this value will be used to determine the external cavity distance in this section.

With raw current modulation, the laser emission frequency does not linearly vary

with the bias injection current. The non-linearity between the bias injection current and the laser emission frequency produces the unevenly spaces between fringes in the output power, and this variation decreases the measurement resolution. With high amplitude reflectivity form the external target at a certain distance, the fringe missing phenomenon will occur at the beginning for an amount of time before a solid fringe would appear in the SMI signal. This phenomenon causes a huge error in the distance calculation while using the fringe counting method. Then, the alternative method, the average time spacing between the fringes, is used to determine the distance in this case.

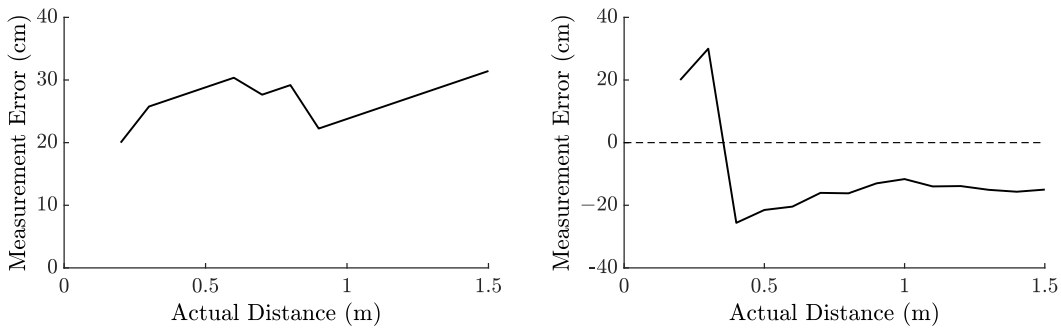

(a) (b)

Figure 3.26: The results of distant measurement of the microprismatic reflective tape with different methods of calculation. (a) The counting number of appeared interferometric fringes. (b) The average time spacing between the appeared interferometric fringes.

At 20 cm and 30 cm, the SMI signal displays no and one interferometric fringe, respectively. It is important to note that the average time spacing between the fringes method needs at least two consecutive fringes in the output power. When the distance between the laser and the target is getting longer, the SMI signal starts showing more fringes with the fringe missing phenomenon at the beginning of the ramp. With the fringe counting method, the measurement resolution shows huge errors compared to the actual distance (more than 20 cm); while the average time spacing between the fringe method can improve the measurement resolution up to less than 10 cm absolute error.

However, this measurement resolution remains quite low as compared to the actual distance, and this is because of the non-linear relationship between the laser injection current and the laser emission frequency that causes the fringe frequencies to rise up over time for each half of the triangle modulation. The wider space at the beginning of the SMI signal caused by the fringe missing phenomenon results in lowering the average time space between the fringes. As shown in Figure 3.26(b), the measured distances are indeed bigger than the actual distances.

With the assumption discussed in subsection 3.3.4, the fringe frequency is exponentially increased with time and thus, the variation of the laser emission frequency can also be found. In order to take into account this phenomenon, the FM coefficient can be expressed as an exponential function of time for a given modulation ramp. We propose to consider the variation of the variation of laser emission frequency in Eq. (3.1) and an exponential variation $\nu_{\text{th}}(t) = \nu_{\text{th}} + A.\exp(t/\tau)$, so the FM coefficient gives,

$$\Omega(t) = \left(\frac{|\nu_{\text{th,max}} - \nu_{\text{th,min}}|}{\triangle I}\right).\exp(t/\tau). \tag{3.13}$$

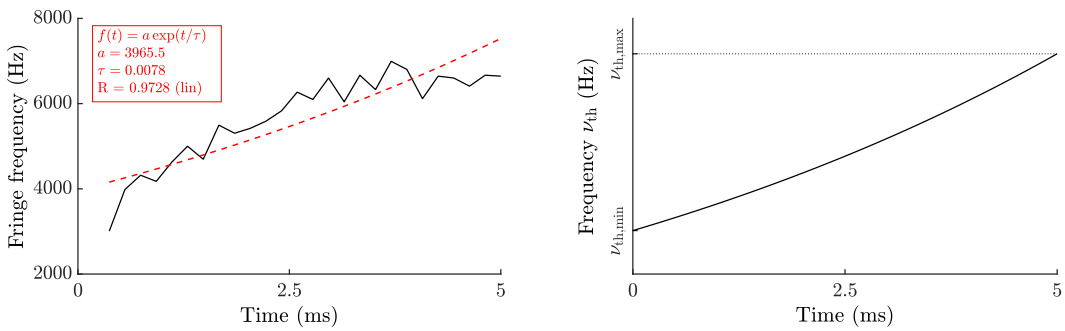

(a) (b)

Figure 3.27: (a) Experimental result of fringe frequency at the distance of 1.2 m when the laser diode is modulated with amplitude 10 mA peak-to-peak at 100 Hz frequency modulation indicated in black solid lines, and MATLAB curve fitting is used to define the constant parameter A and τ indicated in red solid line. (b) Laser emission frequency in function of time resulting from curve fitting parameters in (a).

From the fringe frequencies in the SMI signal, while the laser is operated under the weak feedback regime resulting from the triangle waveform modulation, a curve fitting is applied to find the parameters A and τ in the expression (3.12) as shown in Figure 3.27(a). Then the change in laser emission frequency resulting from modulating the laser injection current can be plotted which then its minimum and maximum value can be determined as shown in Figure 3.27(b). So the exponential graph of the FM coefficient in Eq. (3.13) is plotted as shown in Figure 3.28, and it is then used to calculate the distance between the laser and the target. The time location of the first solid observed interferometric fringe corresponds to the value of the FM coefficient where it is used to calculate the distance, i.e., $\Omega = -403$ GHz/mA given from the result of SMI signal demi-period of modulation at the distance of 1 m where the interferometric fringe disappearance occurs in this case. From the distance of 40 cm, more than two interferometric fringes are presented in each ramp of modulation which lets us to determine the fringe

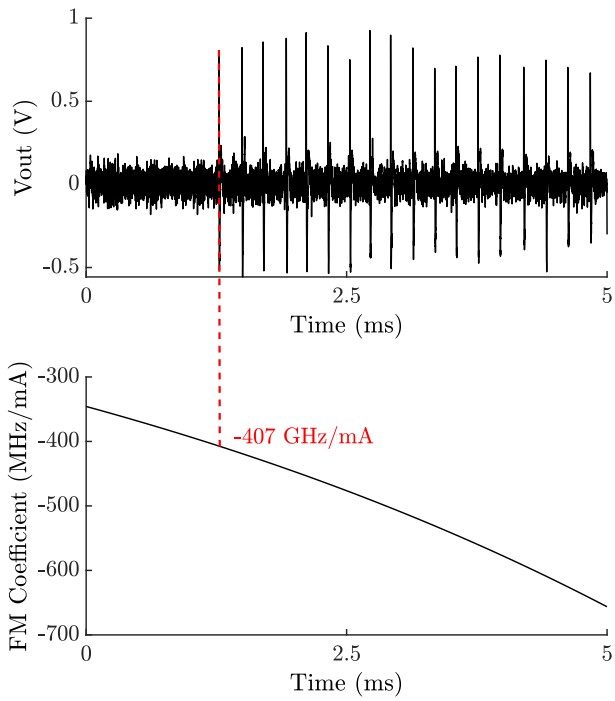

Figure 3.28: Determine FM coefficient value from the plot FM coefficient in function of time resulting from curve fitting of the laser emission frequency with the SMI signal demi-period of modulation when the target covered by the microprismatic reflective tape is fixed at a distance of 1 m.

frequency for the distance's calculation. Each experiment results in different FM coefficient; and Figure 3.29 exposes the different results of measurement error calculation between the FM coefficient compensation and the constant value of FM coefficient (i.e., Ω= -354 MHz/mA).

The new measurement error of the distance between the laser and the target covered by reflective tape in this experiment can be improved to a few centimetres with the average time spacing method including the compensation of the FM coefficient as shown in Figure 3.29.

3.4 | Conclusion

The measurement of distance based on the SMI technique can be achieved when the laser emission frequency is modulated with an ostensibly triangle waveform. This frequency modulation can easily be obtained by modulating the laser injection current. However,

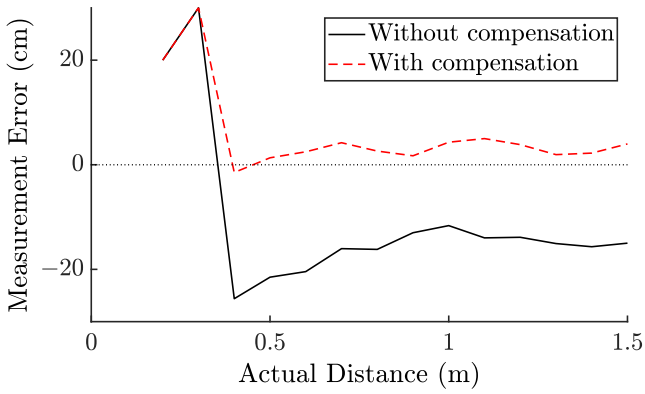

Figure 3.29: Measurement error with time spacing method: the solid black line measured with Ω= -354 MHz/mA and the solid red line measured with the exponential of the FM coefficient resulting from the fringe frequency under the weak optical feedback regime.

in practice, the laser emission frequency does not linearly change with the laser injection current due to the plasma and thermal effects produced inside the laser cavity. To determine the distance between the sensor and the target, a few methods can be used such as counting the number of the appeared interferometric fringes in the SMI signal, averaging time spacing between fringes and the fringe frequency resulting from the FFT. However, at least two observable fringes are needed to measure the with the average time spacing method. The absolute distance measurement with the SMI sensor is far from the trivial because it is subject to various undesirable effects which are not encountered with a conventional interferometric system. Different target surfaces will outcome the number and location of the observed fringes differently. The higher amplitude reflection coefficient from the external target causes more fringes to disappear or, in the worst case, produces the chaotic behaviour in the SMI signal. The missing fringes in the SMI signal caused by the level of back-scattered light from the target can be explained theoretically by the factor feedback C in Chapter 2. The experimental results of fringe disappearance behaviour conducted with the absolute distance measurement by controlling the level of back-scattered light from the target with two variable optical attenuators show a good validation with a proposed model in Chapter where two interferometric fringes disappear in the SMI signal with the increment in feedback level C by 2π. One important remark is the behaviour of the fringe disappearance in the SMI signal sensor. The number of missing fringes in the SMI signal can be different between the first modulation ramp and the others. The reason for this situation can be explained with the stable solution in the excess phase equation when there are multiple stable solutions at the same coordinate of the phase stimulus either the maximum or the minimum. The lasing mode

will start from the lowest stable solution at the minimum of the phase stimulus or the highest stable solution at the maximum of the phase stimulus depending on its direction whether it is increasing or decreasing. Then the lasing solution will follow the stable path back and forth between two points resulting in the same number of interferometric fringes for following ramps of modulation. However, if any perturbation occurs in the laser frequency after the laser being modulated the injection current, the lasing mode will restart from the lasing solution of the initial condition. With raw current modulation, the laser emission frequency does not linearly vary with the bias injection current. The non-linearity between the bias injection current and the laser emission frequency produces the unevenly spaces between fringes in the SMI signal where the fringe frequency is exponentially increased with time. From this variation, the FM coefficient is also assumed varying with time. So, the measurement error when the fringe disappearance phenomenon occurs in the SMI signal can be compensated by choosing a value of the right FM coefficient. The FM coefficient of the measurement is determined at the time when the first solid interferometric fringe appears. It should be highlighted that the exponential graph of FM coefficient needs to be plotted and it depends on the laser diode, the amplitude of current modulation, and the modulation frequency.

Furthermore, in many distance measurement applications, the target or the sensor is in motion where the Doppler is added into the system. So, the objective of chapter 4 is therefore to analyse the interaction between these two effects in the SMI technique.

4

Combined Distance and Velocity Measurement

Today a number of different optical techniques capable of measuring target's distance and velocity or both exist. The most obvious optical method for measuring the velocity of a moving target is to use the Doppler effect where light reflected from the moving target will be shifted in frequency in proportion to the velocity of the target. A well-known optical technique to measure the Doppler frequency is LiDAR (Light detection and ranging). Traditional LiDARs use the time difference between pulses to measure velocity. In contrary, the target's velocity measurement based on the SMI technique uses the interference of the light inside the laser cavity and the backscattered light containing the Doppler information from the moving target. Measuring both the target's distance and verity is also possible with the SMI technique. By modulating current supplied to the laser diode in triangle waveform which results in modulating the laser emission frequency, both target's distance and velocity can be determined from the measured two beat frequencies at the output power. Measuring the distance and velocity of a system gives fundamental information about its behaviour and also how it may evolve over time. Because of the capability of measuring the distance and velocity at the same time, it is possible to determine the profile and speed of the moving target.

Before going further to the application of measuring the external cavity length and the target velocity at the same time, we should first explore the velocity alone. The velocity of the target can be modelled with two different approaches—the target moves along the longitudinal axis of the laser beam (that is the case for displacement or vibration) and the target translates at a fixed distance from the laser (that is the case of many applications, rotating target, flowing target, etc.). In the first case, the external cavity length varies in time, and the external round-trip propagation time is then rewritten as,

$$\tau_{\text{ext}}(t) = n_{\text{ext}} \frac{2\big(L_{\text{ext}} + \upsilon(t)\big)}{c}, \tag{4.1}$$

where υ is the displacement speed of the target along the optical axis.

With this application, the direction of the moving target (backwards or forwards the laser facet) along the longitudinal axis of the laser beam is easily interpreted as described in Chapter 2.

However, in case of the fixed target that has the velocity (i.e., rotating disc, flow measurement), the target is stationary over time but has instantaneous velocity along the longitudinal axis of the laser beam which imparts a frequency shift to light incident upon it. The laser diode as a monochromatic propagates the light on the surface of the rotating target at the distance L_{ext} between the laser and the target, and the light then scatters off the target which creates a Doppler shift. We will detail this in the following section.

4.1 | Laser Doppler

The Doppler measurement technique based on the laser was first demonstrated by many researchers in the late 1970s [81, 82, 83]. The velocity information from the scattering rotating or translating target is contained in the scattered fields due to the Doppler effect.

4.1.1 | Modelling

The configuration of the SMI Doppler velocimetry is illustrated in Figure 4.1. When the laser beam (characterised by the wavelength λ_{th} and the emission frequency ν_{th}), travels towards the target surface located at the external cavity length L_{ext} before being backscattered and re-injected into the laser cavity. It should be highlighted that the incident wave at ν_{th}, propagation time is $\tau_{\text{ext}}/2$. The reflected wave from the target will take a propagation time $\tau_{\text{ext}}/2$ before entering the laser intracavity.

Based on the Land and Kobayashi model for SMI Doppler shifted presented by Zakian *et al.* [84] and Nicolić *et al.* [85], once the emission frequency from the laser interferes with the Doppler frequency and backscatters and recombines with the initial emission frequency inside the laser. Then, the phase stimulus of the excess phase equation in (2.74) is then transformed as,

$$\varphi_{\text{s}}(t) = \Big(\omega_{\text{s}} + \frac{\Omega_{\text{D}}}{2}\Big)\tau_{\text{ext}} - \Omega_{\text{D}}(t), \tag{4.2}$$

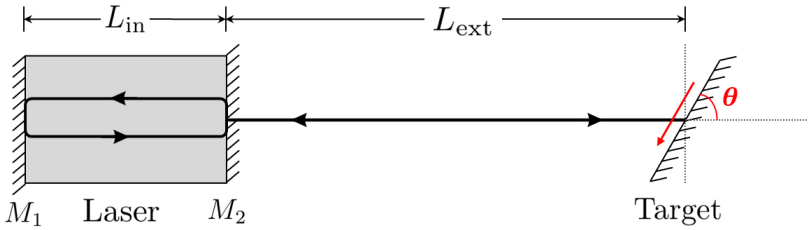

Figure 4.1: The principle of self-mixing interferometer for velocimetry application with a translating target. Solid line with arrows indicates the beam light direction both in the internal and external cavity.

where $\Omega_{\text{D}} = 2\pi f_{\text{D}}$ is the angular frequency produced by the Doppler effect, and f_{D} is the Doppler frequency which is expressed as [11, 86],

$$f_{\text{D}} = n_{\text{ext}} \frac{2\upsilon \cos\theta}{\lambda_{\text{th}}}, \tag{4.3}$$

where υ is the speed of the target and θ is the angle between the laser beam axis and the target velocity vector.

Using the laser diode parameters in Table 3.1, the SMI signal output power is plotted in Figure 4.2 through the expression (2.77) with a feedback parameter $C = 0.7$ for the excess phase equation and given physical parameters such as the speed of the rotating disc $\upsilon = 2$ mm/s, the angle between the laser beam axis and the target velocity $\theta = 30°$, the external cavity length $L_{\text{ext}} = 1$ m and the external refractive index $n_{\text{ext}} = 1$. Figure 4.2 displays the simulation results of the SMI optical output power in the time and frequency domain.

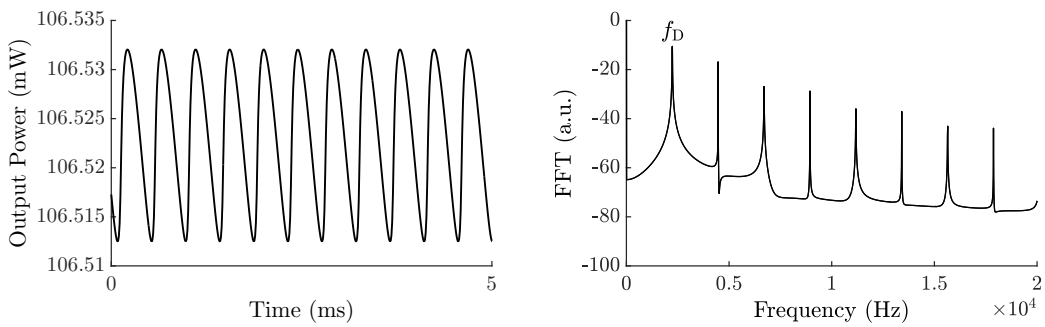

(a) (b)

Figure 4.2: Simulation self-mixing velocimetry power under the optical feedback $C = 0.7$: (a) In the time domain. (b) In the frequency domain.

The signal spectral analysis can be applied to determine the Doppler frequency as

shown in Figure 4.2(b). The strongest peak in the frequency domain corresponds to the Doppler frequency as calculated through the expression (4.3).

Any fluctuation in the feedback parameter C in the system causes the changes in signal amplitude and appearance, and this can be observed in Figure 4.3. The shape of the fringes is almost sinusoidal when the feedback parameter C is very small and translates to sawtooth-like waveform the feedback parameter C is greater than one. This shape of sawtooth-like in the observed output signal can be explained with transitions of the stable solutions in the behaviour of $\cos\varphi_{\mathrm{FB}}$ exactly as in the case of the laser modulation or vibration depicted in chapters 2 and 3.

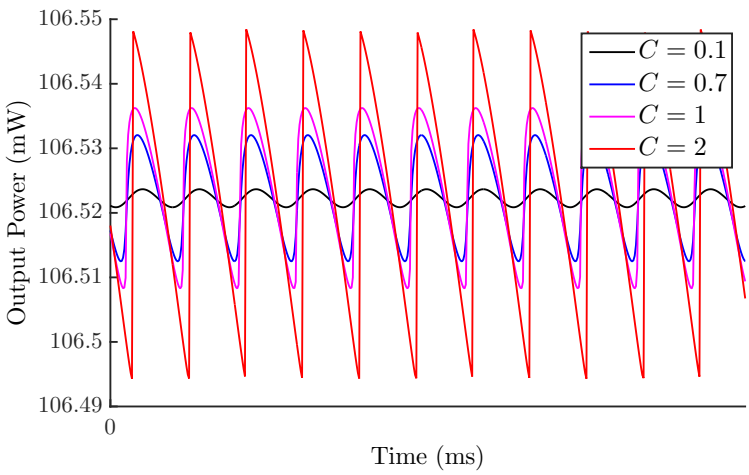

Figure 4.3: Simulation self-mixing velocimetry power under different optical feedback parameter C.

As the distance between the laser and the target is fixed, then there is only Doppler frequency that drives changes in the SMI output signal. As the target velocity moves in one direction either its projection is seen as is positive or negative, the phase stimulus will change also in one direction either increasing or decreasing. As the interferometric fringe disappearance phenomenon explained in the previous chapters occurs also in this situation but the fringes will be lost only at the beginning of the displacement when the laser diode is operated under the moderate/strong optical feedback regime. Consequently, this phenomenon is hard to be observed in actual velocity sensing schemes where the Doppler effect induces a huge amount of fringes.

As we know that the frequency-shifted in the optical feedback is produced by the Doppler shift in the incident laser frequency; then the rate equation for the electric field

in Eq. (2.63) is modified as [84],

$$\frac{dE(t)}{dt} = \Big(j(\omega - \omega_{\mathrm{th}}) + \frac{1}{2}\big(\Gamma G - \frac{1}{\tau_{\mathrm{ph}}}\big)\Big)E(t) + \frac{\kappa_{\mathrm{ext}}}{\tau_{\mathrm{in}}}E(t-\tau_{\mathrm{ext}})\exp(-j\varphi_{\mathrm{D1}}(t)), \tag{4.4}$$

where

$$\varphi_{\mathrm{D1}}(t) = \big(\omega_{\mathrm{th}} + \pi f_{\mathrm{D}}\big)\tau_{\mathrm{ext}} - 2\pi f_{\mathrm{D}}(t). \tag{4.5}$$

Therefore, this leads to the changes in rate equations for the carrier number, photon number and the phase in Eq. (2.64), and it can be written as,

$$\begin{cases} \dfrac{dS(t)}{dt} = \Big(\Gamma G - \dfrac{1}{\tau_{\mathrm{ph}}}\Big)S(t) + \dfrac{2\kappa_{\mathrm{ext}}}{\tau_{\mathrm{in}}}\sqrt{S(t)S(t-\tau_{\mathrm{ext}})}\cos\varphi_{\mathrm{D2}} \\ \dfrac{d\varphi(t)}{dt} = \dfrac{1}{2}\Big(\Gamma G - \dfrac{1}{\tau_{\mathrm{ph}}}\Big) - \dfrac{\kappa_{\mathrm{ext}}}{\tau_{\mathrm{in}}}\sqrt{S(t-\tau_{\mathrm{ext}})/S(t)}\sin\varphi_{\mathrm{D2}} \\ \dfrac{dN(t)}{dt} = \dfrac{\eta_{\mathrm{i}}I}{qV} - \dfrac{N(t)}{\tau_{\mathrm{n}}} - GS(t), \end{cases} \tag{4.6}$$

where

$$\varphi_{\mathrm{D2}} = \Big(\omega_{\mathrm{th}} + \pi f_{\mathrm{D}}\Big)\tau_{\mathrm{ext}} - 2\pi f_{\mathrm{D}}t + \varphi(t) - \varphi(t-\tau_{\mathrm{ext}}). \tag{4.7}$$

By applying the same simulation parameters from the case in Figure 4.2, the SMI output power signal has the interferometric fringe's form in the time domain and results in the same Doppler beat frequency in the frequency domain as the simulation result with the excess phase equation.

The rate equations for Doppler-shifted optical feedback in (4.6) presents with a single-frequency component. However, optical feedback from fluid and rough surfaces in motion consists of multiple frequency-shifted components spectrale close to one another [85]. So these rate equations have been modified by Nikolić *et al.* by adding the independently and uniformly distribution phase over 2π radian, and it can be written as,

$$\begin{cases} \dfrac{dS(t)}{dt} = \Big(\Gamma G - \dfrac{1}{\tau_{\mathrm{ph}}}\Big)S(t) + \dfrac{2\kappa_{\mathrm{ext}}}{\tau_{\mathrm{in}}}\sqrt{S(t)S(t-\tau_{\mathrm{ext}})}\gamma\sum\limits_{k=1}^{k}A_k\cos\varphi_{\mathrm{D3},k} \\ \dfrac{d\varphi(t)}{dt} = \dfrac{1}{2}\Big(\Gamma G - \dfrac{1}{\tau_{\mathrm{ph}}}\Big) - \dfrac{\kappa_{\mathrm{ext}}}{\tau_{\mathrm{in}}}\sqrt{S(t-\tau_{\mathrm{ext}})/S(t)}\gamma\sum\limits_{k=1}^{k}A_k\sin\varphi_{\mathrm{D3},k} \\ \dfrac{dN(t)}{dt} = \dfrac{\eta_{\mathrm{i}}I}{qV} - \dfrac{N(t)}{\tau_{\mathrm{n}}} - GS(t), \end{cases} \tag{4.8}$$

where

$$\varphi_{\mathrm{D3},k} = \Big(\omega_{\mathrm{th}} + \pi f_{\mathrm{D},k}\Big)\tau_{\mathrm{ext}} - 2\pi f_{\mathrm{D},k}t + \varphi(t) - \varphi(t-\tau_{\mathrm{ext}}) + \vartheta_k, \tag{4.9}$$

where ϑ_k is an independently and uniformly distributed phase over 2π radian, $\vartheta_k \sim U(0, 2\pi)$, that is added to each $\varphi_{\mathrm{D3},k}$. γ is the scaling factor and it is necessary to ensure that the optical feedback power level has a root-mean-square value equal to that of a

single sinusoid, regardless of the number K of frequency components. Figure 4.4 shows the simulation results in the time and frequency domain of the SMI frequency shift distribution from the rate equations in (4.8) under the feedback parameter $C = 0.7$ and the Doppler frequency ranging between 25 kHz and 26 kHz.

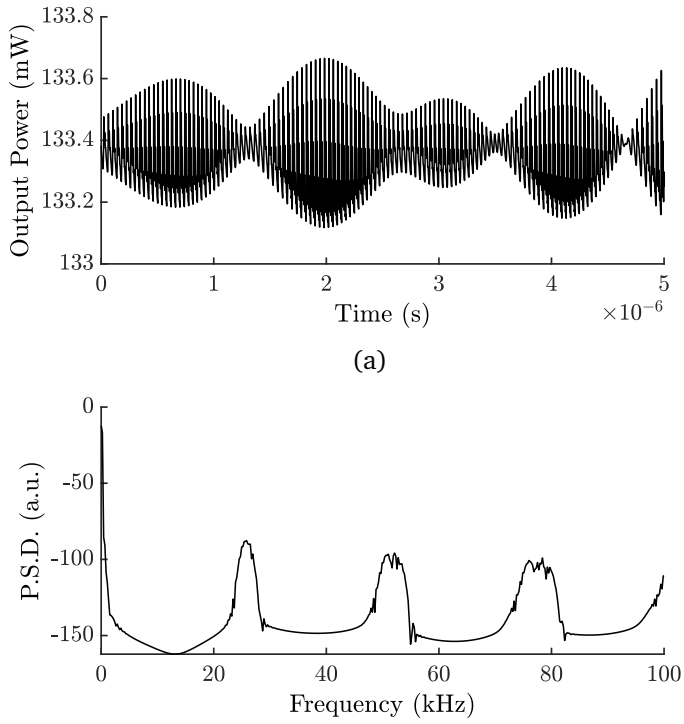

Figure 4.4: Simulation self-mixing power resulting from the Doppler shift distribution based on the rate equations. (a) In the time domain. (b) PSD of the self-mixing power variations in (a).

In reality, the uniform amplitude of SMI output signals in the time domain is caused by the Speckle effect that normally resulting from the reflection of coherent light at the rough surface with a complicated structure, such as a piece of paper, white paint, a display screen, or a metallic surface. We will validate this effect by using a piece of white paper in our experiment in the next section.

4.1.2 | Experiment and validation

The experimental setup is displayed in Figure 4.5. It consists of a DFB laser diode (L1550P5DFB) lasing at 1550 nm with a package−included a monitoring photodiode is associated to a collimating lens with focuses the laser beam onto the rotating target

surface which is covered by a white paper. An angle of $80°$ between the laser beam axis and the target velocity vector is set. The laser diode is operated with a bias injection current of 20 mA (about 3.34 times its threshold current of 6 mA). The photodetected signal from the photodiode is then converted to a voltage by transimpedence amplifier. The distance between the laser and the target is 1 m and the target spins with DC motor in the clockwise direction.

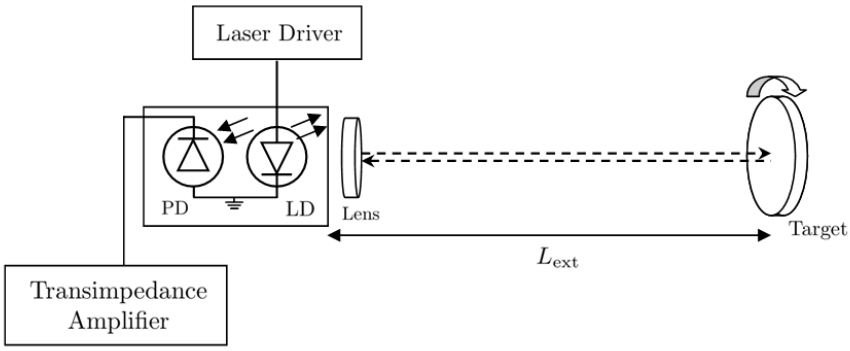

Figure 4.5: Experimental setup for self-mixing Doppler shift with the rotating target.

Figure 4.6 displays the experimental results of the SMI frequency shift distribution which shows an agreement to the numerical simulation shown in Figure 4.4. The amplitude of the signal varies over time, and it can be explained that the white paper surface is rough. It is interesting to notice that not only the speckle effect has effects on the amplitude of SMI signal but it also has been shown that the numerical aperture (NA) of the focusing lens allows different intensities of light from different angles to be mixed with the original laser light [87].

Next experiment, we replace the white paper target surface with the microprism reflective tape at the same external cavity length between the laser and the target, the speed of rotating and the angle between the laser beam axis and the target velocity vector. The result in Figure 4.7(a) shows the SMI signal with a series of interferometric fringes which greatly varies over time. However, it is interesting to mention that the reflective tape reflection coefficient fluctuates very quickly compared to the white paper. Any variation in the external reflection coefficient modulates the feedback parameter C which then varies not only the amplitude signal but also the beat frequency at the SMI output signal. The rapid changes in the reflection coefficient from the microprism tape surface results in no detected peak of Doppler frequency in the PSD frequency domain displayed in Figure 4.7(b).

The similar experimental result was also done in [88] where the external physical

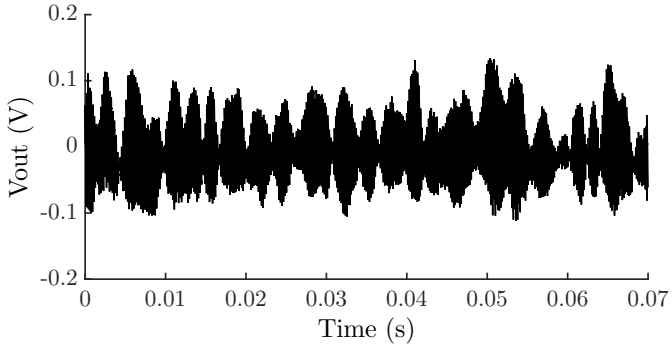

(a)

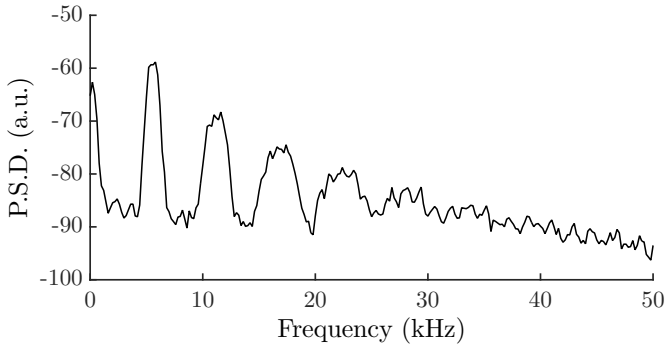

(b)

Figure 4.6: Experimental results of Doppler shift with the white paper surface. (a) The self-mixing signal in the time domain. (b) PSD of of the self-mixing power variations obtained from (a).

length of the target changes constantly along the laser beam axis instead of a stationary target. Their explanation describes clearly that the speckle effect results in variation in the feedback parameter C. Other experimental results about the speckle effect can also be found in [89, 90].

By default, the spectral analysis of the SMI signal does not provide information on the direction of the velocity vector direction. However, as will be discussed in the next section, the direction can be obtained when modulating the laser wavelength through its injection current.

4.2 | Measurement of the target distance and velocity

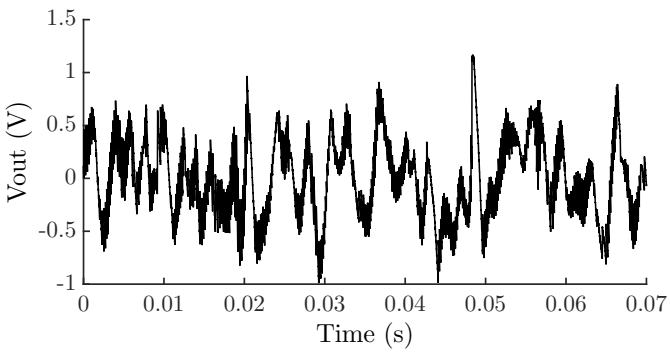

(a)

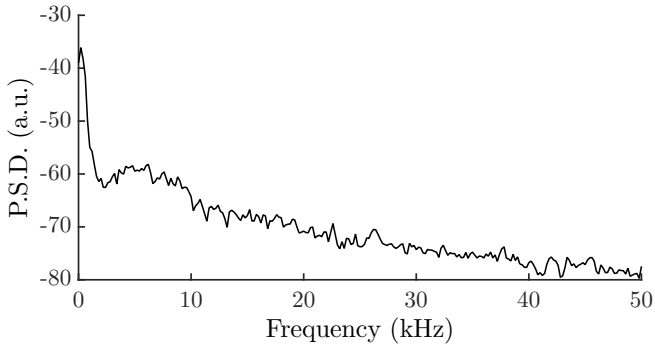

(b)

Figure 4.7: Experimental results of Doppler shift with the microprism reflective tape surface. (a) The self-mixing signal in the time domain. (b) PSD of of the self-mixing power variations obtained from (a).

4.2.1 | Modelling

If the laser emission frequency is modulated to produce a periodic triangle frequency sweep by means of modulating the laser injection current, an estimation of the external cavity length and of the target velocity are possible calculated at the same time. It should be noticed that the increasing linear sweep of lasing frequencies is seen as a linear extension of the external cavity, while the decreasing sweep is seen as a reduction of the external cavity.

As we described in Chapter 3, modulating the laser injection current which then modulates the laser emission frequency in triangle waveform, the SMI output power results in a triangle waveform with low contrast ripples on each ramp of modulation by the interferometric fringe. Those fringes correspond to the longitudinal modes in the external cavity whose frequency spacing are proportional to the distance between the laser and the target.

Combining the two physical stimuli, the Doppler shift for a stationary target in Eq. (4.2) and the triangle laser emission frequency at the free-running state in Eq. (3.1), into a single phase stimulus that can be expressed in function of time as,

$$\varphi_{\mathrm{s}}(t) = 2\pi\tau_{\mathrm{ext}}\Big(\nu_{\mathrm{th}} + \Delta\nu_{\mathrm{th}}(t) + \frac{f_{\mathrm{D}}}{2}\Big) - \Omega_{\mathrm{D}}(t). \tag{4.10}$$

The SMI output power can thus be computed by applying the modulated phase stimulus in Eq. (4.10) into the excess phase equation in Eq. (2.74) to solve the phase response which is related to the SMI output power in Eq. (2.77). Besides the excess phase equation model, this application of the Doppler shift from a stationary target with triangular laser emission frequency sweeping can also be modelled with the rate equation. It is expressed as,

$$\begin{cases} \dfrac{dS(t)}{dt} = \Big(\Gamma G - \dfrac{1}{\tau_{\mathrm{ph}}}\Big)S(t) + \dfrac{2\kappa_{\mathrm{ext}}}{\tau_{\mathrm{in}}}\sqrt{S(t)S(t-\tau_{\mathrm{ext}})}\cos\varphi_{\mathrm{D4}} \\ \dfrac{d\varphi(t)}{dt} = \dfrac{1}{2}\Big(\Gamma G - \dfrac{1}{\tau_{\mathrm{ph}}}\Big) - \dfrac{\kappa_{\mathrm{ext}}}{\tau_{\mathrm{in}}}\sqrt{S(t-\tau_{\mathrm{ext}})/S(t)}\sin\varphi_{\mathrm{D4}} \\ \dfrac{dN(t)}{dt} = \dfrac{\eta_{\mathrm{i}} I}{qV} - \dfrac{N(t)}{\tau_{\mathrm{n}}} - GS(t), \end{cases} \tag{4.11}$$

where

$$\varphi_{\mathrm{D4}} = \Big(\omega_{\mathrm{th}}(t-\tau_{\mathrm{ext}}) + \frac{\Omega_{\mathrm{D}}}{2}\Big)\tau_{\mathrm{ext}} - \Omega_{\mathrm{D}}t + \varphi(t) - \varphi(t-\tau_{\mathrm{ext}}) \tag{4.12}$$

The SMI output power can thus be calculated with the rate equation using a fourth order Runge-Kutta algorithm, and the same procedure described in the previous absolute distance chapter. The Doppler shift leads to an asymmetry in the number of interferometric fringes observed in each half of the triangle waveform that can be used to discriminate the displacement.

It is important to highlight that using a rotating disk as the target, the distance between the laser and the target is stationary, then the distance beat frequency f_{d} remains constant. The Doppler beat frequency f_{D} is proportional to the target velocity and the angle between the laser beam axis and the target velocity vector. Then, two cases must be considered—when the distance beat frequency is superior to the Doppler frequency and when the distance beat frequency is inferior to the Doppler frequency.

4.2.1.1 | When $|f_{\mathrm{d}}| > |f_{\mathrm{D}}|$

For the simulation in Figure 3.1, at the external distance of 1 m with a given FM coefficient of -3 GHz/mA, and the laser diode is modulated with an amplitude of 0.5 mA peak-to-peak in triangle waveform at 50 Hz frequency modulation, the distance beat

frequency is 1 kHz with twenty interferometric fringes for a complete period of triangle modulation waveform in the SMI output power. Then, with a velocity of the target 0.35 mm/s and the angle $30°$, the Doppler frequency results in 391.10 Hz.

The number of fringe in each half of the triangle waveform strongly depends on the Doppler shift frequency and the direction of the target. The different number of interferometric fringe in the SMI signal results from the asymmetrical of the phase stimulus as shown in Figure 4.8.

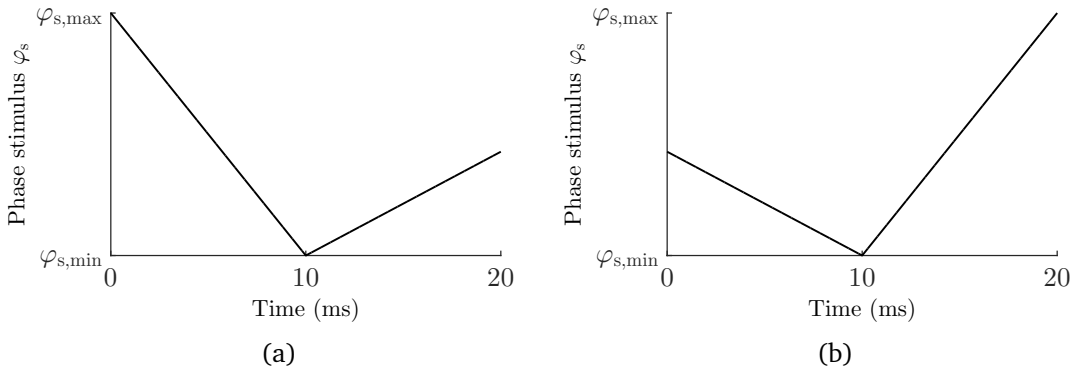

Figure 4.8: Simulation laser phase stimulus for the rotating target. (a) In the clockwise direction with the speed υ = +0.35 mm/s. (b) In the anticlockwise direction with the speed υ = -0.35 mm/s.

In Figure 4.8(a), when the Doppler frequency is positive (rotating clockwise direction), the decreasing phase stimulus sweeping in the first half of the triangle waveform is longer than the increasing phase sweeping in the other half of the triangle waveform. On the other hand, when the Doppler frequency is negative (rotating anticlockwise direction), the decreasing phase stimulus sweeping in the first half of the triangle waveform is shorter than the increasing one in the other half of the triangle waveform as shown in Figure 4.8(b). Both cases of rotating directions in Figures 4.8(a) and (b) result in a different number of interferometric fringes in the SMI output signal as shown in Figures 4.9(a) and (b), respectively.

The classical method to calculate the external cavity length and the target velocity is by counting the integer number of the observed interferometric fringes in the SMI output signal for a full cycle of triangle waveform. Assuming that the number of observed fringes for the first and second half period of the triangle waveform are $N_{\mathrm{f},1}$ and $N_{\mathrm{f},2}$, respectively, the target velocity and distance can be determined as [4],

$$L_{\mathrm{ext}} = \frac{c}{4\Delta I \Omega n_{\mathrm{ext}}}\big(N_{\mathrm{f},1} + N_{\mathrm{f},2}\big), \tag{4.13}$$

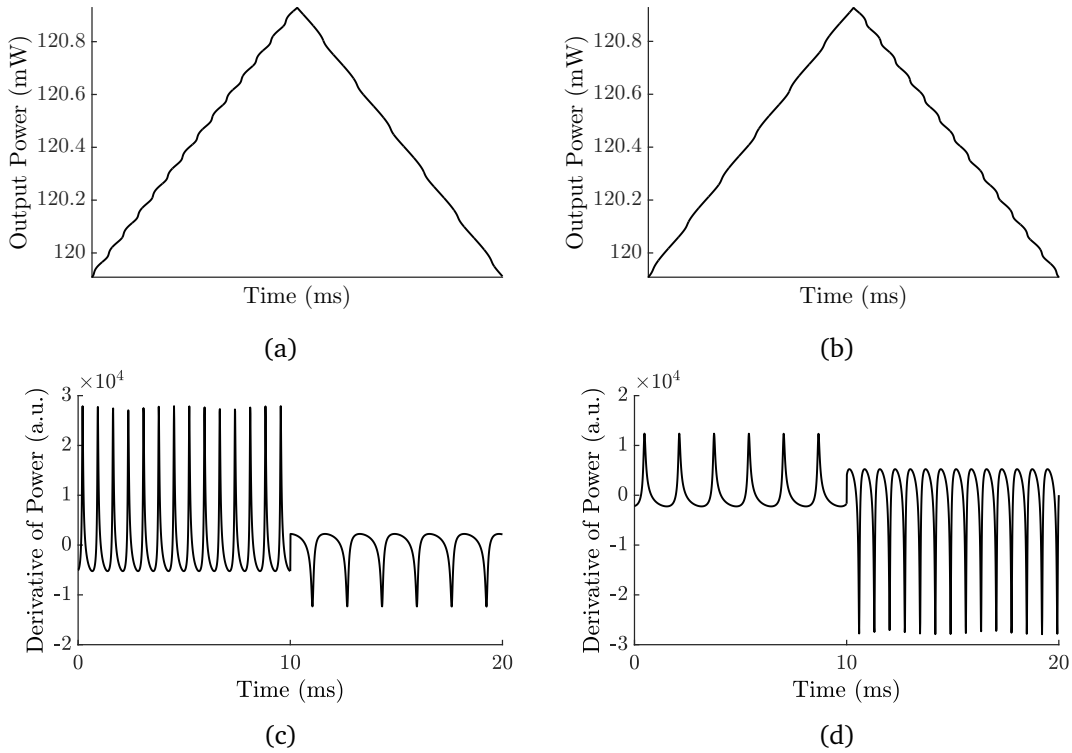

Figure 4.9: Simulation self-mixing power resulting from modulating the phase stimulus in the triangle waveform under the feedback parameter $C = 0.7$ in different velocity directions. (a) In the clockwise direction with the speed υ = +0.35 mm/s. (b) In the anticlockwise direction with the speed υ = -0.35 mm/s.

$$\upsilon = \frac{\lambda_{\mathrm{th}} f_{\mathrm{m}}}{2\cos\theta}\left(N_{\mathrm{f},1} - N_{\mathrm{f},2}\right). \tag{4.14}$$

As seen in Eq. (4.14), the direction of the target (clockwise or anticlockwise in the case of the rotating target and linear extension or contraction of the external cavity) can be discriminated as the number of observed fringes is not equal between each half of the triangle waveform. It is interesting to notice that the sum of observed interferometric fringes for a full cycle of the triangle waveform always equals the number of appeared fringes in a triangle period in SMI absolute distance measurement.

As discussed in Chapter 3, the alternative methods can also be used to determine the external cavity and the target velocity in this case. Assuming that the average spacing times between fringes for the first and second half of the triangle waveform are $t_{\mathrm{b},1}$ and $t_{\mathrm{b},2}$, respectively, then the corresponding average beat frequencies are $f_{\mathrm{b},1}$ and $f_{\mathrm{b},2}$. Applying the FFT to the SMI output power, the first strongest peak is ignored due to the frequency modulation of the triangle waveform; then the next two strongest peaks

corresponds to the average beat frequency of interferometric fringes during the linear increasing and decreasing output power sweep of the SMI signal. So, the distance beat frequency and the Doppler beat frequency can be defined as **??**,

$$f_{\mathrm{d}} = \frac{f_{\mathrm{b},1} + f_{\mathrm{b},2}}{2}, \tag{4.15}$$

$$f_{\mathrm{D}} = \frac{f_{\mathrm{b},1} - f_{\mathrm{b},2}}{2}, \tag{4.16}$$

Thus the external cavity of physical length and the target velocity can be rewritten as,

$$L_{\mathrm{ext}} = \frac{c}{8\Delta I \Omega f_{\mathrm{m}}}\left(f_{\mathrm{b},1} + f_{\mathrm{b},2}\right), \tag{4.17}$$

$$\upsilon = \frac{\lambda_{\mathrm{th}}}{4\cos\theta}\left(f_{\mathrm{b},1} - f_{\mathrm{b},2}\right). \tag{4.18}$$

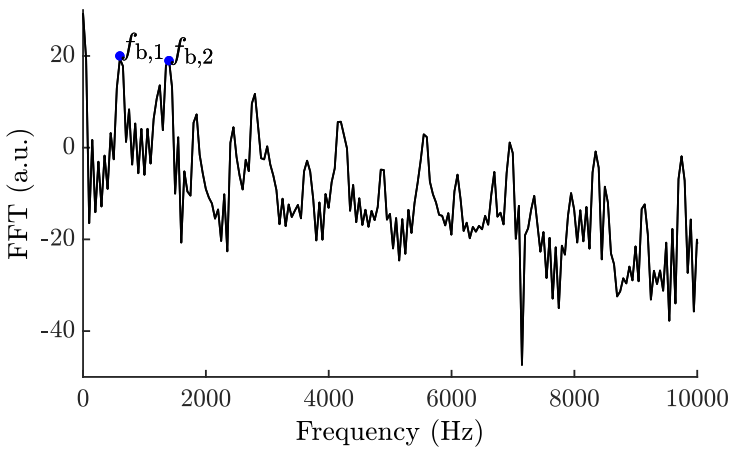

Figure 4.10: FFT of the simulated self-mixing velocimetry output power resulting from the triangular frequency sweeping.

Figure 4.10 shows the plot of FFT for the SMI output power which results in 600 Hz and 1400 Hz for the first and second strongest peak. It should be highlighted that the sign of the Doppler beat frequency may not be discriminated when applying the FFT to a full cycle period of triangle modulation of the SMI signal. It cannot tell that the first or second peak corresponds to the first or second beat frequency in the output power. However, if we apply the FFT to each semi-period of triangle modulation of SMI signal by knowing that $f_{\mathrm{b},1}$ is the beat frequency when the injection current increases and $f_{\mathrm{b},2}$ is the beat frequency when the injection current decreases, the direction of the moving target is easy to determine.

4.2.1.2 | When $|f_\mathrm{d}| < |f_\mathrm{D}|$

With the given target velocity of 2 mm/s and the angle between the laser beam axis and the target velocity of $30°$, the Doppler frequency would result in 2.23 kHz. With the same simulation parameters as in the previous section and the 2.23 kHz of Doppler frequency, the phase stimulus in (4.10) can be plotted for both cases as shown in Figure 4.11.

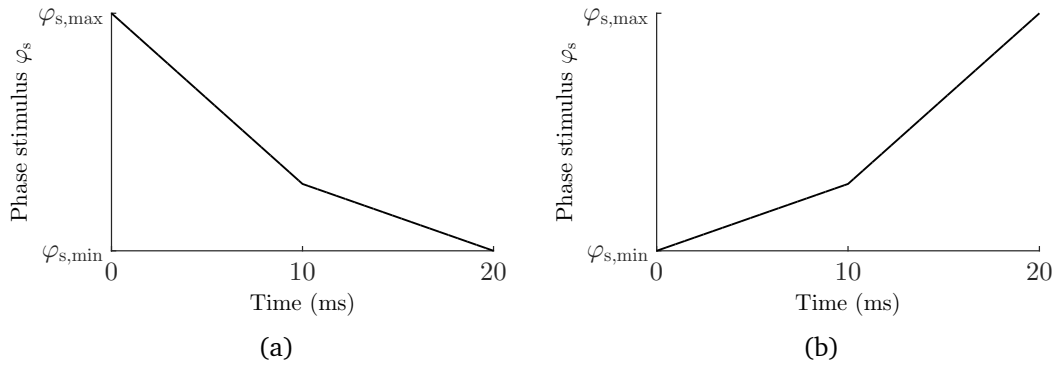

Figure 4.11: Simulation laser phase stimulus for the rotating target. (a) In the clockwise direction with the speed v = +2 mm/s. (b) In the anticlockwise direction with the speed v = -2 mm/s.

As seen in Figure 4.11(a) with a positive Doppler shift when the bias injection current increases, the phase stimulus linearly decreases. Then when the injection current decreases, the phase stimulus does not inversely increase, but instead continuously decreases until the end of the triangle modulation. However, when the Doppler shift is negative, the phase stimulus keeps increasing for a full cycle of triangle modulation as shown in Figure 4.11(b). In this case, the length between the $\varphi_{\mathrm{s,min}}$ and $\varphi_{\mathrm{s,max}}$ depends on the value of Doppler frequency which is then affected to the number of interferometric fringes in the optical output power. The derivative of the SMI output power will result in a series of interferometric fringes which are all positive or negative depending on the Doppler shift sign and thus on the translation direction as shown in Figure 4.12.

The external cavity length and the target velocity can be determined by using the observed fringes counting method as [4],

$$L_\mathrm{ext} = \frac{c}{4\Delta I \Omega n_\mathrm{ext}} \big(|N_\mathrm{f,1} - N_\mathrm{f,2}|\big), \tag{4.19}$$

$$v = \frac{\lambda_\mathrm{th} f_\mathrm{m}}{2\cos\theta} \big(N_\mathrm{f,1} + N_\mathrm{f,2}\big). \tag{4.20}$$

Furthermore, the external cavity of physical length and the target velocity can also be determined with the frequency domain method by applying the FFT as shown in

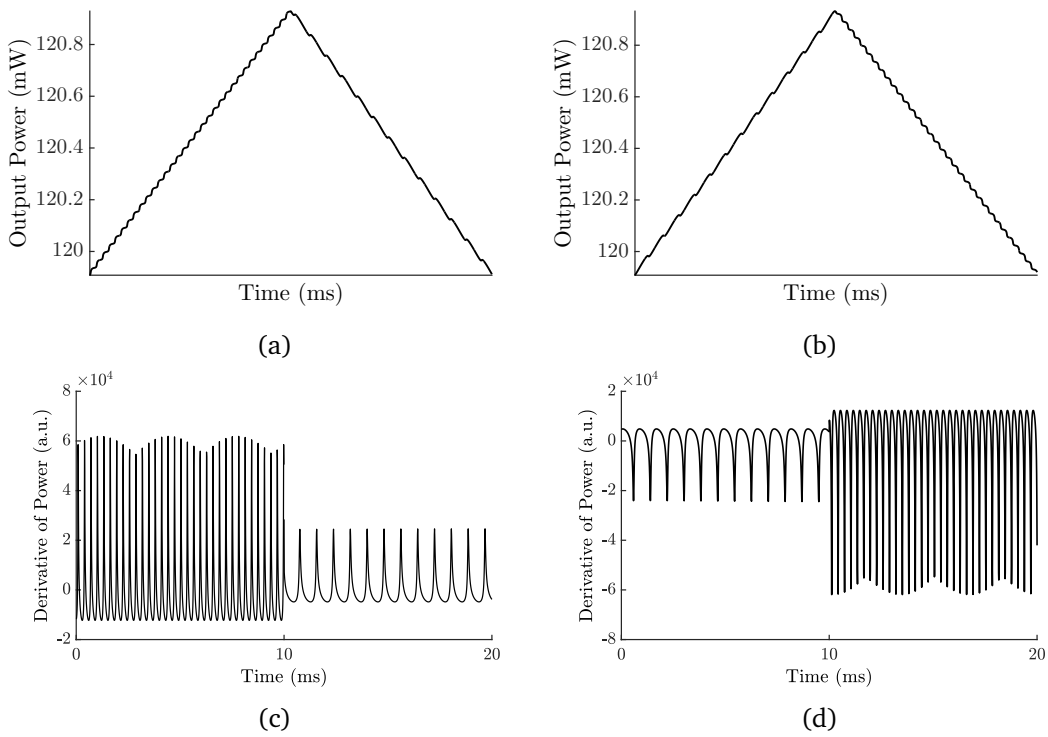

Figure 4.12: Simulation self-mixing power resulting from modulating the phase stimulus in the triangle waveform under the feedback parameter $C = 0.7$ in different velocity directions. (a) In the clockwise direction with the speed v = +2 mm/s. (b) In the anticlockwise direction with the speed v = -2 mm/s.

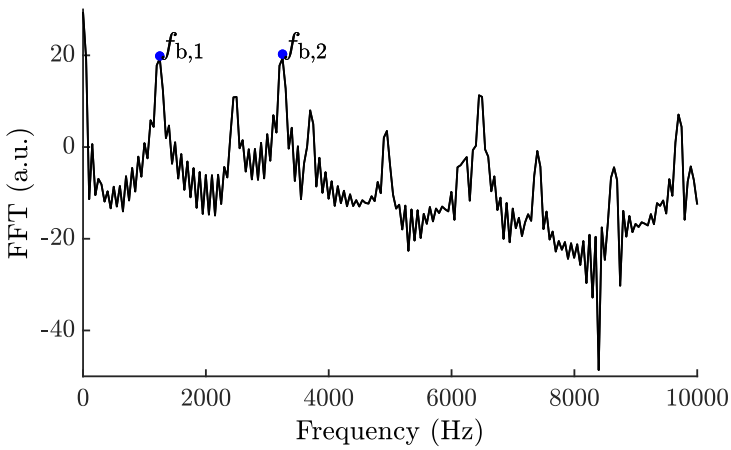

Figure 4.13: FFT of the simulated self-mixing velocimetry output power resulting from the triangular frequency sweeping.

Figure 4.13. The first two strongest of the average beat frequency peaks in the FFT are used to determine the distance and Doppler beat frequency; those can be expressed as [4],

$$f_{\mathrm{d}} = \frac{|f_{\mathrm{b},1} - f_{\mathrm{b},2}|}{2}, \tag{4.21}$$

$$f_{\mathrm{D}} = \frac{f_{\mathrm{b},2} + f_{\mathrm{b},1}}{2}. \tag{4.22}$$

Then, the external cavity length and the target velocity can be calculated as,

$$L_{\mathrm{ext}} = \frac{c}{8\Delta I \Omega f_{\mathrm{m}}}\big(|f_{\mathrm{b},1} - f_{\mathrm{b},2}|\big), \tag{4.23}$$

$$v = \frac{\lambda_{\mathrm{th}}}{4\cos\theta}\big(f_{\mathrm{b},1} + f_{\mathrm{b},2}\big). \tag{4.24}$$

The next section, we will see the behaviour of SMI signal in different optical feedback regimes.

4.2.2 | Phase behaviour

The SMI output powers described in the previous section were simulated under the weak feedback regime. However, when the laser diode is operated under moderate/strong feedback, interferometric fringe disappearance phenomenon appears in the SMI output signal. So, in this section, we will present the SMI phase behaviour in this application for both cases discussed in the previous section.

4.2.2.1 | When $|f_{\mathrm{d}}| > |f_{\mathrm{D}}|$

As we have discussed before in Chapters 2 and 3, the phase response φ_{FB} in the excess phase equation mainly depends on the phase stimulus φ_{s} and the feedback parameter C as the linewidth enhancement factor α is usually modelled as a constant. It should be noted that the phase stimulus is fixed by the emission frequency, the external cavity length and the Doppler frequency. Using the simulation in Section 4.2, we vary the feedback parameter C to see the evolution of the SMI phase behaviour in different optical feedback regimes.

The variation between the increasing and decreasing portions of the phase stimulus for each half of the triangle waveform is not symmetrical because of the presence of Doppler shift. The portion of the phase stimulus for the first half of the triangle waveform varies more than the other half portion. To ease further demonstration, the laser injection current in this section is modulated with two periods of triangle waveforms.

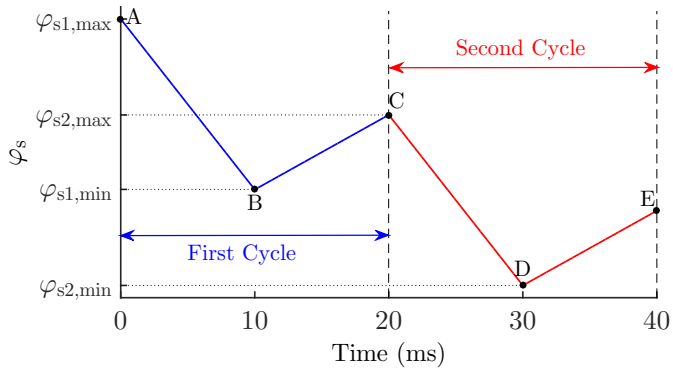

(a) Plot phase stimulus in function of time with two cycles period of triangle modulation.

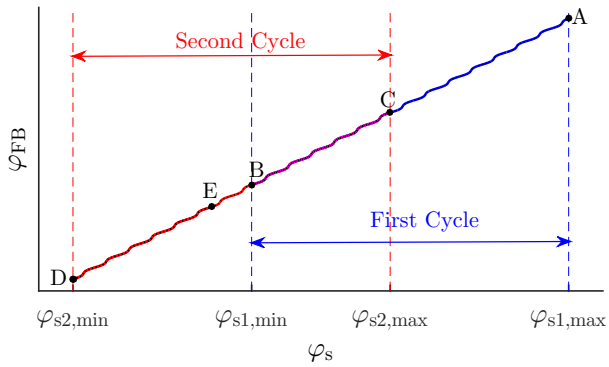

(b) Plot the dwelling path solutions of phase stimulus and phase response.

Figure 4.14: (a) Plot the triangle laser phase stimulus sweeping in the function of time when the distance beat frequency is superior to the Doppler frequency. (b) The lasing mode in phase behaviour under the optical feedback parameter $C = 0.7$.

The modulation of the injection current results in the change of the phase stimulus as shown in Figure 4.14(a). The first cycle of modulation is indicated in the thick blue solid lines while the second cycle of modulation is indicated in the red one.

Figure 4.14(b) displayed the SMI phase behaviour with a feedback parameter $C = 0.7$. The phase stimulus for the first half period of modulation results in 14 segments of the curve $\mathcal{C}$ while for the other half period 6 segments of the curve $\mathcal{C}$ are generated. Under the weak feedback regime, the lasing mode will start dwelling the stable solution from point A (the maximum of the phase stimulus $\varphi_{s1,max}$), then goes down to point B (the minimum of the phase stimulus $\varphi_{s1,min}$), crosses 14 segments of the curve $\mathcal{C}$ without any mode hopping. Unlike the absolute distance application, when the laser injection current decreases for another half period, the lasing mode does not turn back with the

same solution path to point A, but it keeps dwelling just 6 segments of the curve $\mathcal{C}$ and stops at point C. For a new cycle of modulation, the lasing mode does not jump back to point A but starts dwelling the stable solution from point C where it has stopped from the previous modulation cycle (the maximum of phase stimulus for the second cycle, $\varphi_{\mathrm{s2,max}}$). From point C, the lasing mode will dwell the stable solution to point D (the minimum of phase stimulus for the second cycle, $\varphi_{\mathrm{s2,min}}$) with 14 curves $\mathcal{C}$ and backs to point E for another 6 curves $\mathcal{C}$ for a new cycle of triangle modulation.

When the laser diode is operated under the moderate/strong feedback, anti-mode or unstable solution occurs in the lasing mode, and the interferometric fringe disappearance phenomenon will also happen. In the next simulation, we will set the parameter C to 31.26. The interferometric fringes appear only in the first half of the triangle waveform in the SMI output power.

As seen in Figure 4.15(a), only linear decreasing portion of the phase stimulus still displays the transitions of the stable solution in the lasing mode. When the phase stimulus decreases for the first half of the triangle waveform, the lasing mode dwells the stable solution from point A, goes down to point B with 10 transitions between curve $\mathcal{C}$ which result in 10 interferometric fringes at the output power indicated in solid blue lines. On the other hand, when the phase stimulus increases for another half of the triangle waveform, there is no transition of the stable solution; but lasing mode just dwells the stable solution on the same curve from point B to point C.

Later, for a new cycle of the triangle modulation, the lasing mode will dwell the stable solution starting from point C where it has stopped from the previous modulation cycle to point D with another 7 modes hopping and goes to point E without any mode hopping indicated in thick red solid lines. Then, the SMI output power for these two modulation cycles can be plotted with the rate equation under the feedback level $C = 31.26$ shown in Figure 4.15(b). We can see clearly that there is no interferometric fringe when the phase stimulus linear increases over time.

With the missing fringe occurs in the SMI output power, the calculation error of the external cavity length and the target velocity is very high while using the counting fringes method. The determination of those parameters should be performed with the average time spacing or FFT method.

4.2.2.2 | When $|f_{\mathrm{d}}| < |f_{\mathrm{D}}|$

When the Doppler beat frequency is superior to the distance beat frequency, the modulated phase stimulus's form is no more a triangle waveform; it will keep either increasing or decreasing slope for a complete modulation period. For the positive Doppler frequency,

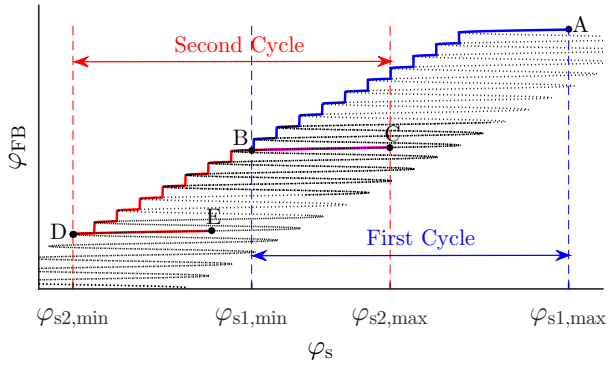

(a) Plot the dwelling path solutions of phase stimulus and phase response.

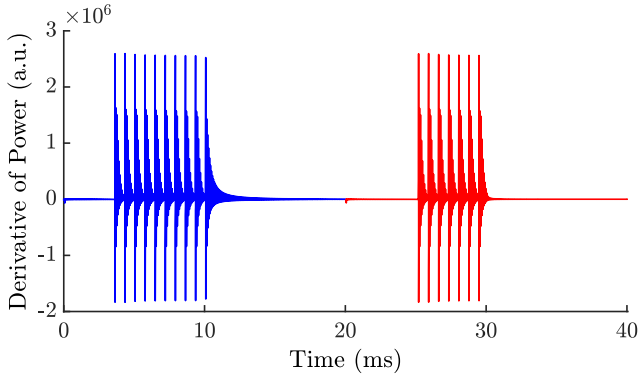

(b) Plot derivative of the output power in resulting from the dwelling solution path in (a).

Figure 4.15: (a) Plot the lasing mode behaviour resulting from the triangular phase stimulus sweeping under the feedback parameter $C = 31.26$. (b) Simulation the self-mixing power resulting from dwelling of the lasing mode in (a).

the phase stimulus is decreasing over time as shown in Figure 4.16(a); on the contrary, the phase stimulus is increasing over time when the Doppler beat frequency is negative. These circumstances give the extension of the segment of the curves $\mathcal{C}$ because of the sweeping portion of the phase stimulus. The number of extension curves mainly depends on the Doppler beat frequency while considering that the distance beat frequency is constant.

Under the weak optical feedback regime, the lasing mode seeks for the stable solution commencing from point A, then passes by point B and C for the first cycle of the triangle modulation indicated in the thick blue solid line. Later, the lasing mode will continue to decrease from point C to D, then E for the second cycle of modulation indicated in thick red solid line as shown in Figure 4.16(b). With this SMI phase behaviour of the stable

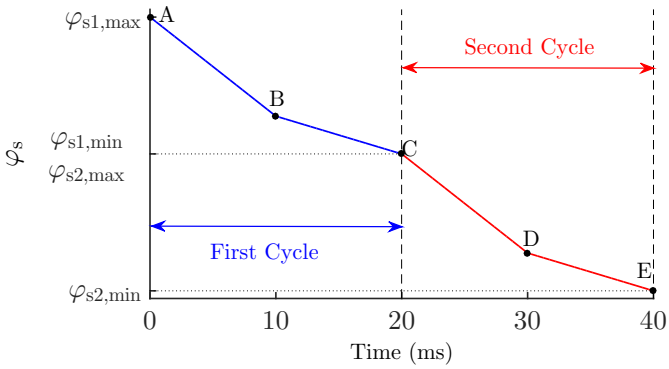

(a) Plot phase stimulus in function of time with two cycles period of triangle modulation.

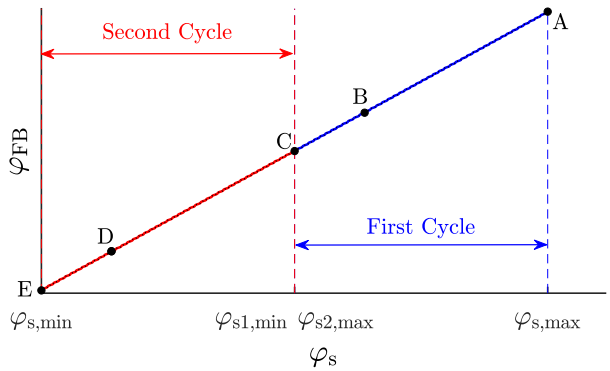

(b) Plot the dwelling laser path solutions of phase stimulus and phase response.

Figure 4.16: (a) Plot the triangle laser phase stimulus sweeping in the function of time when the distance beat frequency is inferior to the Doppler frequency. (b) The lasing mode in phase behaviour under the optical feedback parameter $C = 0.7$.

mode dwelling under the feedback parameter $C = 0.7$, the derivative of the output power would result in a series of interferometric fringes where all of the spikes observed are negative shown in Figure 4.12(b).

However, when the laser diode performs under the moderate/strong optical feedback regime, the stable solution's line of each curve are getting wider where the interferometric fringe disappearance phenomenon would occur only at the beginning in the SMI output signal. The reason that the fringe missing phenomenon happens only at the beginning of the signal is because of the ostensibly decreasing of the phase stimulus over time. Figure 4.17(a) displayed the dwelling of the lasing mode in stable solutions in the same manner as the previous simulation; from point A to B, C, D, then E for two cycles of the triangle modulation. The SMI output signal resulting from the dwelling of the lasing

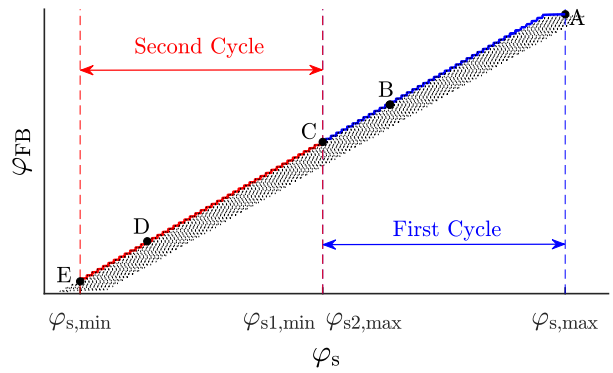

(a) Plot the dwelling path solutions of phase stimulus and phase response.

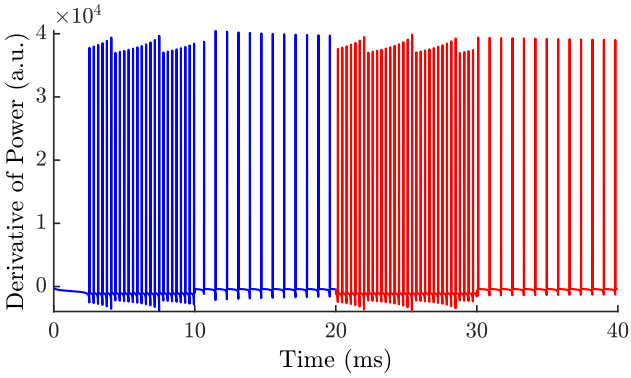

(b) Plot derivative of the output power in resulting from the dwelling solution path in (b).

Figure 4.17: (a) Plot the lasing mode behaviour resulting from the triangular phase stimulus sweeping under the feedback parameter $C = 26$. (b) Simulation the self-mixing power resulting from dwelling of the lasing mode in (a).

mode is presented in Figure 4.17(b).

4.2.3 | Experimental validation

As discussed in Chapter 3, the modulating laser emission frequency is easy to obtain by modulating the laser injection current. In this experiment, the FM coefficients are re-measured while varying the frequency modulations through the Eq. (3.6) in the SMI absolute distance application with the same experimental setup illustrated in Figure 4.14 as we change the electronics card and the laser diode in this experiment. The reason behind this changing is that we need a faster and high-frequency bandwidth to adapt the rotating target in our experiments. The laser diode (ML920J11S-01) with a package-

included a monitoring photodiode is associated to a collimating lens which focuses the laser beam on the target surface which is a white paper. The laser diode is operated with a bias injection current of 15 mA (about 2 times of its threshold current) and modulated with an amplitude of 5 mA peak-to-peak with a triangle waveform. The target is stationary at a distance of 1 m from the laser. The photodetected signal from the packaged photodiode is then converted to a voltage by a transimpedance amplifier with a selective bandwidth ranging from 150 kHz to 10 MHz.

In SMI absolute distance application, the derivative of the output signal will result in a series of sharp peaks in each half of the triangle waveform. The interferometric fringes are then detected by setting a threshold height. Later, the counted fringe number is then divided by the time spacing between the first and the last detected fringe to give the average spacing time. The FM coefficients are measured with different frequency modulation ranging from 1 kHz to 25 kHz; then results are plotted in Figure 4.18. It is interesting to highlight that the number of interferometric fringes decreases at higher frequency modulation, as a result of the decay of the FM coefficient.

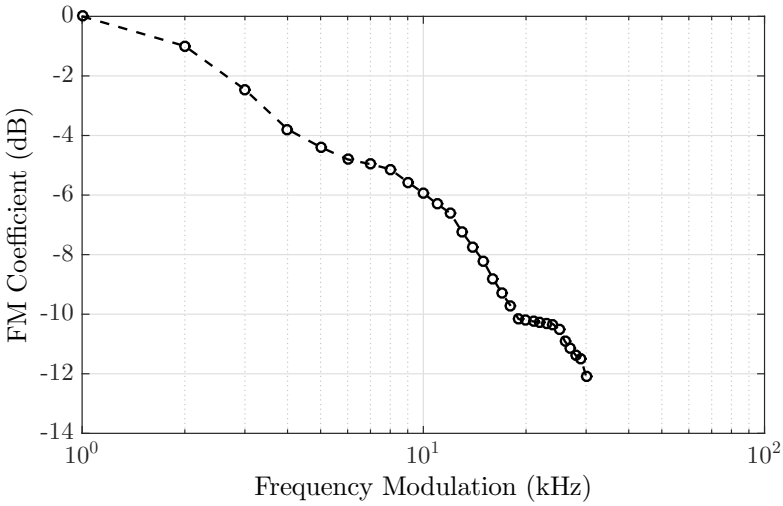

Figure 4.18: Plot the experimental results of FM coefficients in function of frequency modulations.

The experiment setup for the SMI absolute distance and target velocity by triangular frequency sweeping is depicted in Figure 4.19. The laser diode is injected with a bias current of 15 mA and modulated with an amplitude of 5 mA peak-to-peak at 5 kHz of frequency modulation. The laser beam focuses on the target surface through a collimating lens. The target is a disc that rotates thanks to the DC motor that is fixed at 1 m from the laser, so that it creates a $60°$ angle between the laser beam axis and the target

velocity vector. The disc surface is covered first by a white paper, then with a microprism reflective tape to obtain a higher reflection coefficient.

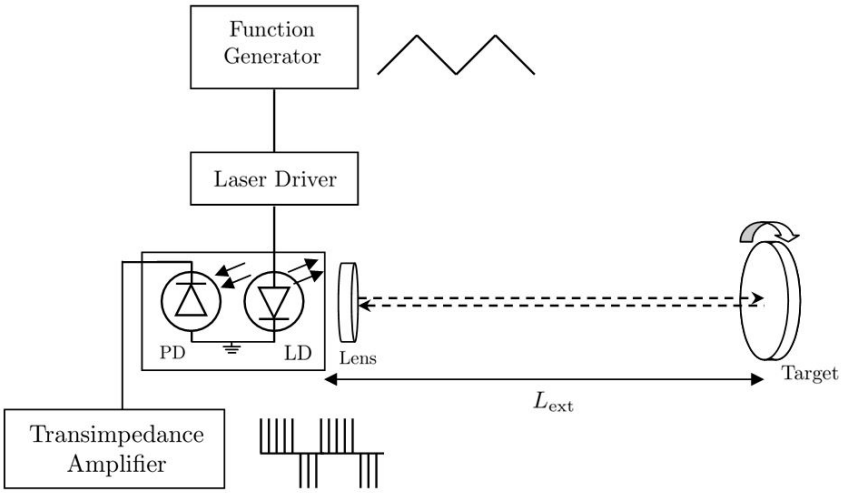

Figure 4.19: Block diagram of experimental setup. Laser and photodiode are in the same package, and the target is metal disc that can be rotated through the DC motor.

Figure 4.20 displays experimental results of the SMI signal when the distance beat frequency is superior to the Doppler beat frequency in different directions with a different surface. In the clockwise rotating direction, the number of interferometric fringes in the first half of the triangle modulation exceeds the number of fringe in the other half as shown in Figures 4.20(a) and (c). As expected, when the target rotates in the anti-clockwise direction, the opposite phenomenon is observed as shown in Figures 4.20(c) and (d). The SMI signals in Figures 4.20(a) and (b) are obtained with the white paper surface that generates no interferometric fringe disappearance. At the contrary, there are some missing interferometric fringes when the target is the reflective tape as displayed in Figures 4.20(c) and (d). It should be highlighted that those experimental results do not include the initial condition when the laser diode experiences the early current modulation. It is interesting to notice that the number of missing fringes between each half period modulation should be the same even the phase sweeping portions is not symmetrical.

The external cavity length and the target velocity in these experiments are calculated by using the average time between two consecutive fringes. The SMI output signal in Figure 4.20(a) results in an external cavity of 1.007 m and a Doppler frequency of 64.2 kHz, while Figures 4.20(b), (c) and (d) result in the distance of 0.9421 m, 1.16 m and 1.15 m;

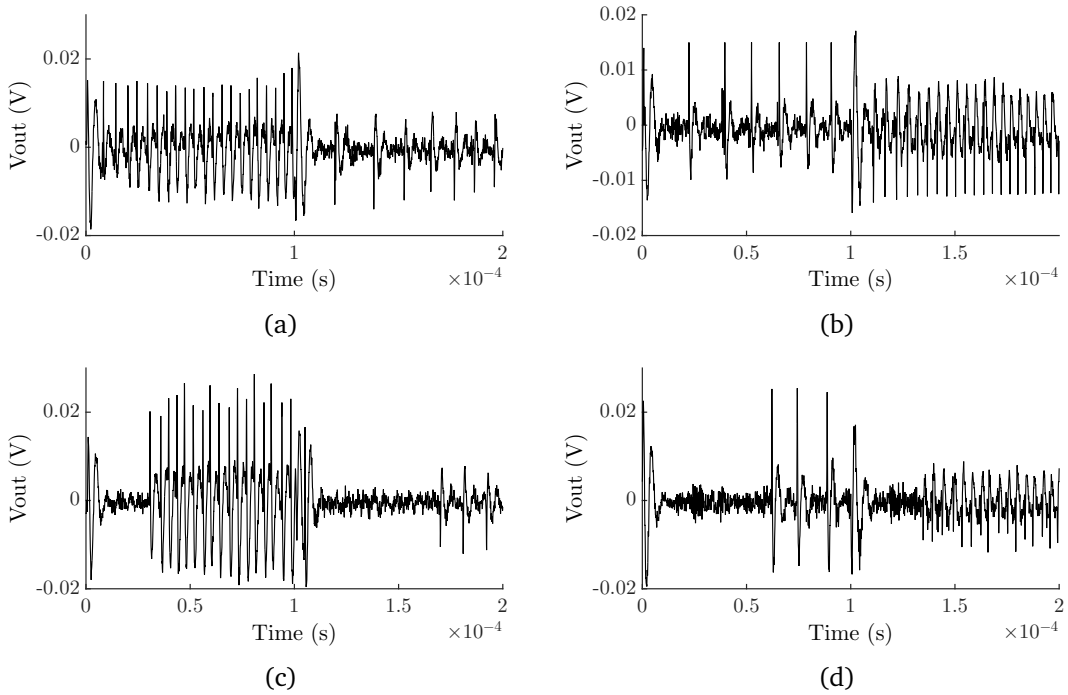

Figure 4.20: Experimental SMI signal acquisition when the distance beat frequency is superior to the Doppler frequency in different velocity directions and target surfaces. (a) and (b) The target as a white paper surface rotates in clockwise and anticlockwise, respectively. (c) and (d) The target as a microprism reflective tape surface rotates in clockwise and anticlockwise, respectively.

and Doppler frequencies of -75.9 kHz, 58.4 kHz and -60.4 kHz, respectively. With the white paper target surface, the measurement resolution of the distance is up to several centimetres as no interferometric fringe disappearance during the data acquisition but it raises up to more than 10 cm with the microprism reflective tape surface.

In the other case, when the distance beat frequency is inferior to the Doppler frequency, the interferometric fringes in the SMI signal appears either all positive or negative depending on the direction of rotation, the external cavity length is reduced to 30 cm; while the angle between the laser axis and the velocity vector is set to $30°$. All other parameters are kept constant as compared to the previous setup.

Measured SMI signals are plotted in Figures 4.21(a) and (b) for the white paper surface, and in Figures 4.21(c) and (d) for the reflective tape. By ignoring the initial condition of the first stage of laser current modulation, the fringe missing phenomenon does not occur at the beginning of the SMI signal even with high reflectivity from the microprism reflective tape surface. When the target rotates in the clockwise direction, all of the spikes observed in Figures 4.21(a) and (c) are positive. In contrary, when the

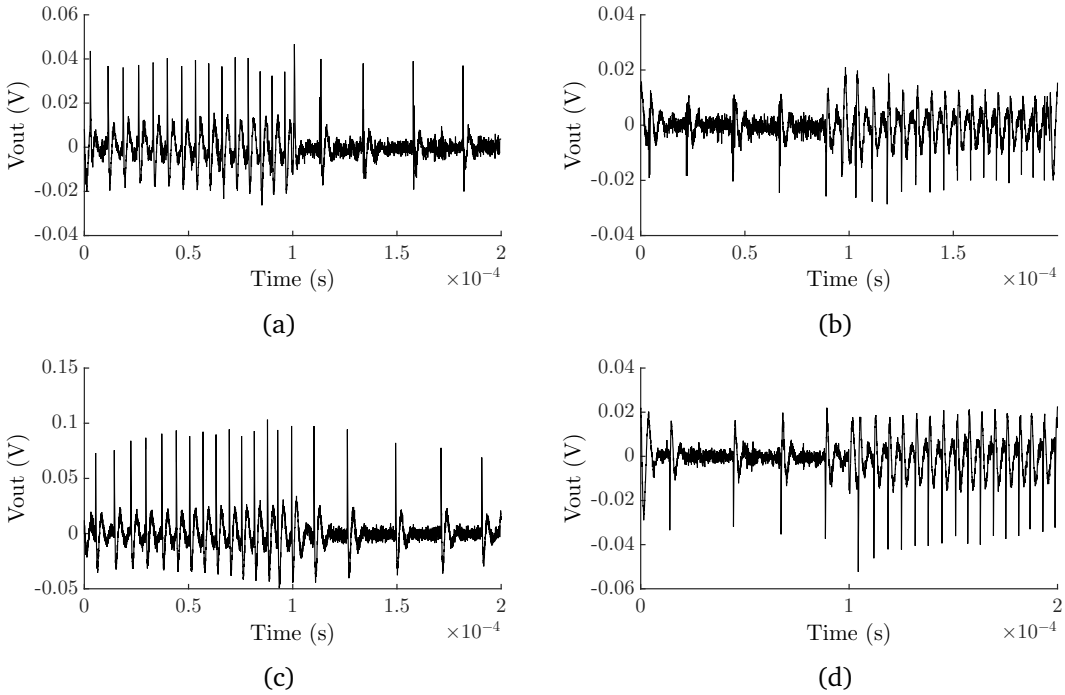

Figure 4.21: Experimental SMI signal acquisition when the distance beat frequency is inferior to the Doppler frequency in different velocity directions and target surfaces. (a) and (b) The target as a white paper surface rotates in clockwise and anticlockwise, respectively. (c) and (d) The target as a microprism reflective tape surface rotates in clockwise and anticlockwise, respectively.

target rotates in the anticlockwise direction, all of the spikes observed in Figures 4.21(b) and (d) are negative.

The experimental SMI signal results in almost the same number of interferometric fringes between the white paper and microprism reflective tape surface. The main difference between these signals is the fringe's amplitude. The result in Figure 4.21(a) gives a distance of 30.65 cm between the laser and the target through the average time spacing between fringes method, while Figures 4.21(b), (c) and (d) give 31.07 cm, 29.24 cm and 32.89 cm, respectively. The measurement resolution of distance is still limited to a few centimetres; again because of the non-linearity of the emission frequency through the linear modulation of the laser injection current. In addition, all the experimental results give almost the same Doppler beat frequency which is around 110 kHz.

4.3 | Profiling

4.3.1 | Distance measurement

With the methodology and theoretical background presented in this chapter, we propose to measure the profile of a translating (rotating) target. This technique is based on the triangle frequency sweeping as described in this chapter. For measurement accuracy reason, it needs high bandwidth electronics and a laser diode with a large frequency modulation coefficient. To demonstrate the feasibility of this technique, the experimental setup in Figure 4.19 is reused. First, different distances between the laser and the target ranging from 128 cm to 133 cm are measured when the target is fixed without any movement. While doing this, we can know the measurement resolution for the absolute distance before the target rotates. The target surface is the microprism reflective tape cover on the rotating disc. An attenuator is used along the path between the laser facet and the target to decrease the backscattered reflection coefficient thus avoiding fringe disappearance. The laser diode is operated with the injection current of 15 mA and modulated with an amplitude of 10 mA peak-to-peak at 5 kHz.

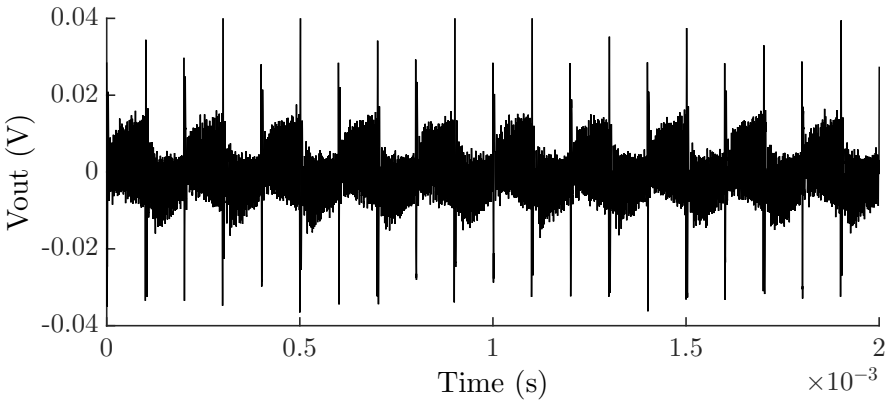

Figure 4.22: Experimental results of SMI distance signal by triangular frequency sweeping.

Each distance is measured ten times consecutively. Figure 4.22 shows the SMI signal with ten cycles of the triangle waveform at a distance of 128 cm in the time domain. Each modulation cycle, the SMI signal displays a series of interferometric fringes in each half of the triangle waveform as shown in Figure 4.23(a). The average time spacing between fringes by means of the average beat frequency is used to calculate the distance. The process of the external cavity distance determination is accomplished within three steps. First, the locations of the interferometric fringes in each half of the triangle waveform

are detected with the Matlab toolbox *findpeaks* as seen in Figure 4.23(b). Then, the beat frequencies on each half of the triangle waveform are determined. The analysis area for each half of the triangle waveform does not include the high ring peaks caused by the changing of modulation ramps which normally happens at the beginning of the modulation ramp. As described in Chapter 3, when the laser injection current is rawly modulated without any pre-distortion of the modulating waveform, the beat frequencies on each ramp are not constant. Moreover, noises are present in the signal; so any high peak of the noise that is higher than the threshold can be detected causing errors in the evaluation of the distance as shown in the first fringes of Figure 4.23(b). In some cases, the peak cannot be detected because its height is smaller than the threshold. These errors of peaks detection decrease the measurement resolution. To solve this problem, the range of useful beat frequencies is chosen based on their occurrence rate. Figure 4.23(c) displays an example of a histogram from detected frequencies in Figure 4.23(b). The beat frequencies ranging from 300 kHz and 500 kHz which are the most frequently detected are chosen to determine the average beat frequency.

Figure 4.24 displays the result of the distance measurement by using the average beat frequency detection. The resolution of each distance is still limited to the centimetre. It is interesting to note that an interferometric fringe corresponds to 1.63 cm. With the presence of noises caused by the electronic circuit and the non-linearity between the laser injection current and the laser emission frequency, the measurement resolution can be worse than 1.63 cm.

4.3.2 | Velocity measurement

The second experiment is to determine the Doppler frequency of the target alone without any current modulation. The same laser diode is operated with 15 mA of injection current, and the target as a metal disc rotates in the clockwise direction thanks to the DC motor feeder with a 10 V supply voltage. The target position is fixed at the angle of $45°$ between the laser beam axis and the target velocity vector. The target surface is covered by reflective tape, and an attenuator is fixed as in the previous experiment. It is interesting to notice that the SMI signal exhibits the same Doppler frequency at any given external cavity length. Figure 4.25(a) shows the SMI Doppler signal in the time domain where it displays a series of interferometric fringes with different amplitude due to speckle interferences. The Doppler frequency in this experiment can be found by applying the FFT to the SMI signal in the time domain, and it results in 275 kHz as displayed in Figure 4.25(b).

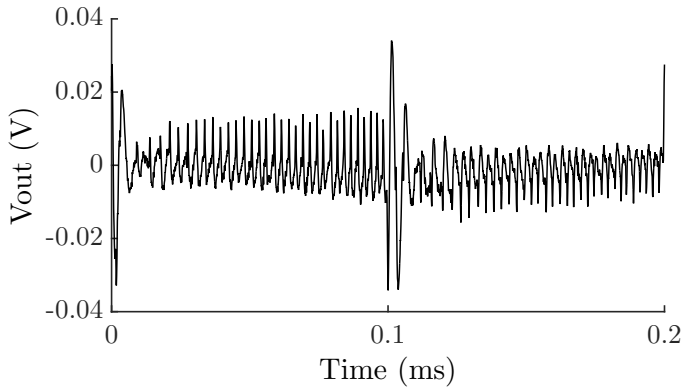

(a)

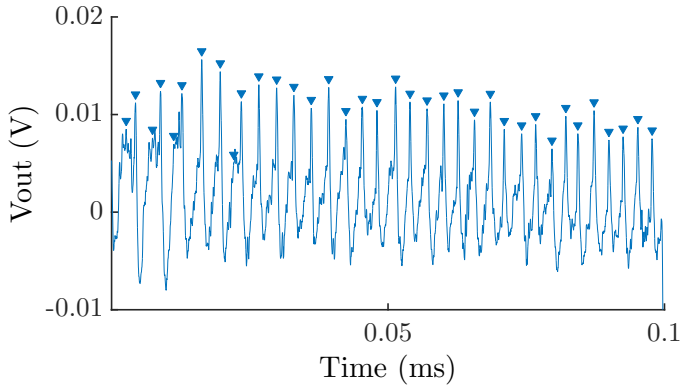

(b)

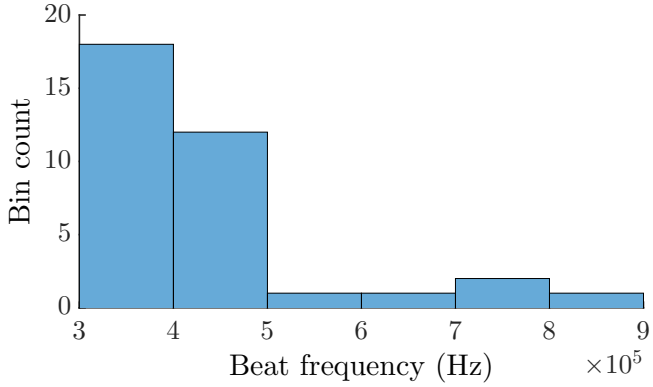

(c)

Figure 4.23: (a) Experimental results of SMI distance signal for one cycle of the triangle waveform. (b) Peaks detection of half-period of the triangular SMI waveform. (c) Histogram of beat frequencies resulting peak detections in (b).

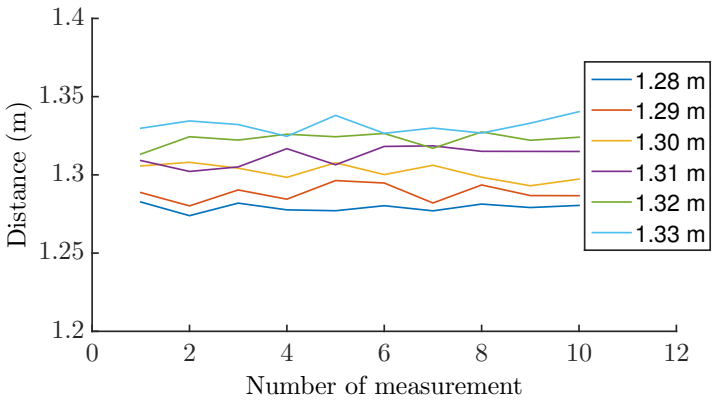

Figure 4.24: Distance measurements resulting from the SMI triangular frequency sweeping ranging from 128 cm to 133 cm.

4.3.3 | Distance and velocity measurement

The external cavity length and the target velocity can be determined at the same time by combining the two applications above. The same laser diode is operated with the same bias current of 15 mA and modulated with 10 mA peak-to-peak amplitude at 5 kHz triangle modulation. The target rotates by a DC motor supplied with 10 V, and the target surface is covered by a microprism reflective tape. The laser lights travel to target through the same attenuator used in previous sections.

Each external cavity distance and target velocity are measured ten times consecutively. Figure 4.26 displayed the SMI signal for ten cycles of the modulation triangle at the distance of 128 cm between the laser and the target when the target rotates producing a 275 kHz of Doppler frequency shift. At each modulation cycle, the number of observed interferometric fringes for each half of the triangle waveform is different as shown in Figure 4.27, this is because of the combined effect of modulated light's wavelength and the Doppler shift. The target distances and velocities in this experiment are determined by using the average beat frequency method. In this experiment, the data acquisition for each modulation cycle is 100 k sampling rates. The fringe detection method used in Section 4.3.1 is applied for each half of the modulation cycle. Figure 4.28(a) shows that a series of interferometric fringes in the signal of the SMI signal for the first half of the triangle waveform is detected from which results in the beat frequencies histogram shown in Figure 4.28(b). For another half of the triangle waveform, the number interferometric fringes are displayed less than the first half as shown in Figure 4.28(c), and the beat frequencies are plotted in the histogram in Figure 4.28(d). We see that a few of the peaks which are caused by noises are detected at the beginning of the signal;

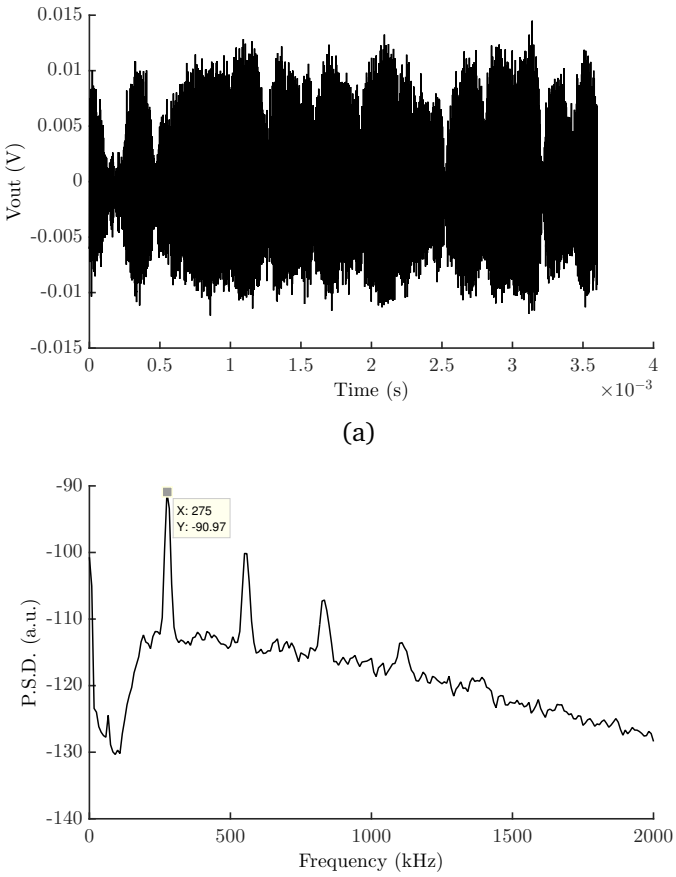

Figure 4.25: Experimental results of Doppler shift with the reflective tape surface. (a) The self-mixing signal in the time domain. (b) PSD of of the self-mixing power variations obtained from (a).

then those frequencies are rejected for the calculation process. The distances between the laser and the target are determined through the Eq. (4.17) with the actual distance ranging from 128 cm to 133 cm, while the Doppler beat frequencies of each distance are done with the Eq. (4.18). Figure 4.29 and Figure 4.30 depicts the SMI results for the target distance and velocity, respectively.

This accuracy of the proposed method in this section is still limited due to few reasons such as small frequency modulation coefficient of the laser diode, the limitation of bandwidth from the electronics card, and the non-linearity between the laser injection current and the laser emission frequency when we modulate the laser injection current in triangle waveform. However, based on the showing results, it is possible to determine the target's profile and also velocity when the target is in motion.

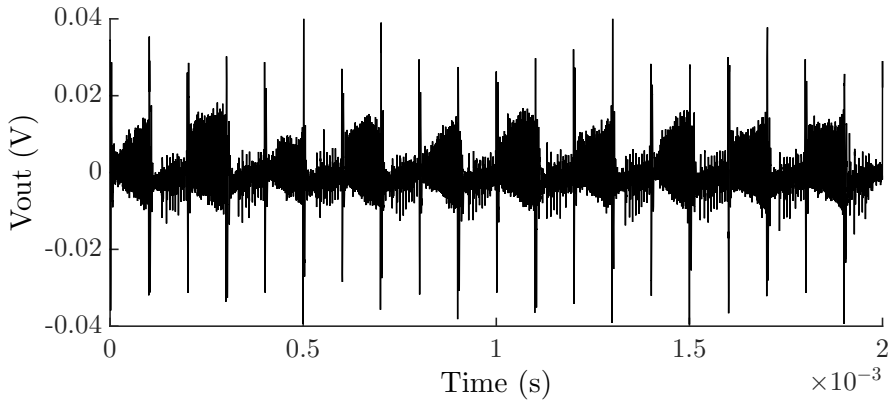

Figure 4.26: Experimental results of SMI signal of distance and velocity by triangular frequency sweeping.

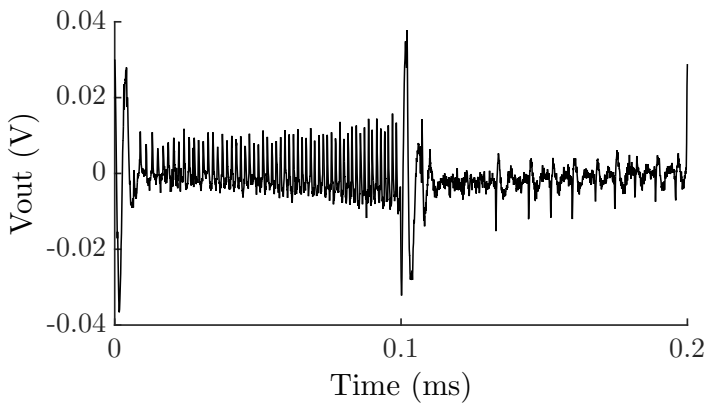

Figure 4.27: Experimental results of SMI signal of distance and velocity for one cycle of the triangle waveform.

4.4 | conclusion

The measurement of the external cavity length and the target velocity based on the SMI technique can be achieved by combining the absolute distance method that has been extensively described in previous chapters which produces a modulation of the laser power with a beat frequency related to the target distance, and the power modulation induced by the Doppler shift that affects the backscattered wave and which beat frequency is related to the target velocity. In order to combine the two applications into one, we propose a system where the laser emission frequency is modulated with triangle waveform and where the two different beat frequencies are determined by the signal processing thus allowing for the determination of the external distant target and the target's velocity at

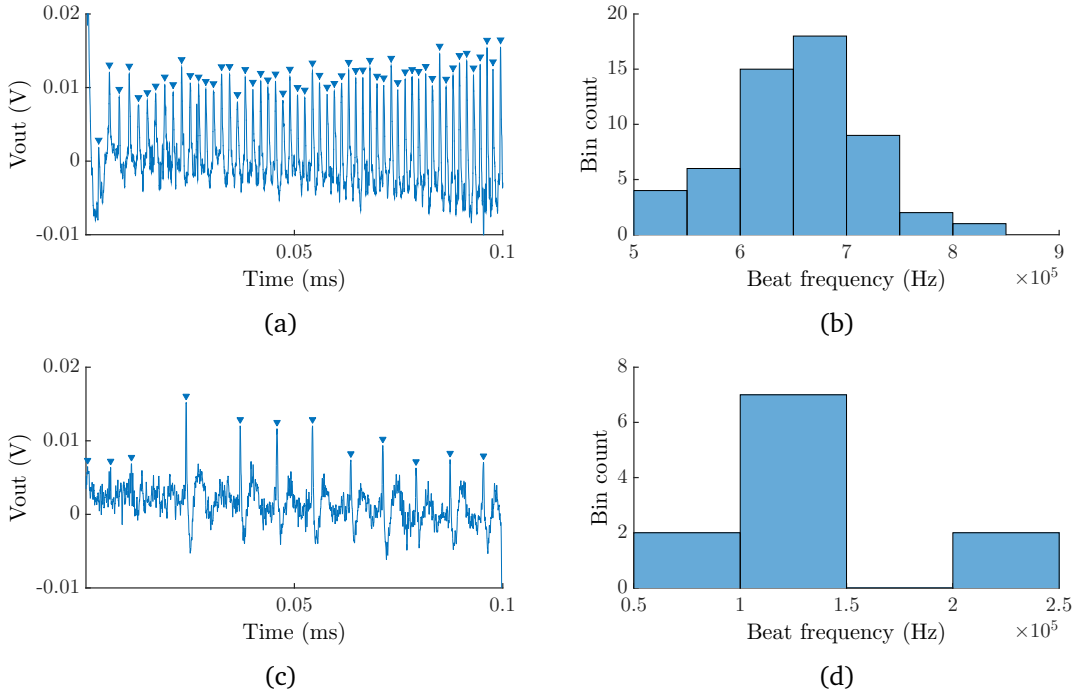

Figure 4.28: (a) Peak detections of the first half self-mixing signal of the triangle waveform. (b) Histogram of the beat frequencies resulting from (a). (c) Peak detections of the other half self-mixing signal of the triangle waveform. (d) Histogram of the beat frequencies resulting from (d).

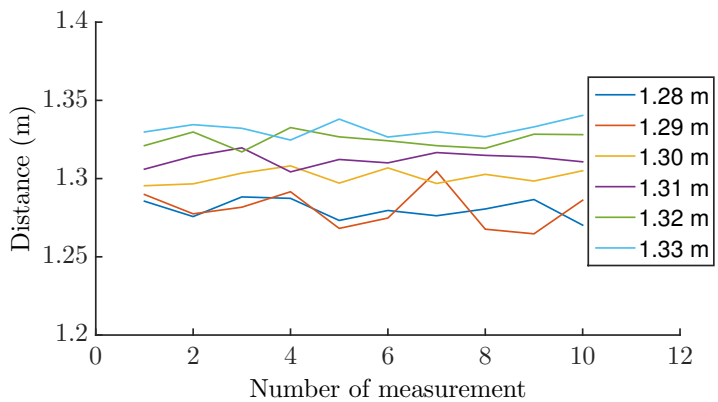

Figure 4.29: Distance measurements resulting from the SMI triangular frequency sweeping ranging from 128 cm to 133 cm when the target rotates.

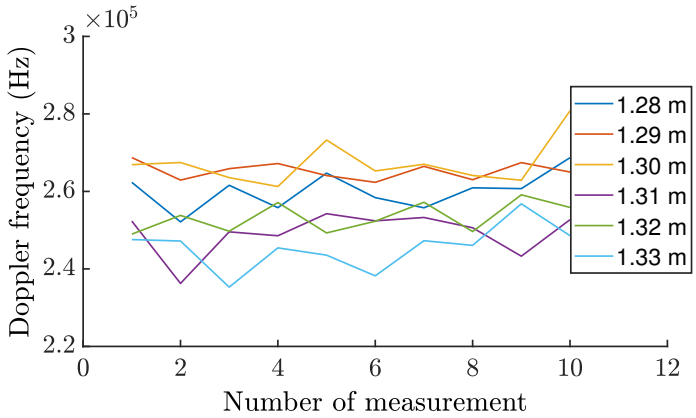

Figure 4.30: Doppler frequency measurement resulting from the SMI triangular frequency sweeping when the target is fixed at the distances ranging from 128 cm to 133 cm.

the same time. Two scenarios were evaluated considering the distance beat frequency can be either superior or inferior to the Doppler beat frequency. Moreover, the fringe disappearance phenomenon that was depicted in chapter 2 and 3 is predicted by the model and observed experimentally in the case where the distance beat frequency is superior to the Doppler frequency. This phenomenon is highly dependent on the feedback parameter C, and it can be explained by the analysis of the phase behaviour based on the excess phase equation.

Analysing the SMI output signal on each slope of the triangle modulation is interesting as it gives us an advantage of discriminating the direction of the target's velocity. We investigate this property both using time domain analysis and spectral domain when applying the FFT to each semi-period of triangle modulation in the optical output power.

As an application of the property to measure simultaneously the distance and the target velocity, we proposed to evaluate the feasibility of profiling a rough target surface. We have proposed the basic method for this application and designed an experimental methodology. However, the target profiling based on modulating the laser emission frequency needs future researches as the resolution that was obtained (in the centimetre range) may be insufficient in most of the applications. improvement of the laser frequency modulation through the injection current, in terms of dynamic, responsivity, and linearity would be clearly required in such an application.

Conclusions

The objectives of my Ph.D were two folds: first to re-investigate and develop the use of the laser diode under the optical feedback in different regimes and with a focus on the absolute distance application, and second to investigate the case where the distant target is moving and to evaluate the feasibility of a combined sensor for both velocity and distance by self-mixing interferometry. Thus, taking advantage of the main specificity of the SMI technique−it is a compact and self-aligned system, such a sensor based on a single laser diode could be of major interest for autonomous mobile systems in the domains of robotics, automotive, etc...

Chapter 1 gave a presentation to the usual methods for distance measurement based on sound, electromagnetic waves, and optical waves. Those methods of measurement have been used in different areas and purposes of application. For example, sonars based on the sound wave are used to detect objects underwater while radars based on the electromagnetic wave are used to determine long distant objects such as aircraft, ships, spacecraft, guided missiles, motor vehicles, weather formations, and terrain. However, sensors based on optic waves have various techniques such as stereo-vision, time of flight (LiDAR) and interferometry. Among the interferometry sensing family is self-mixing interferometry where the laser itself acts as a source and a sensor due to the high sensitivity to optical feedback of the laser diode. This detection technique leads to low-cost and robust as it does not need any reference arm or external detector, it is a self-aligned setup. The distant measurement resolution based on this technique has been improved over the years. However, those measurements were achieved with very low back-scattered light from the target and there are few research publications concerning the distance measurement with high back-scattered light power.

In chapter 2, we present an advanced study on the laser feedback interferometry theory. A classic model known as the three-mirror model as well as the rate equations de-

rived from the Lang and Kobayashi model are described in detail. The rate equations can be reduced to a single equation known as the excess phase equation. The most important parameter in the excess phase equation is the feedback parameter C. This parameter is very important as its value defines the optical feedback regimes of the laser which have a major impact on the behaviour of the laser diode. Re-investigating the behaviour of the laser diode in weak and moderate/strong optical feedback regimes allowed for a better understanding of the self-mixing technique. Those behaviours can be described with the excess phase equation or the rate equations. We have focused our study on a rarely described phenomenon that occurs when the laser is in a moderate/strong feedback regime: the disappearance of interferometric fringes. We have demonstrated that the number of missing interferometric fringes strongly depends on the feedback parameter C. The model proposed in this chapter shows that two interferometric fringes per semi-period of the modulation disappear if the coupling parameter C is increased by a value close to 2π. We also investigate the dependency of this phenomenon to other parameters such as the laser injection current, the type of the laser, and the working environment.

Chapter 3 and 4 presented the application models and experimental results obtained. All experimental set-ups were described in detail.

Chapter 3 focused on studies of the self-mixing absolute distance measurement. The measurement of absolute distance between the source and the target based on the SMI technique can be achieved when the laser emission frequency is typically modulated with triangle waveform. This modulation can be easily obtained by directly modulating the laser injection current. However, in practice, the laser emission frequency does not vary linearly with the injection current due to the plasma and thermal effect inside the laser inner cavity. That non-linear relationship tends to vary the beat frequencies in the SMI signal which then decreases the measurement resolution. The missing fringe phenomenon impacts the determination of the distance between the laser and the target with the classical method by counting the number of fringes and affecting the measurement resolution. Also, in this chapter, many experiments were conducted. Two parameters that fix the coupling coefficient C were calibrated for a combination of target surface (white paper, metal, reflective tapes with microspheres and microprims) and the target to sensor distances. As C also relies on laser intrinsic parameters, such a calibration does not give the C values, but it is possible from one configuration to the other to estimate precisely the change in C.

One of the other important parameters in the distance measurement is the frequency modulation coefficient that symbolises the relationship between the laser injection current and its emission frequency. This parameter normally depends on the laser type,

material, structure and the process of fabrication, and requires to be determined experimentally. With a DFB laser (L1550P5DFB) lasing at 1550 nm, our experiments showed that the value of laser FM coefficient decreases with the increase of frequency modulation. We have performed a characterization with the frequency ranging from 100 mHz to 1 kHz by counting interferometric fringes in the output power. Before going further in the validation of our model as regarding the interferometric fringe disappearance, we have evaluated the effect of the bias injection current on the number of interferometric fringes in the output power. We also investigate the linearity between the laser injection current and the laser emission frequency. Reshaping the laser injection current has been proposed by many researchers to improve the measurement resolution. However, even with the missing fringes in the output power, an alternative method without reshaping current was proposed in this thesis to improve the measurement resolution by using the curve fitting of the beat frequencies resulting from the SMI signal. To validate the proposed model of fringes disappearance in Chapter 2, two variable optical attenuators were used to control the back-scattered light intensity from the target. We observed that our model was in great agreement with our experimental results. However, we also observed that the number of fringes was different in each half of the triangle modulation in the cases where the laser first experiences a large and brutal change of feedback condition from the target. This was due to the initial condition where the laser bias injection current was first modulated. This behaviour can be explained in our model by the dwelling of the lasing mode in the laser phase behaviour. After the initial condition, the lasing phase condition will keep the lasing path even if the laser injection current pauses and is-re-modulated again with the same amplitude and frequency. On the other hand, if there is any perturbation in the phase stimulus at any time during the light propagation, the laser solution will change the path and restart from the initial condition.

When the target moves along the longitudinal axis of the laser beam or if it translates or rotates, the back-scattered light contains the Doppler shift. The combination of Doppler and distance measurement were discussed in Chapter 4 both in theory and experiment. Normally, the Doppler frequency in SMI is determined by a simple spectral analysis. In our experiment, the external cavity distance and the velocity of the target can be determined at the same time by triangular frequency sweeping technique. The number of interferometric fringe on each ramp of triangle modulation at the optical power varies with the Doppler frequency. This inequality of the fringe's number gives us a chance to calculate the external distant target and the target's velocity at the same time. Two possible cases were investigated: (1) when the distance beat frequency is superior to the Doppler frequency, and (2) when the distance beat frequency is inferior to the Doppler frequency. In both cases we used either the counting of the observed fringes or

the average time spacing method or a spectral analysis performed after an FFT algorithm was applied to determine the distance between the laser and the target.

Moreover, with the advantage of measuring the absolute distance and the target velocity at the same time, the target's profile and the target's speed can be identified. This measurement technique can be achieved with a very high-performance electronic device with low noise and high bandwidth, a linear frequency sweeping by reshaping or pre-distorting the laser injection current and a high-performance laser diode with a large variation between the laser injection current and the laser emission frequency to produce more interferometric fringes in the SMI signal to achieve a better resolution. This opens up additional opportunities for data analysis and the application of the sensor. For further research, this application can be used to replace LiDAR where SMI is a self-aligned setup sensor, compact and more robust.

Bibliography

[1] Takashi Fujii and Tetsuo Fukuchi. *Laser remote sensing*. CRC press, 2005.

[2] Maric Josip and Siedersbeck Alfons. *Time-of-flight (ToF) measurement using pulse lasers*. OSRAM Opto Semiconductors, 11 2018.

[3] Christophe Gorecki. Range finding using frequency-modulated interferometry with a monomode external-cavity laser diode. *Japanese journal of applied physics*, 35(5R):2833, 1996.

[4] F. Gouaux, N. Servagent, and T. Bosch. Absolute distance measurement with an optical feedback interferometer. *Appl. Opt.*, 37(28):6684–6689, Oct 1998.

[5] Ming Wang, Takahiko Sato, Guanming Lai, and Shigenobu Shinohara. Self-mixing interferometry for distance and displacement measurement by fourier transform method. In *Laser Diodes and LEDs in Industrial, Measurement, Imaging, and Sensors Applications II; Testing, Packaging, and Reliability of Semiconductor Lasers V*, volume 3945, pages 193–200. International Society for Optics and Photonics, 2000.

[6] Yah Leng Lim, Karl Bertling, Pierre Rio, JR Tucker, and AD Rakic. Displacement and distance measurement using the change in junction voltage across a laser diode due to the self-mixing effect. In *Photonics: Design, Technology, and Packaging II*, volume 6038, page 60381O. International Society for Optics and Photonics, 2006.

[7] Dongmei Guo and Ming Wang. New absolute distance measurement technique with a self-mixing interferometer. In *Journal of Physics: Conference Series*, volume 48, page 1381. IOP Publishing, 2007.

[8] John R Tucker, Aleksandar D Rakić, Christopher J O'Brien, and Andrei V Zvyagin. Effect of multiple transverse modes in self-mixing sensors based on vertical-cavity surface-emitting lasers. *Applied optics*, 46(4):611–619, 2007.

[9] M. Norgia, A. Magnani, and A. Pesatori. High resolution self-mixing laser rangefinder. *Review of Scientific Instruments*, 83(4):045113, 2012.

[10] K. Kou, X. Li, L. Li, and H. Xiang. Injected current reshaping in distance measurement by laser self-mixing interferometry. *Appl. Opt.*, 53(27):6280–6286, Sep 2014.

[11] T. Taimre, M. Nikolić, K. Bertling, Y. L. Lim, T. Bosch, and A. D. Rakić. Laser feedback interferometry: a tutorial on the self-mixing effect for coherent sensing. *Adv. Opt. Photon.*, 7(3):570–631, Sep 2015.

[12] Larry A Coldren, Scott W Corzine, and Milan L Mašanovitć. *Diode lasers and photonic integrated circuits*, volume 218. John Wiley & Sons, 2012.

[13] Roy Edgar Hansen. Introduction to sonar. *Course Material to INF-GEO4310, University of Oslo,(Oct. 7, 2009)*, 2009.

[14] Jaime C Fonseca, Júlio S Martins, and Carlos Couto. An experimental model for sonar sensors. 2001.

[15] N. Friedman. *The Naval Institute Guide to World Naval Weapons Systems, 1997-1998*. Naval Institute Guide to World Naval Weapons Systems Series. Naval Institute Press, 1997.

[16] B. Siciliano and O. Khatib. *Springer Handbook of Robotics*. Springer Handbook of Robotics. Springer Berlin Heidelberg, 2008.

[17] A. Stelzer, M. Jahn, and S. Scheiblhofer. Precise distance measurement with cooperative fmcw radar units. In *2008 IEEE Radio and Wireless Symposium*, pages 771–774, Jan 2008.

[18] Garry Berkovic and Ehud Shafir. Optical methods for distance and displacement measurements. *Adv. Opt. Photon.*, 4(4):441–471, Dec 2012.

[19] A. L. Hou, X. Cui, Y. Geng, W. J. Yuan, and J. Hou. Measurement of safe driving distance based on stereo vision. In *2011 Sixth International Conference on Image and Graphics*, pages 902–907, Aug 2011.

[20] Marc Lescure Risto A. Myllylae Marc Rioux Markus-Christian Amann, Thierry M. Bosch. Laser ranging: a critical review of unusual techniques for distance measurement. *Optical Engineering*, 40:40 – 40 – 10, 2001.

[21] Claus Weitkamp. *Lidar: range-resolved optical remote sensing of the atmosphere*, volume 102. Springer Science & Business, 2006.

[22] Pasi Palojarvi. Integrated electronic and optoelectronic circuits and devices for pulsed time-of-flight laser rangefinding. 2004.

[23] Bastien Béchadergue, Luc Chassagne, and Hongyu Guan. Visible light phase-shift rangefinder for platooning applications. In *2016 IEEE 19th International Conference on Intelligent Transportation Systems (ITSC)*, pages 2462–2468. IEEE, 2016.

[24] Albert A Michelson. Xxx. on the application of interference methods to spectroscopic measurements.—ii. *The London, Edinburgh, and Dublin Philosophical Magazine and Journal of Science*, 34(208):280–299, 1892.

[25] Parameswaran Hariharan. *Basics of interferometry*. Elsevier, 2010.

[26] Khaled Alzahrani, David Burton, Francis Lilley, Munther Gdeisat, Frederic Bezombes, and Mohammad Qudeisat. Absolute distance measurement with micrometer accuracy using a michelson interferometer and the iterative synthetic wavelength principle. *Optics express*, 20(5):5658–5682, 2012.

[27] René Benoît. Application des phénomènes d'interférence à des déterminations métrologiques. *J. Phys. Theor. Appl.*, 7(1):57–68, 1898.

[28] K Meiners-Hagen, René Schödel, F Pollinger, and Ahmed Abou-Zeid. Multi-wavelength interferometry for length measurements using diode lasers. 9, 04 2009.

[29] A Olsson and CL Tang. Dynamic interferometry techniques for optical path length measurements. *Applied optics*, 20(20):3503–3507, 1981.

[30] RJ Tansey. An absolute distance interferometer using a dye laser heterodyne interferometer and spatial separation of beams. In *Precision Surface Metrology*, volume 429, page 43, 1983.

[31] Eugene Hecht. Optics. 2002. *Pearson Education, Inc.,*, 360:366–367, 2002.

[32] GP Barwood, P Gill, and WRC Rowley. High-accuracy length metrology using multiple-stage swept-frequency interferometry with laser diodes. *Measurement Science and Technology*, 9(7):1036, 1998.

[33] Karl-Heinz Bechstein and Werner Fuchs. Absolute interferometric distance measurements applying a variable synthetic wavelength mesures de distances absolues par interférométrie utilisant une longueur d'onde variable synthétique. *Journal of Optics*, 29(3):179, 1998.

[34] Th Kinder and Klaus-Dieter Salewski. Absolute distance interferometer with grating-stabilized tunable diode laser at 633 nm. *Journal of Optics A: Pure and Applied Optics*, 4(6):S364, 2002.

[35] T. Bosch, C. Bès, L. Scalise, and G. Plantier. Optical feedback interferometry. In C. A. Grimes, E.C. Dickey, and M.V. Pishko, editors, *Encyclopedia of Sensors*, volume vol. X, pages 1–20. American Scientific Publishers, 2006.

[36] Silvano Donati. Developing self-mixing interferometry for instrumentation and measurements. *Laser & Photonics Reviews*, 6(3):393–417, 2012.

[37] N. Servagent, F. Gouaux, and T. Bosch. Measurements of displacement using the self-mixing interference in a laser diode. *Journal of Optics*, 29(3):168, 1998.

[38] Y. Gao, Y. Yu, J. Xi, and Q. Guo. Simultaneous measurement of vibration and parameters of a semiconductor laser using self-mixing interferometry. *Appl. Opt.*, 53(19):4256–4263, Jul 2014.

[39] M. J. Rudd. A laser doppler velocimeter employing the laser as a mixer-oscillator. *Journal of Physics E: Scientific Instruments*, 1(7):723, 1968.

[40] G. Plantier, N. Servagent, T. Bosch, and A. Sourice. Real-time tracking of time-varying velocity using a self-mixing laser diode. *IEEE Transactions on Instrumentation and Measurement*, 53(1):109–115, Feb 2004.

[41] L. Campagnolo, M. Nikolić, J. Perchoux, Y. L. Lim, K. Bertling, K. Loubière, Laurent Prat, A. D. Rakić, and T. Bosch. Flow profile measurement in microchannel using the optical feedback interferometry sensing technique. *Microfluidics and Nanofluidics*, 14(1):113–119, Jan 2013.

[42] J. Perchoux, A. Quotb, R. Atashkhooei, F. J. Azcona, E. E. Ramírez-Miquet, O. Bernal, A. Jha, A. Luna-Arriaga, C. Yanez, J. Caum, T. Bosch, and S. Royo. Current developments on optical feedback interferometry as an all-optical sensor for biomedical applications. *Sensors*, 16(5), 2016.

[43] M. Norgia, A. Magnani, D. Melchionni, and A. Pesatori. Drop measurement system for biomedical application. *IEEE Transactions on Instrumentation and Measurement*, 64(9):2513–2517, Sept 2015.

[44] K. Bertling, J. Perchoux, T. Taimre, R. Malkin, D. Robert, A. D. Rakić, and T. Bosch. Imaging of acoustic fields using optical feedback interferometry. *Opt. Express*, 22(24):30346–30356, Dec 2014.

[45] R. Kliese, Y. L. Lim, K. Bertling, A. A. A. Bakar, T. Bosch, and A. D. Rakić. Self-mixing displacement sensing using the junction voltage variation in a gan laser. In *2008 Conference on Optoelectronic and Microelectronic Materials and Devices*, pages 23–25, July 2008.

[46] PGR King and GJ Steward. Metrology with an optical maser. *New Sci*, 17(180):14, 1963.

[47] H Bachert and S Raab. The influence of external optical coupling on the threshold current density of gaas injection lasers. *physica status solidi (b)*, 29(2):K175–K178, 1968.

[48] VN Morozov, VV Nikitin, and AA Sheronov. Self-synchronization of modes in a gaas semiconductor injection laser. *JETP Lett*, 7(9):256–258, 1968.

[49] R. Lang and K. Kobayashi. External optical feedback effects on semiconductor injection laser properties. *IEEE Journal of Quantum Electronics*, 16(3):347–355, Mar 1980.

[50] A Dandridge, RO Miles, and TG Giallorenzi. Diode laser sensor. *Electronics Letters*, 16(25):948–949, 1980.

[51] James H Churnside. Laser doppler velocimetry by modulating a co 2 laser with backscattered light. *Applied optics*, 23(1):61–66, 1984.

[52] S Shinohara, A Mochizuki, H Yoshida, and Masao Sumi. Laser doppler velocimeter using the self-mixing effect of a semiconductor laser diode. *Applied Optics*, 25(9):1417–1419, 1986.

[53] Glenn Beheim and Klaus Fritsch. Range finding using frequency-modulated laser diode. *Appl. Opt.*, 25(9):1439–1442, May 1986.

[54] Shigenobu Shinohara, Yoshiji Yoshida, Hirofumi Yoshida, Hiroaki Ikeda, Masafumi Miyata, Ken-ichi Nishide, and Masao Sumi. High-precision range finder for slowly

moving target with rough surface. In *[Proceedings] IECON'90: 16th Annual Conference of IEEE Industrial Electronics Society*, pages 659–664. IEEE, 1990.

[55] Thierry Bosch, Noel Servagent, Ryad Chellali, and Marc Lescure. Three-dimensional object construction using a self-mixing type scanning laser range finder. *IEEE Transactions on Instrumentation and Measurement*, 47(5):1326–1329, 1998.

[56] Klaus Petermann. *Laser diode modulation and noise*, volume 3. Springer Science & Business Media, 2012.

[57] Junji Ohtsubo. *Semiconductor lasers: stability, instability and chaos*, volume 111. Springer, 2012.

[58] Russell Kliese, Thomas Taimre, A Ashrif A Bakar, Yah Leng Lim, Karl Bertling, Milan Nikolić, Julien Perchoux, Thierry Bosch, and Aleksandar D Rakić. Solving self-mixing equations for arbitrary feedback levels: a concise algorithm. *Applied optics*, 53(17):3723–3736, 2014.

[59] G. Acket, D. Lenstra, A. Den Boef, and B. Verbeek. The influence of feedback intensity on longitudinal mode properties and optical noise in index-guided semiconductor lasers. *IEEE Journal of Quantum Electronics*, 20(10):1163–1169, October 1984.

[60] R. Tkach and A. Chraplyvy. Regimes of feedback effects in 1.5 distributed feedback lasers. *Journal of Lightwave Technology*, 4(11):1655–1661, Nov 1986.

[61] S. Donati and R. H. Horng. The diagram of feedback regimes revisited. *IEEE Journal of Selected Topics in Quantum Electronics*, 19(4):1500309–1500309, July 2013.

[62] O. D. Bernal, H. C. Seat, U. Zabit, F. Surre, and T. Bosch. Robust detection of non-regular interferometric fringes from a self-mixing displacement sensor using bi-wavelet transform. *IEEE Sensors Journal*, 16(22):7903–7910, Nov 2016.

[63] M. Norgia and S. Donati. A displacement-measuring instrument utilizing self-mixing interferometry. *IEEE Transactions on Instrumentation and Measurement*, 52(6):1765–1770, Dec 2003.

[64] G. Giuliani, M. Norgia, S. Donati, and T. Bosch. Laser diode self-mixing technique for sensing applications. *Journal of Optics A: Pure and Applied Optics*, 4(6):S283, 2002.

[65] Y. Yu, G. Giuliani, and S. Donati. Measurement of the linewidth enhancement factor of semiconductor lasers based on the optical feedback self-mixing effect. *IEEE Photonics Technology Letters*, 16(4):990–992, April 2004.

[66] Y. Gao, Y. Yu, J. Xi, Q. Guo, J. Tong, and S. Tong. Improved method for estimation of multiple parameters in self-mixing interferometry. *Appl. Opt.*, 54(10):2703–2709, Apr 2015.

[67] O. D. Bernal, U. Zabit, and T. Bosch. Classification of laser self-mixing interferometric signal under moderate feedback. *Appl. Opt.*, 53(4):702–708, Feb 2014.

[68] Y. Yu, J. Xi, J. F. Chicharo, and T. M. Bosch. Optical feedback self-mixing interferometry with a large feedback factor c : Behavior studies. *IEEE Journal of Quantum Electronics*, 45(7):840–848, July 2009.

[69] U. Zabit, F. Bony, T. Bosch, and A. D. Rakić. A self-mixing displacement sensor with fringe-loss compensation for harmonic vibrations. *IEEE Photonics Technology Letters*, 22(6):410–412, March 2010.

[70] J. El Assad. *Analysis of self-mixing moderate and strong feedback regimes for mechatronics applications*. PhD thesis, INPT, 2008.

[71] MH Koelink, FFM De Mul, AL Weijers, Jan Greve, R Graaff, ACM Dassel, and JG Aarnoudse. Fiber-coupled self-mixing diode-laser doppler velocimeter: technical aspects and flow velocity profile disturbances in water and blood flows. *Applied optics*, 33(24):5628–5641, 1994.

[72] R Tkach and AR Chraplyvy. Regimes of feedback effects in 1.5-μm distributed feedback lasers. *Journal of Lightwave technology*, 4(11):1655–1661, 1986.

[73] R Juškaitis, NP Rea, and Tony Wilson. Semiconductor laser confocal microscopy. *Applied optics*, 33(4):578–584, 1994.

[74] Deborah M Kane and K Alan Shore. *Unlocking dynamical diversity: optical feedback effects on semiconductor lasers*. John Wiley & Sons, 2005.

[75] G. Plantier, C. Bes, and T. Bosch. Behavioral model of a self-mixing laser diode sensor. *IEEE Journal of Quantum Electronics*, 41(9):1157–1167, Sept 2005.

[76] Karl Bertling, John R Tucker, and Aleksandar D Rakic. Optimum injection current waveform for a laser rangefinder based on the self-mixing effect. In *Photonics: Design, Technology, and Packaging*, volume 5277, pages 334–346. International Society for Optics and Photonics, 2004.

[77] E. Gagnon and J. F. Rivest. Laser range imaging using the self-mixing effect in a laser diode. *IEEE Transactions on Instrumentation and Measurement*, 48(3):693–699, Jun 1999.

[78] Wikipedia. Runge–kutta methods Wikipedia, the free encyclopedia, 2019. [Online; accessed 14-March-2019].

[79] G Bönsch and E Potulski. Measurement of the refractive index of air and comparison with modified edlén's formulae. *Metrologia*, 35(2):133, 1998.

[80] Tao Wei, Yukun Han, Yanjun Li, Hai-Lung Tsai, and Hai Xiao. Temperature-insensitive miniaturized fiber inline fabry-perot interferometer for highly sensitive refractive index measurement. *Optics Express*, 16(8):5764–5769, 2008.

[81] Yu.N. Dubnistchev and Yu.G. Vasilenko. A laser doppler velocimeter which measures the three components of velocity. *Optics & Laser Technology*, 8(3):129 – 131, 1976.

[82] B.M. Watrasiewicz and M.J. Rudd. *Laser Doppler measurements*. Butterworths, 1976.

[83] Tariq S Durrani and Clive A Greated. Laser systems in flow measurement. *New York, Plenum Press, 1977. 303 p.*, 1977.

[84] Christian Zakian, Mark Dickinson, and Terence King. Particle sizing and flow measurement using self-mixing interferometry with a laser diode. *Journal of Optics A: Pure and Applied Optics*, 7(6):S445, 2005.

[85] M Nikolić, T Taimre, JR Tucker, Yah Leng Lim, K Bertling, and AD Rakić. Laser dynamics under frequency-shifted optical feedback with random phase. *Electronics Letters*, 50(19):1380–1382, 2014.

[86] H-E Albrecht, Nils Damaschke, Michael Borys, and Cameron Tropea. *Laser Doppler and phase Doppler measurement techniques*. Springer Science & Business Media, 2013.

[87] Kazuo Kyuma, Shuichi Tai, Koichi Hamanaka, and Masahiro Nunoshita. Laser doppler velocimeter with a novel optical fiber probe. *Applied optics*, 20(14):2424–2427, 1981.

[88] Usman Zabit, Olivier D Bernal, and Thierry Bosch. Self-mixing laser sensor for large displacements: Signal recovery in the presence of speckle. *IEEE Sensors Journal*, 13(2):824–831, 2013.

[89] Reza Atashkhooei, Santiago Royo, Francisco Azcona, and Usman Zabit. Analysis and control of speckle effects in self-mixing interferometry. In *SENSORS, 2011 IEEE*, pages 1390–1393. IEEE, 2011.

[90] U Zabit, R Atashkhooei, T Bosch, S Royo, F Bony, and AD Rakic. Adaptive self-mixing vibrometer based on a liquid lens. *Optics letters*, 35(8):1278–1280, 2010.

Résumé / Abstract

Title: Self-mixing interferometry for absolute distance measurement: modelling and experimental demonstration of intrinsic limitation

Abstract: The fringe disappearance phenomenon in the self-mixing interferometry occurs whenever the external round-trip phase at free-running state is modulated by either external modulation such as external cavity length changes or internal modulation when the laser injection current is modulated with a high back-scattered light power. This phenomenon has been observed by many authors in the context of harmonic motion or vibration application. The core issue in this configuration is the unfeasibility to maintain a constant feedback level over the target course due mostly to speckle or an imperfect alignment. To the best of our knowledge, no accurate explanations or theories on the mechanism on the fringe disappearance phenomenon have been published so far. In this thesis, a novel approach that depicts the mechanism of interferometric fringes disappearance is proposed that highlights with a new perspective the impact of the coupling strength between the laser diode and the external cavity on the number of missing fringes. An absolute distance measurement has been set where the laser diode is operated with modulation of the injection current in the triangle waveform. As compared to the vibration sensing scheme, the absolute distance approach guarantees a stable feedback level thus allowing for more repeatable experiment conditions. The observed experimental results show an agreement with the proposed model on this phenomenon which is based on the excess phase equation. There is also a remarkable demonstration both experimentally and theoretically that the number of missing fringes in the SMI signal can be different between the first modulation ramp as compared to others.

Keywords: Self-mixing interferometry, laser feedback interferometry, optical feedback, fringe disappearance, absolute distance measurement, mathematical model, optical sensor.

Titre: Interférométrie à rétro-injection optique pour la mesure de distance absolue : modélisation et démonstration expérimentale des limites intrinsèques

Résumé: Le phénomène de disparition des franges dans l'interférométrie à rétro-injection optique se produit chaque fois que la phase externe de laser à l'état de fonctionnement libre est modulée par une modulation externe telle que des changements de longueur de cavité externe ou une modulation interne, c'est-à-dire le courant d'injection laser est modulé, avec un retour élevé de la puissance lumineuse de la cible. Ce phénomène a été observé par de nombreux auteurs dans le cadre de l'application de mouvements harmoniques ou de vibrations. Le problème dans cette configuration est l'impossibilité de maintenir un niveau de rétro-injection optique constant sur la cible en raison principalement de l'effet Speckle ou d'un alignement imparfait. A notre connaissance, aucune explication ou théorie précise sur le mécanisme du phénomène de disparition de franges n'a été publiée à ce jour. Dans cette thèse, une nouvelle approche qui décrit le mécanisme de disparition des franges interférométriques est proposée qui met en évidence avec une nouvelle perspective l'impact de la force de couplage entre la diode laser et la cavité externe sur le nombre de franges disparus. Une mesure de distance absolue a été définie où le courant d'injection de diode laser est modulé dans la forme de triangulaire. Par rapport au schéma de détection des vibrations, l'approche de distance absolue garantit un niveau de rétro-injection optique stable permettant ainsi des conditions d'expérience plus reproductibles. Les résultats expérimentaux observés montrent une concordance avec le modèle proposé sur ce phénomène qui est basé sur l'équation de phase. Il y a aussi une démonstration remarquable à la fois expérimentalement et théoriquement que le nombre de franges disparus dans le signal SMI peut être différent entre la première rampe de modulation par rapport aux autres.

Mots-clés: Interférométrie à rétro-injection optique, disparition de franges, mesure de distance absolue, modèle mathématique, capteur optique